Lawrence Berkeley National Laboratory
LBL Publications

Title
The DESI Early Data Release white dwarf catalogue

Permalink
https://escholarship.org/uc/item/6zh078qk

Journal
Monthly Notices of the Royal Astronomical Society, 535(1)

ISSN
0035-8711

Authors
Manser, Christopher J
Izquierdo, Paula
Gänsicke, Boris T
et al.

Publication Date
2024-10-25

DOI
10.1093/mnras/stae2205

Copyright Information
This work is made available under the terms of a Creative Commons Attribution License, available at https://creativecommons.org/licenses/by/4.0/

Peer reviewed

eScholarship.org Powered by the California Digital Library
University of California

Monthly Notices of the ROYAL ASTRONOMICAL SOCIETY

MNRAS **535,** 254–289 (2024)
Advance Access publication 2024 September 24

https://doi.org/10.1093/mnras/stae2205

The DESI Early Data Release white dwarf catalogue

Christopher J. Manser,[1,2] Paula Izquierdo,[2★] Boris T. Gänsicke,[2] Andrew Swan,[2] Detlev Koester,[3] Akshay Robert,[4] Siyi Xu,[5] Keith Inight,[2] Ben Amroota,[1] N. P. Gentile Fusillo,[6] Sergey E. Koposov,[7,8,9] Bokyoung Kim,[7] Arjun Dey,[10] Carlos Allende Prieto,[11,12] J. Aguilar,[13] S. Ahlen,[14] R. Blum,[10] D. Brooks,[4] T. Claybaugh,[13] A. P. Cooper,[15] K. Dawson,[16] A. de la Macorra,[17] P. Doel,[4] J. E. Forero-Romero,[18,19] E. Gaztañaga,[20,21,22] S. Gontcho A Gontcho,[13] K. Honscheid,[23,24,25] T. Kisner,[13] A. Kremin,[13] A. Lambert,[13] M. Landriau,[13] L. Le Guillou,[26] Michael E. Levi,[13] T. S. Li,[27] A. Meisner,[10] R. Miquel,[28,29] J. Moustakas,[30] J. Nie,[31] N. Palanque-Delabrouille,[13,32] W. J. Percival,[33,34,35] C. Poppett,[13,36,37] F. Prada,[38] M. Rezaie,[39] G. Rossi,[40] E. Sanchez,[41] E. F. Schlafly,[42] D. Schlegel,[13] M. Schubnell,[43] H. Seo,[43] J. Silber,[13] G. Tarlé,[43] B. A. Weaver,[10] Z. Zhou[31] and H. Zou[31]

Affiliations are listed at the end of the paper

Accepted 2024 September 18. Received 2024 September 5; in original form 2024 February 28

ABSTRACT

The Early Data Release (EDR) of the Dark Energy Spectroscopic Instrument (DESI) comprises spectroscopy obtained from 2020 December 14 to 2021 June 10. White dwarfs were targeted by DESI both as calibration sources and as science targets and were selected based on *Gaia* photometry and astrometry. Here, we present the DESI EDR white dwarf catalogue, which includes 2706 spectroscopically confirmed white dwarfs of which approximately 60 per cent have been spectroscopically observed for the first time, as well as 66 white dwarf binary systems. We provide spectral classifications for all white dwarfs, and discuss their distribution within the *Gaia* Hertzsprung–Russell diagram. We provide atmospheric parameters derived from spectroscopic and photometric fits for white dwarfs with pure hydrogen or helium photospheres, a mixture of those two, and white dwarfs displaying carbon features in their spectra. We also discuss the less abundant systems in the sample, such as those with magnetic fields, and cataclysmic variables. The DESI EDR white dwarf sample is significantly less biased than the sample observed by the Sloan Digital Sky Survey, which is skewed to bluer and therefore hotter white dwarfs, making DESI more complete and suitable for performing statistical studies of white dwarfs.

Key words: techniques: spectroscopic – catalogues – surveys – white dwarfs.

1 INTRODUCTION

White dwarfs are the stellar remnants left over from the evolution of main-sequence stars born with masses $\leq 8\,M_\odot$ (Iben, Ritossa & Garcia-Berro 1997; Dobbie et al. 2006). Sustained against gravity by the pressure of degenerate electron gas, white dwarfs are Earth-sized and intrinsically faint objects. White dwarfs emerge from the giant branch evolution of their progenitors extremely hot (with effective temperatures $T_{\rm eff} \simeq 10^5$ K), but in the absence of nuclear fusion, they gradually cool. Throughout their evolution, white dwarfs have similar optical colours as much more luminous and distant quasars and main-sequence stars. Consequently, the selection of foreground white dwarfs has been difficult against the much more numerous background contaminants.

Early samples were based on proper motion searches (e.g. Giclas, Burnham & Thomas 1965), and while they were fairly representative of the intrinsic white dwarf population, only yielded a few hundred confirmed white dwarfs. Photometric surveys for blue-excess objects and individual follow-up spectroscopy identified ~ 1000 white dwarfs (Green, Schmidt & Liebert 1986; Homeier et al. 1998; Christlieb et al. 2001). However, these samples were heavily biased towards hot ($T_{\rm eff} \gtrsim 10\,000$ K) and young ($\lesssim 1$ Gyr) systems. Major progress was made possible by wide-area multi-object spectroscopic surveys, including the Two-degree-Field Galaxy Redshift Survey (Vennes et al. 2002), the Large Sky Area Multi-Object Fiber Spectroscopic Telescope Survey (Guo et al. 2015), and the Sloan Digital Sky Survey (SDSS; Kleinman et al. 2004, 2013; Eisenstein et al. 2006; Kepler et al. 2021), with the latter producing the largest and most homogeneous white dwarf sample to date. Yet, even the SDSS white dwarf sample was still subject to complex selection effects (Richards et al. 2002; Kleinman et al. 2004), as white dwarfs were targeted serendipitously.

An unbiased selection of white dwarfs became only possible with photometry and astrometry from *Gaia*, leading to a deep ($G \simeq 20$) and homogeneous all-sky sample of $\simeq 359\,000$ high-confidence

★ E-mail: paulaizquierdosanchez@gmail.com

© 2024 The Author(s).
Published by Oxford University Press on behalf of Royal Astronomical Society. This is an Open Access article distributed under the terms of the Creative Commons Attribution License (https://creativecommons.org/licenses/by/4.0/), which permits unrestricted reuse, distribution, and reproduction in any medium, provided the original work is properly cited.

Downloaded from https://academic.oup.com/mnras/article/535/1/254/7774399 by guest on 09 December 2024

white dwarf candidates (Gentile Fusillo et al. 2019, 2021; hereafter GF19 and GF21, respectively). Follow-up spectroscopy is essential to both confirm the white dwarf nature of these candidates, and determine their physical properties.

Research areas making use of large samples of white dwarfs with accurately determined characteristics include, but are not limited to:

(i) the spectral evolution of white dwarfs as they age (Koester 1976; Pelletier et al. 1986; Bergeron et al. 1990; Althaus et al. 2005; Cunningham et al. 2020; Rolland, Bergeron & Fontaine 2020; Bédard, Bergeron & Brassard 2022; Camisassa et al. 2023; Blouin, Bédard & Tremblay 2023a),

(ii) the composition and evolution of planetary systems (Zuckerman & Becklin 1987; Jura 2003; Zuckerman et al. 2007; Gänsicke et al. 2012; Vanderburg et al. 2015; Zuckerman 2015; Schreiber et al. 2019; Swan et al. 2019, 2024; Hollands et al. 2021; Izquierdo et al. 2021; Kaiser et al. 2021; Klein et al. 2021; Trierweiler, Doyle & Young 2023; Rogers et al. 2024),

(iii) the effects of magnetic fields in the range of $\simeq 10^2$–10^6 kG on the atom and stellar atmospheres (Kemp et al. 1970; Angel et al. 1974b; Reid, Liebert & Schmidt 2001; Schimeczek & Wunner 2014a, b; Manser et al. 2023; Reding et al. 2023; Hardy, Dufour & Jordan 2023a, b),

(iv) the physics of accretion discs in isolated and binary systems (Kraft 1962; Tapia 1977; Horne & Marsh 1986; Marsh & Horne 1988; Gänsicke et al. 2009; Manser et al. 2016, 2021; Cauley et al. 2018; Steele et al. 2021; Cunningham et al. 2022; Inight et al. 2023; Okuya et al. 2023), and

(v) the processes of energy transfer in, and modelling of white dwarf atmospheres (Koester 2010; Tremblay et al. 2011, 2019b; Bauer & Bildsten 2018; Blouin, Dufour & Allard 2018; Cukanovaite et al. 2018; Cunningham et al. 2019; Bédard et al. 2020).

Spectroscopic follow-up of the *Gaia* white dwarf candidate sample will be obtained as part of four of the next generation multi-object spectroscopic surveys. While the William Herschel Telescope Enhanced Area Velocity Explorer (Dalton et al. 2012, 2016) and the 4-metre Multi-Object Spectroscopic Telescope (de Jong et al. 2016) are expected to come online in the near future, SDSS-V (Kollmeier et al. 2017; Almeida et al. 2023) and the Dark Energy Spectroscopic Instrument (DESI; DESI Collaboration 2016a, b, 2024b) survey are already collecting white dwarf spectra. The DESI survey obtained commissioning and survey validation observations from 2020 December 14 to 2021 June 10 (DESI Collaboration 2024a), which have been released as the DESI Early Data Release (EDR; DESI Collaboration 2024b). The data observed in this release include more than 4000 white dwarf candidates.

In this paper, we present the DESI EDR sample of white dwarfs and associated systems. We describe the observations used in this work in Section 2. We then describe how we constructed the DESI EDR white dwarf sample in Section 3, and broadly describe the subsystems included along with a comparison to the SDSS in Section 4. In Section 5, we give a more detailed discussion and analysis of white dwarf subtypes of interest, and conclude with our findings in Section 6.

2 OBSERVATIONS

2.1 DESI

DESI on the Mayall 4-m telescope at Kitt Peak National Observatory is a multi-object spectroscopic instrument capable of collecting fibre spectroscopy on up to $\simeq 5000$ targets per pointing (DESI Collaboration 2022). The fibres are positioned by robot actuators and are grouped into 10 petals which feed 10 identical three-arm spectrographs, each spanning 3600–9824 Å at a full width at half maximum resolution of $\simeq 1.8$ Å. The inter-exposure sequence that includes telescope slewing, spectrograph readout, and focal plane reconfiguration can be completed in as little as $\simeq 2$ min (DESI Collaboration 2022). The acquired data are then wavelength- and flux-calibrated with the DESI processing and reduction pipeline (for a full description, see Guy et al. 2023).

The DESI survey started main-survey operations on 2021 May 14 and will obtain spectroscopy of more than 40 million galaxies and quasars over 5 yr to explore the nature of dark matter. During suboptimal observing conditions (e.g. poor seeing or high lunar illumination), observations switch focus to nearby bright galaxies (Ruiz-Macias et al. 2020; Hahn et al. 2022) and stars (Allende Prieto et al. 2020; Cooper et al. 2023). As part of this bright-time programme, the DESI survey is targeting white dwarfs.

2.1.1 *DESI targeting of white dwarfs*

The target selection of white dwarfs for the DESI survey is described in Cooper et al. (2023, section 4.4.1). For the main survey, these selection criteria use *Gaia* DR2 photometry and *Gaia* EDR3 astrometry, and are based on equations (1)–(7) defined in GF19. DESI EDR observations also follow these same criteria but use *Gaia* DR2 astrometry. Applying the white dwarf target selection within the DESI footprint results in 66 811 white dwarf candidates, where over 99 per cent of these targets are expected to be allocated a fibre during the main survey (see fig. 1 and table 2 of Cooper et al. 2023). However, as fibre assignment is done on the fly immediately before an observation is made, the details of what individual white dwarfs are observed by DESI is not predictable in advance (Schlafly et al. 2023).

Targets selected as white dwarf candidates can be easily identified by their target bitmask (as detailed in Myers et al. 2023; DESI Collaboration 2024b), and 3437 of them were assigned fibres as part of the DESI EDR sample. We additionally cross-matched the entire DESI EDR sample with the GF19*Gaia* DR2 white dwarf catalogue using the unique *Gaia* DR2 source ID to identify additional white dwarf candidates that may have been observed by other programs in the main survey. This resulted in an additional 627 targets, for a total number of 4064 DESI EDR white dwarf candidates.

The majority of white dwarfs targeted in the DESI EDR were observed more than once, and for the construction of the white dwarf catalogue we produced uncertainty-weighted co-adds using all the individual exposures for each white dwarf candidate and combined all spectra obtained in each of the three spectral arms. Across the 4064 white dwarf candidates targeted, a total of 31 842 single-object exposures were obtained. However, during commissioning and the early parts of survey validation some observed spectra were of poor quality, leading to 4852 exposures with a median signal-to-noise ratio < 0.5 in all three spectral arms. As a result, 391 white dwarf candidates observed during DESI EDR had unusable spectroscopy, resulting in a set of 3673 white dwarf candidates with usable spectra.

2.1.2 *Known issues with DESI EDR spectral calibration*

There are two known instrumental and processing issues that affect a small subset of DESI spectroscopy (Fig. 1):

Sensitivity at$\simeq 4300$ Å. The reflectivity of the collimators in the blue arm of the DESI spectrographs is reduced in the wavelength range $\simeq 4200$–4400 Å, resulting in a drop in sensitivity in that region

Downloaded from https://academic.oup.com/mnras/article/535/1/254/7774399 by guest on 09 December 2024

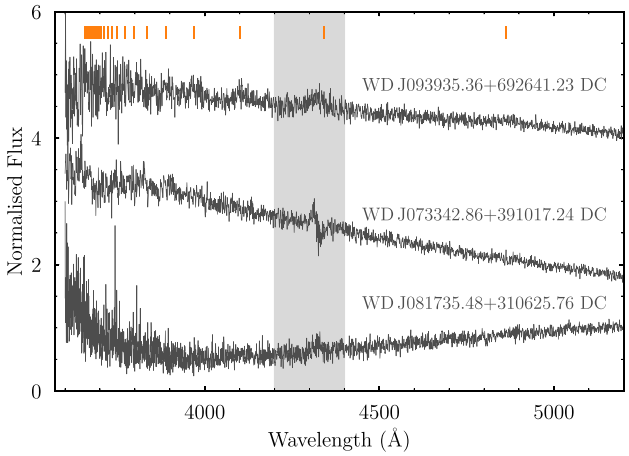

Figure 1. Three featureless DC (see Table 1) white dwarfs identified in the DESI EDR sample showcasing some of the spectral issues affecting a small number of systems. The Balmer series up to the Balmer jump are marked with short vertical lines, and the vertical region covering the wavelength range 4200 Å $< \lambda <$ 4400 Å highlights the region where the spectrograph collimator coating has reduced reflectivity and calibration residuals.

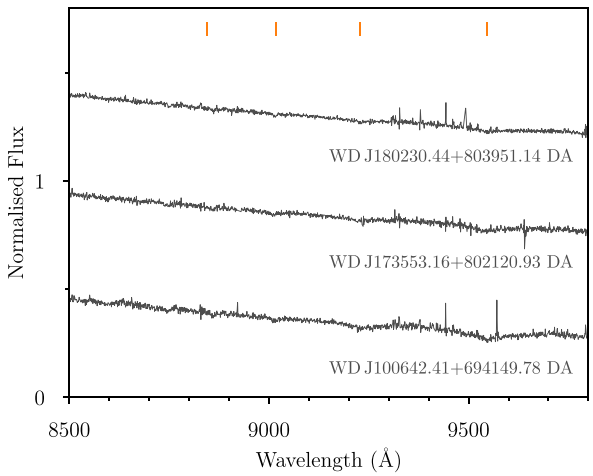

Figure 2. Three DA (see Table 1) white dwarfs identified in the DESI EDR sample showcasing some of the wide Paschen absorptions, marked with short vertical tabs.

(see fig. 24 of Guy et al. 2023). The exact shape of the reflectivity profile as a function of wavelength varies with the location in the mirror and with the incidence angle of the light. This sensitivity issue affects both the flux calibration and the sky subtraction and can result in the creation of non-physical continuum shapes in this region, such as in the DESI spectrum of WD J073342.86+391017.24 (Fig. 1).

Flux calibration. The flux calibration of DESI is performed using F-stars with a preference for low-metallicity halo stars. Guy et al. (2023) used hydrogen-atmosphere DA white dwarfs as an independent test of the flux calibration. For the majority of the DESI spectral range the average residuals are relatively flat at a level of $\simeq$ 2 per cent (see fig. 41 of Guy et al. 2023). However, around the Balmer and Paschen series emission and absorption features are present in the average residuals, which are suggestive of an imperfect fit to the spectral features of the standard stars. This is most notable at wavelengths $\simeq$ 3750 Å, where a $\simeq$ 6 per cent jump coincides with the Balmer jump. For some very cool white dwarfs (i.e. the featureless DC white dwarfs), this increase in flux can appear quite dramatic and starts affecting the spectrum at redder wavelengths. While some features in the average residual from fitting DAs are likely due to imperfections in the white dwarf models, such as the very broad ($\sim$ 100 Å) Paschen absorption features (Fig. 2), many of the other features are reproduced in the continuum fitting of moderate redshift quasars observed by DESI, highlighting these as calibration issues (see fig. 5 of Ramírez-Pérez et al. 2023).

2.2 SDSS

The SDSS has been taking multiband photometry and multifibre spectroscopy since 2000, using a 2.5-m telescope located at the Apache Point Observatory in New Mexico (Gunn et al. 2006). We retrieved archival SDSS spectroscopy (DR17; Abdurro'uf et al. 2022) and cross-matched these with the DESI EDR sample of white dwarf candidates, which resulted in 1427 unique sources common to both surveys and a total of 2149 SDSS spectra. We use these SDSS spectra to validate our fitting routines (Section 5) using different spectroscopic sources for the same target and comparing with previous literature results.

2.3 Photometry

2.3.1 Multicolour photometry

We retrieved photometric data from four catalogues, namely *Gaia* DR2, *Gaia* EDR3, SDSS DR18, and Pan-STARRS DR2 (Chambers et al. 2019). Zero-point corrections were applied to the SDSS *u*, *i*, and *z* bands as suggested by Eisenstein et al. (2006) to convert to actual AB magnitudes. *Gaia* DR2 photometry and astrometry was used for the target selection in the DESI EDR and for our cross-match to identify potential white dwarf candidates observed through other target selections (see Section 3). *Gaia* EDR3 (or DR2 if the former was not available) photometry was employed to compare our internal photometric analysis with an independent test.

2.3.2 Zwicky Transient Facility

Zwicky Transient Facility (ZTF) is a robotic time-domain survey using the Palomar 48-inch Schmidt Telescope (Bellm et al. 2019; Masci et al. 2019). Utilizing a 47 deg^2 field of view, ZTF can scan the entire sky in $\simeq$ two days, making it a powerful survey for identifying photometrically variable sources at optical wavelengths. We obtained archival ZTF data from DR18 (Masci et al. 2019), which includes data up to 2023 May 7. We inspected the ZTF light curves of cataclysmic variables (CVs) identified in the DESI EDR sample to assist in their classifications (Section 5.5).

3 WHITE DWARF CATALOGUE

3.1 Spectral classification

The spectral classification system for white dwarfs has been defined by Sion et al. (1983), and is purely based on the morphology of the spectroscopic data. We summarize in Table 1 the identifiers associated with specific features in the spectrum of a white dwarf, which relate both to the chemical composition of the atmosphere, as well as to other characteristic features that may be present in the

Downloaded from https://academic.oup.com/mnras/article/535/1/254/7774399 by guest on 09 December 2024

Table 1. Description of the identifiers for the varied spectral features detected in DESI EDR white dwarf spectra. A white dwarf spectral class is given the degenerate 'D' prefix, with any combination of features that are present, for example 'DA', 'DABZ', or 'DBH'. The top six identifiers relate to the chemical composition of the atmosphere, the next four are used to label additional characteristics of the spectra. Systems we could identify as white dwarfs but could not further classify were given the classification 'WD'.

Identifier	Definition
A	H I lines present
B	He I lines present
C	Featureless spectrum
O	He II lines present
Q	C features present in atomic or molecular form
Z	Metal lines present[a]
P	Peculiar or unidentified features
H	Zeeman-splitting present
e	Emission lines present
:	Tentative or uncertain classification

[a]Some of these detections may include ISM absorption features, which is more common for hotter white dwarfs at larger distances.

spectra. The majority of white dwarfs in any magnitude or volume-limited sample are 'DA' white dwarfs, that is, their spectra only show Balmer absorption lines. Spectral identifiers can be combined if multiple features are identified, resulting in composite spectral types such as 'DBAZ'. The original definition of Sion et al. (1983) defined that 'weaker or secondary spectroscopic features' are used for additional spectral identifiers, leaving a fair amount of ambiguity with respect to deciding the sequencing of the spectral type. We adopted an overall weighted visual assessment of the different spectral features, rather than focusing on the strength of specific individual lines. It is important to note that the equivalent width (EW) of features of a specific element are not directly linked to its abundance within the atmosphere, hence care has to be taken not to mistake spectral types as a reflection of the dominant species within the atmosphere of a given white dwarf. The 391 white dwarf candidates with unusable DESI spectra were given a NULL classification.

The 3673 DESI EDR spectra of white dwarf candidates were visually classified by three of the authors, who carefully reviewed all systems where their initial classifications were discrepant, followed by a final inspection of all spectra within any individual spectral class. In total, we spectroscopically confirm 2706 white dwarfs. We also provide classifications for 66 binary white dwarf systems, including white dwarf–main-sequence binaries (WD + MS), CVs, and double-degenerate binaries such as the DA + DQ system WD J092053.05+692645.36 (hereafter WD J0920+6926) are discussed in Section 4.2. We also identified 817 contaminant extragalactic sources, main-sequence stars and subdwarfs, with an additional 84 spectra that could not be confidently classified. These classifications are listed in Table 2, and some example DESI spectra of white dwarf systems are shown in Fig. 3.

The DESI EDR white dwarf catalogue is provided as a FITS file,[1] with the details of the extensions included and the content of the individual columns described in detail in Appendix A. The first extension contains the full list of 4064 white dwarf candidates targeted by DESI with our spectral classifications (where applicable) and auxiliary data. The second extension includes the results of our cross-match between the DESI EDR sample and SDSS with 2149 entries giving the unique SDSS plate, modified Julian date (MJD), fibre identifiers for each SDSS spectrum, the separation between a given white dwarf candidate and the location associated with the SDSS spectrum, and the number of spectra associated with each object. Subsequent extensions include our best-fitting parameters to the DA, DB, DBA, and DQ systems and the surface-average field strengths for the magnetic objects.

[1]This FITS file can be obtained at https://zenodo.org/records/13684288.

3.2 New identifications versus known systems

To determine the percentage of new white dwarfs the DESI EDR sample has identified, we cross-matched our sample with the Montreal White Dwarf Database (MWDD, Dufour et al. 2017) and the SIMBAD astronomical database (Wenger et al. 2000). The results of this cross-match are included in our DESI EDR catalogue (Table A1), and in the discussion of spectral types and subclasses below we exclude systems within the DESI EDR with uncertain (:) classifications. For the largest sample of systems, that is, DA, DB, and DC white dwarfs, we use the results of our cross-match to determine which white dwarfs have been identified as such for the first time. 61 per cent of DAs, 77 per cent of DCs, 48 per cent of DBs, 31 per cent of DAB/DBAs, and 27 per cent of DAO/DOs have been spectroscopically confirmed as a white dwarf for the first time with DESI, adding well over 1000 new systems. This is somewhat expected from the cooler distribution of DESI white dwarfs compared to the SDSS sample (Fig. 9), where DCs and DAs are the dominant spectral types. As SDSS preferentially samples hotter white dwarfs, the DB, DAB/DBA, and DAO/DO subclasses are better examined and fewer new systems have been identified by DESI.

We do a more in-depth literature search for four subgroups of interest to us; DQ white dwarfs (Section 5.2, Table C1), metal-enriched systems (Section 5.3, Table D1), magnetic white dwarfs (Section 5.4, Table E1), and CVs (Section 5.5, Table F1). In these searches, we identify whether DESI has newly discovered (or confirmed in the case of candidates in the literature) these white dwarfs as members of their given subclasses, and discuss them in more depth in the given sections.

4 THE DESI EDR WHITE DWARF SAMPLE IN THE CONTEXT OF THEIR LOCATION ON THE *GAIA* HRD

We illustrate the distribution of the DESI EDR white dwarf sample within the *Gaia* Hertzsprung–Russell diagram (HRD) in Fig. 4 separated into spectroscopically confirmed white dwarf systems (including binaries, left) and contaminants (right), with the 84 unclassified systems ('UNCLASS') being omitted (see Table 2). The DESI EDR white dwarf sample closely follows the distribution of the magnitude-limited sample of high confidence (probability of being a white dwarf $P_{\rm WD} > 0.95$) white dwarfs identified in the *Gaia* EDR3 catalogue of GF21. The DESI white dwarf sample overlaps with the A and B branches, populated by standard-mass white dwarfs with H- and He-dominated photospheres, respectively (Gaia Collaboration 2018). Some contribution from the Q-branch is also apparent in the sample (Gaia Collaboration 2018), which is thought to be due to delayed cooling by crystallization of high-mass white dwarfs (Tremblay et al. 2019b), settling of ^{22}Ne (Cheng, Cummings & Ménard 2019), or white dwarf–subgiant mergers (Shen, Blouin & Breivik 2023). The majority of white dwarf systems observed by DESI have high $P_{\rm WD}$ values in both GF19 and GF21. The $P_{\rm WD}$ variable was estimated based on the probability of a candidate being

Downloaded from https://academic.oup.com/mnras/article/535/1/254/7774399 by guest on 09 December 2024

Table 2. Classifications[a] of the white dwarf candidates from the DESI EDR. The NULL class was not visually inspected (see the text).

Class	Number	Class	Number	Class	Number	Class	Number	Class	Number	Class	Number
White dwarfs	2706	DAH:	12	DBAZ	4	DAe:	5	DQZ	1	Contaminants	817
DA	1958	DQ	50	DBAZ:	3	DAHe	2	DZAP	1	EXGAL	445
DA:	18	DQ:	5	DH:	6	DAHe:	2	DZBA	1	STAR	329
DC	197	DZ	49	DZA	6	DAZe:	1	DZBA:	2	sdX	42
DC:	23	DBZ	19	DZAB	4	DAOH:	1	DZQ	1	sdX:	1
DB	141	DBA	15	DZB	4	DAQ:	1	WD	20	UNCLASS	84
DB:	6	DBA:	1	DCH:	3	DAZH:	1	Binaries	66	NULL	391
DAZ	54	DAO	10	DAP	2	DO	1	WD + MS	53		
DAZ:	11	DAO:	1	DAB	1	DQA	1	CV	12		
DAH	53	DBZA	7	DABZ	1	DQH	1	DA + DQ	1		

[a]In the text, we present classifications such as D(AB), where bracketed subclassifications collate any permutation of the spectral classifications, for example, D(AB) includes both DAB and DBA white dwarfs.

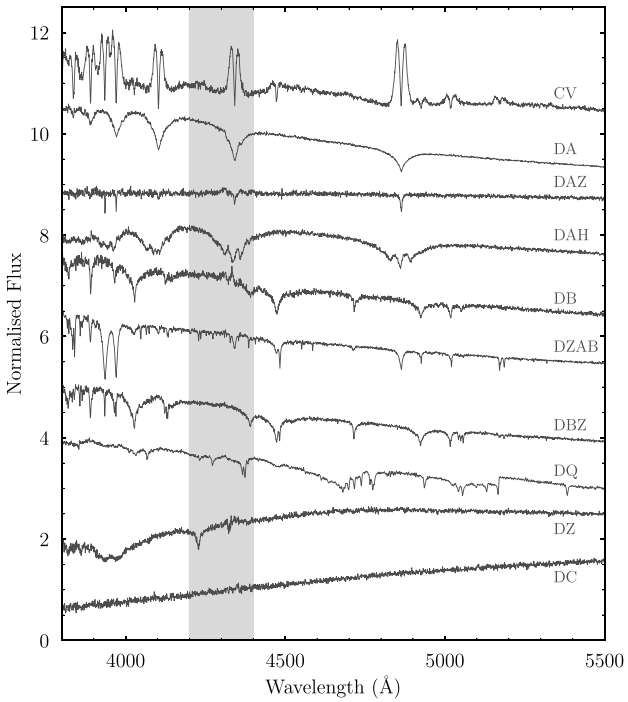

Figure 3. A subset of the white dwarf systems spectra within the DESI EDR showcasing some of the spectral types. The wavelength range 4200 < λ < 4400 Å is subject to relatively poor calibration due to an issue with the spectrograph collimator coating. Adapted from Cooper et al. (2023).

an isolated white dwarf, and so the binary sample that dominates the systems that sit above the white dwarf cooling track have a lower $P_{\rm WD}$. The contaminants are similarly located above the white dwarf cooling track, with many of them having very small $P_{\rm WD}$ values. Additionally between the construction of the GF19 and GF21 catalogues, 714 (87.3 per cent) of the contaminant population have been excluded from the more reliable *Gaia* EDR3-based selection criteria of GF21 compared with that of DR2 used by GF19, whereas only 14 (0.5 per cent) of the confirmed white dwarf systems have dropped out of the GF21 white dwarf catalogue (Fig. G1). Overall, this showcases both the high fidelity of the selection methods and the robustness of the $P_{\rm WD}$ value calculated by GF19 and GF21.

In the following subsections, we will describe the DESI EDR white dwarf sample within the *Gaia* HRD, split up into the various spectral classes (Table 2). The systems are loosely grouped to illustrate the evolution of hydrogen-dominated atmospheres (DA → DC) and helium-dominated atmospheres (DO → DB → DC/DQ), as well as classes that share similar physical characteristics (e.g. metal enrichement, the presence of magnetic fields or binary companions). These groupings are not fully representative however, as some white dwarf classes may be populated by multiple evolutionary channels, such as DC white dwarfs evolving from both H- and He-dominated atmosphere white dwarfs (Bergeron 2001; Kowalski & Saumon 2006; Kilic et al. 2009; Caron et al. 2023), as well as different physical processes that can alter the spectral type of a white dwarf, such as convective mixing or accretion from various sources (Fontaine, Brassard & Bergeron 2001; Gentile Fusillo et al. 2017; Rolland, Bergeron & Fontaine 2018; Cunningham et al. 2020; Rolland et al. 2020). Cooling tracks[2] for DA- and DB-type white dwarfs are presented to help give context to the samples, but are not applicable to all objects.

4.1 Typical white dwarfs

Fig. 5 shows the majority of the white dwarf sample, which is dominated by the DA, DC, and DB spectral types, adding up to a total of 86.3 per cent of the DESI EDR confirmed white dwarfs. The DAs make up 72.8 per cent of the sample, and cover the majority of the cooling sequence. A small subset of high-mass DAs lie on the Q-branch described above. DA white dwarfs cool until they reach ≃ 5000 K when the Balmer lines become undetectable and these systems transition to featureless DCs.

While He-dominated atmosphere white dwarfs cool along a similar path in the *Gaia* HRD, their spectral evolution through this cooling sequence is more complex. The hottest pure He-atmosphere white dwarfs in our sample are the DO systems that show He II lines in their spectra and are thought to form after a late shell flash in which the white dwarf progenitor burns all the remaining H in the envelope (Herwig et al. 1999; Althaus et al. 2005; Werner & Herwig 2006) or through the convective dilution or convective mixing processes, in which a thin H layer is diluted by the deeper convective He one (Fontaine & Wesemael 1987; Cunningham et al. 2020). As DO white dwarfs cool, they can either transition into a DB as He becomes neutral and produces He I features (∼ 1/3 of DOs follow this path) or into a DA, following the DO-to-DA transition due to the upward diffusion of leftover H (Wesemael & Fontaine 1985; Fleming, Liebert & Green 1986; Liebert 1986). As DBs cool further (first path), He I features disappear below ≃ 10 000 K, and these white dwarfs then split into two categories: those with featureless

[2]http://www.astro.umontreal.ca/~bergeron/CoolingModels

Downloaded from https://academic.oup.com/mnras/article/535/1/254/7774399 by guest on 09 December 2024

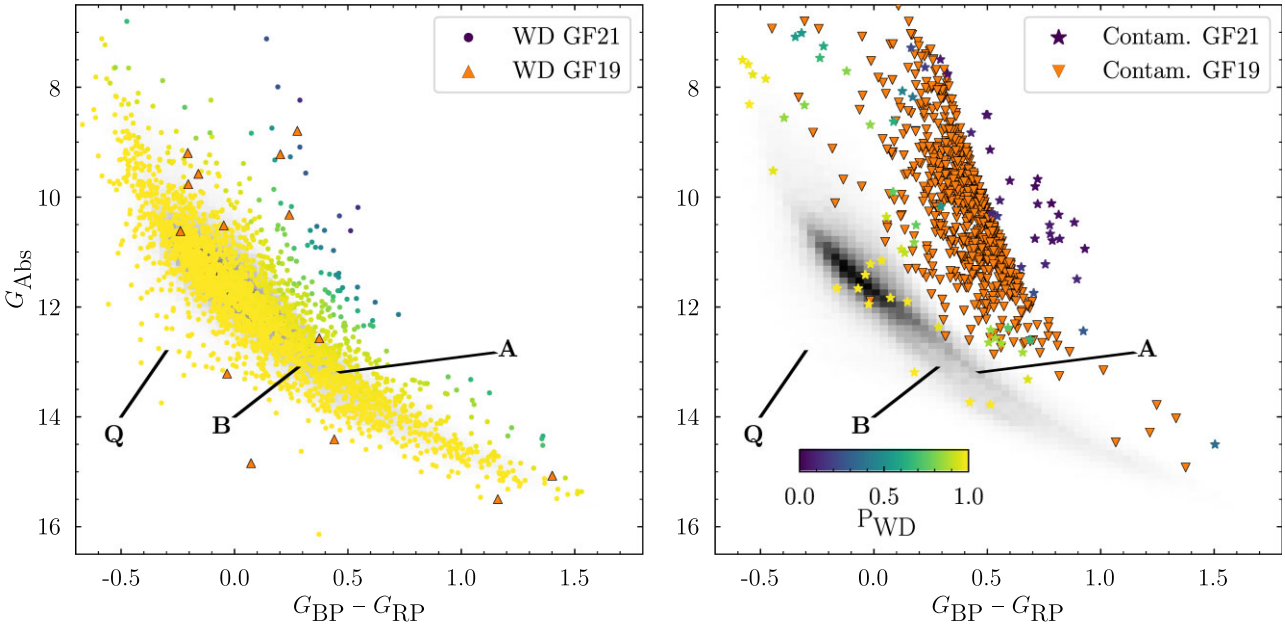

Figure 4. The *Gaia* HRD showing spectroscopically confirmed white dwarf systems (left panel) and contaminants (right panel), observed by DESI. For reference, the high-confidence ($P_{\rm WD} > 0.95$) sample of *Gaia* EDR3 white dwarfs from GF21 brighter than $G = 20$ are shown as a 2D grey-scale histogram in both panels, although it is completely obscured by the DESI EDR white dwarf sample in the left panel. DESI-identified white dwarf systems and contaminants with entries in the GF21*Gaia* EDR3 white dwarf catalogue are denoted as circles and stars in the left and right panels, respectively. 14 white dwarf systems and 714 contaminants do not have entries in the GF21*Gaia* EDR3 catalogue and only appear in the GF19*Gaia* DR2 white dwarf catalogue and we plot them as up-facing (left panel) and down-facing (right panel) orange triangles with a black edge colour. White dwarf systems and contaminants are coloured based on their probability of being a white dwarf, $P_{\rm WD}$, from GF21. The A, B, and Q branches defined in Gaia Collaboration (2018) are indicated by black lines (see the text). The sharp upper edge in the distribution of the contaminants is due to the selection criteria defined by GF19 (see their fig. 1).

DC spectra, and those showing the presence of C, that is, DQ white dwarfs. The existence of C in the spectra of these white dwarfs is thought to be due to dredge-up, when the deepening He convection zone reaches the C-rich core (Pelletier et al. 1986). Not all DQ white dwarfs appear to share this origin however, as a number sit on the Q-branch, suggesting they are both hotter and have a higher mass. These 'warm' or 'hot' DQs are thought to form instead from binary mergers (Dunlap & Clemens 2015; Kawka, Ferrario & Vennes 2023). Many He-atmosphere white dwarfs also show spectroscopically detectable H in their atmospheres, such as the DAO/DOA and DAB/DBA white dwarfs. These systems by-and-large overlap with those that do not show the presence of H.

The DC white dwarfs appear to group in two regions, with one group roughly between $0.00 < (G_{\rm BP} - G_{\rm RP}) < 0.75$, and the other appearing cooler at $(G_{\rm BP} - G_{\rm RP}) > 1.00$. The bluer sample of DCs is likely dominated by white dwarfs with He-rich atmospheres once He I lines stop being present in the spectra, and overlap with the cool DQ systems. Like their DQ counterparts, these bluer DCs likely also have trace C in their atmospheres:[3] while by definition they have featureless optical spectra, a large fraction of DCs experience some form of C dredge-up during their lifetime. This dredge-up is evidenced by non-negligible changes in their optical spectral energy distribution due to the addition of extra electrons from C (Camisassa et al. 2023; Blouin et al. 2023a), in addition to a reduction of their flux in the ultraviolet from C absorption (Blouin et al. 2023b). The redder sample of DCs is thought to be dominated by H-atmosphere white dwarfs where Balmer lines stop appearing in otherwise DA spectra, however these DCs appear to deviate quite significantly from the DA cooling sequence, which is centred roughly on the 0.6 $M_\odot$ evolutionary track. This may suggest imperfections in the cooling sequences used at these cooler temperatures (Caron et al. 2023), but the origin of this deviation is unknown. The gap between the two regions of DC white dwarfs as a function of temperature or colour has been previously identified as part of non-DA samples (Bergeron, Ruiz & Leggett 1997; Bergeron, Leggett & Ruiz 2001), although a recent study of the volume-limited 40 pc sample of white dwarfs does not reproduce two distinct regions (O'Brien et al. 2024).

A single DC white dwarf, WD J095106.36 + 645400.46 (hereafter WD J0951+6454, Fig. 6), lies significantly below the main white dwarf cooling sequence and is the least luminous white dwarf in the DESI EDR white dwarf sample (with an absolute magnitude in Gaia G band of $G_{\rm Abs} \simeq 16$, and $G_{\rm Bp} - G_{\rm Rp} \simeq 0.38$). The system sits on the ultra-blue sequence of infrared faint targets identified by Kilic et al. (2020) and Bergeron et al. (2022). These systems appear to be comprised of relatively cool ($\simeq$4000 K) white dwarfs. The spectra of these systems are unusual due to the presence of collisionally induced absorption generated from molecular H colliding with He dominating the opacity (Borysow, Jorgensen & Fu 2001).

4.2 Exotic white dwarf systems

Fig. 7 showcases the rarer white dwarf systems and spectral types arising from interactions with external bodies or additional physical characteristics beyond the thermal evolution of white dwarfs depicted in Fig. 5. The top left panel of Fig. 7 displays all systems where metals (Z) heavier than helium, and excluding carbon, are spotted. We

[3]DC white dwarfs with evidence of trace C have been dubbed as 'stealth-DQs' and 'DQ-manqués'.

Downloaded from https://academic.oup.com/mnras/article/535/1/254/7774399 by guest on 09 December 2024

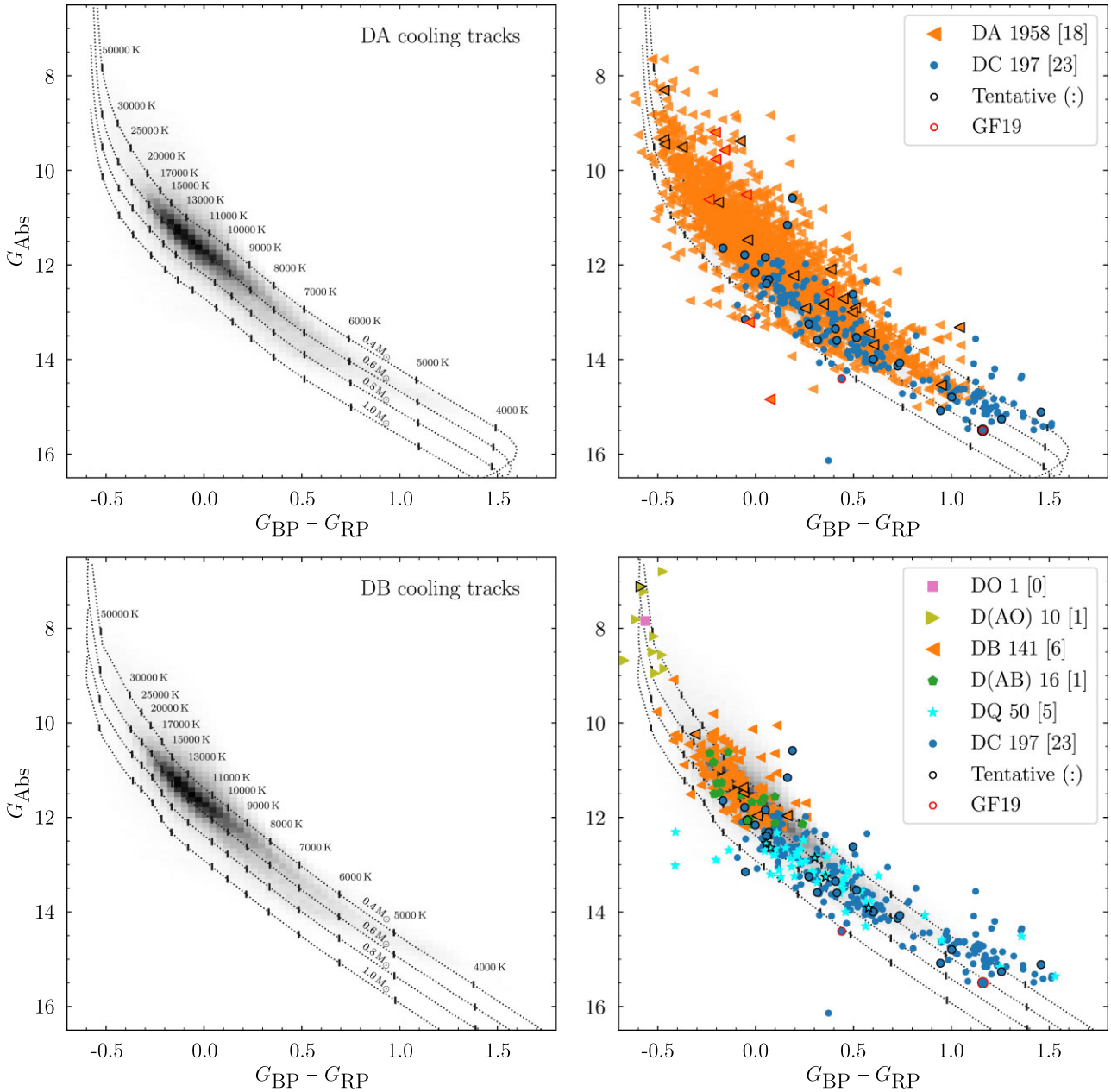

Figure 5. High-confidence ($P_{\rm WD} > 0.95$) *Gaia* white dwarfs brighter than $G = 20$ identified by GF21 are shown as a 2D grey-scale histogram in all panels. Left panels: cooling tracks from Bédard et al. (2020) for pure DA (top) and DB (bottom) white dwarfs are plotted as dashed lines for masses of 0.4, 0.6, 0.8, and 1.0 $M_{\odot}$ with vertical tabs highlighting $T_{\rm eff}$ values. Right panels: the same as the left panels, but with white dwarfs commonly associated with H- and He-dominated atmospheres identified by DESI (top and bottom, respectively). Bracketed classifications in the legend collate any combination of the spectral classifications, for example, D(AB) includes both DAB and DBA white dwarfs. The number of confidently classified white dwarfs associated with each classification are given, with the number of tentative (:) classifications provided additionally for each white dwarf type in square brackets. In both the top right and bottom right panels, tentatively identified systems are highlighted by a black border. Confirmed white dwarfs not present in GF21, but present in GF19 are highlighted by a red border. The spectrum of the very faint ($G_{\rm Abs} \simeq 16$), but blue ($G_{\rm Bp} - G_{\rm Rp} \simeq 0.38$) DC white dwarf, WD J0951+6454, is shown in Fig. 6.

identify a total of 152 metal-enriched white dwarfs, the vast majority of which are likely the result of the accretion of planetary material that survived the evolution of the post-main-sequence evolution planet-hosting main-sequence star (Zuckerman & Becklin 1987; Graham et al. 1990; Debes & Sigurdsson 2002; Jura 2003; Zuckerman et al. 2003). White dwarfs redder than $(G_{\rm BP} - G_{\rm RP}) > 0.1$, corresponding to $T_{\rm eff} \lesssim 12\,000$ K, dominate those with metal enrichment, which is more striking when additionally taking into account the magnitude-limited bias to hotter white dwarfs. The key reason for the apparent increase in the fraction of metal-enriched white dwarfs is the strength of the Ca H/K resonance lines, and the fact that Ca II is gradually becoming more populated in cooler atmospheres – resulting in a spectroscopic detection of Ca even at low photospheric abundances (Dufour et al. 2007b; Koester et al. 2011; Hollands et al. 2017; Hollands, Gänsicke & Koester 2018a). Observations of white dwarf samples at higher resolution and signal-to-noise ratios, and also in the

Downloaded from https://academic.oup.com/mnras/article/535/1/254/7774399 by guest on 09 December 2024

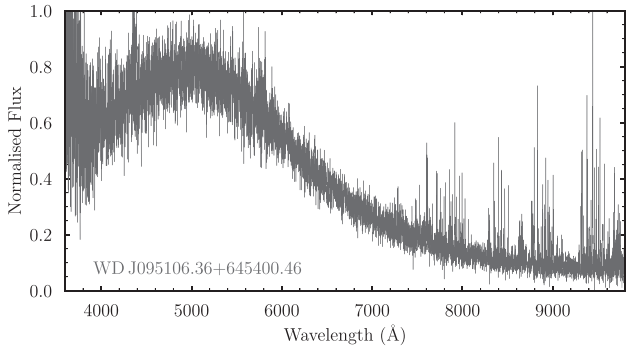

Figure 6. DESI EDR spectrum of the ultra-blue white dwarf WD J0951+6454. The steep increase in flux below $\simeq 3800$ Å is likely due to the calibration issues shown in Fig. 1. Additionally there are residual sky features in the red part of the spectrum past $\simeq 7500$ Å. The suppression of flux in the red part of the spectrum is due to collisionally induced absorption (Blouin, Kowalski & Dufour 2017).

far-ultraviolet (wavelengths below $\simeq 2000$ Å) where the detection of additional elements can be made, show that $\simeq 25-50$ per cent of all white dwarfs are enriched with metals consistent with the accretion of planetary bodies (Zuckerman et al. 2003, 2007; Barstow et al. 2014; Koester, Gänsicke & Farihi 2014).

We also identify 66 white dwarf binary systems which occupy a region that lies above the white dwarf cooling sequence due to the contribution of flux from two stars rather than one increasing the systems $G_{\rm Abs}$ (Fig. 7, top right panel). The majority of these systems are white dwarf–main-sequence binaries, where contributions from largely blue white dwarfs and red M dwarfs can be seen simultaneously in the DESI EDR spectra. Twelve of these systems are of the accreting binary CV type, of which five are newly confirmed (see Section 5.5), and are largely dominated by disc emission. The last system in this sample is a double white dwarf binary WD J0920+6926 (Fig. 8). The spectra of white dwarfs with both H and C in their spectrum (DAQ/DQA white dwarfs) usually show atomic C I lines which arise in hotter atmospheres and are thought to be, similar to the warm DQs, the product of binary mergers (Koester & Kepler 2019; Hollands et al. 2020; Kilic et al. 2024). However, WD J0920+6926 displays both weak and narrow Balmer lines, in addition to the molecular C Swan bands which are corroborated by the $T_{\rm eff}$ of 6250 ± 100 K we obtain from our spectroscopic fitting (see Section 5.2) that is much cooler than for the known DAQ/DQA systems. These arguments, along with its position above the white dwarf cooling sequence have led to our classification of this system as a DA+DQ system. Only one DA+DQ binary has previously been identified and characterized, NLTT 16 249 (Vennes & Kawka 2012; Vennes et al. 2012), making WD J0920+6926 an interesting target for follow-up observations.

The bottom left panel of Fig. 7 contains systems that either show evidence for Zeeman splitting of spectral features or are associated with magnetic fields. Only 56 white dwarfs in the sample have a confident detection of magnetic fields, with all but three of them being classed as DAH white dwarfs. The population of magnetic white dwarfs is dimmer and redder than what would be expected if they uniformly sample the magnitude-limited population of white dwarfs provided by *Gaia*, and is split into two populations. The first group of magnetic white dwarfs appears to follow the main white dwarf cooling track although slightly fainter suggesting that these white dwarfs are either bluer and/or heavier than their non-magnetic counterparts. The second population of magnetic white dwarfs lies close to, or on, the Q-branch. These systems appear to have higher masses than their redder counterparts and are likely the result of binary mergers (Regős & Tout 1995; Tout et al. 2008; Nordhaus et al. 2011; García-Berro et al. 2012; Wickramasinghe, Tout & Ferrario 2014).

In the bottom right panel of Fig. 7 we show the remaining white dwarf systems that did not nicely fall into the loose categories above, in addition to 20 systems we identified as white dwarfs but no further classification could be given.

4.3 Advantages over the SDSS white dwarf sample

The DESI survey has already observed over 47 000 white dwarf candidates (Manser et al. 2023), making it one of the largest surveys of white dwarfs to date, surpassing the $\simeq 30\,000$ white dwarfs observed by the SDSS (Harris et al. 2003; Kleinman et al. 2004, 2013; Eisenstein et al. 2006; Gentile Fusillo et al. 2015, 2019, 2021; Kepler et al. 2021). Most of the SDSS white dwarfs were serendipitously targeted as quasar candidates or blue-excess objects, resulting in strong selection effects with respect to the underlying galactic population of white dwarfs. The left panel of Fig. 9 compares the distribution of the *Gaia*–SDSS sample of spectroscopically confirmed isolated white dwarfs from GF21 (as contour lines) with the entire magnitude-limited sample of high-confidence ($P_{\rm WD} > 0.95$) white dwarf candidates from GF21 (grey 2D histogram). It can be clearly seen that the SDSS sample is heavily biased towards bluer, hotter white dwarfs, with very few systems extending past $(G_{\rm BP} - G_{\rm RP}) > 0.8$. Additionally, there is an overdensity of white dwarfs in the *Gaia*–SDSS sample around $0.25 < (G_{\rm BP} - G_{\rm RP}) < 0.6$. Conversely, the DESI EDR sample shows a much better agreement with the magnitude-limited sample of high-confidence white dwarf candidates. This should not be surprising given the DESI EDR white dwarf target selection was based on the sample selected by GF21, but highlights the selection effects within the SDSS sample.

The biases present in the SDSS white dwarf sample have been previously reported in other studies (e.g. section 5.2.1 of Gänsicke et al. 2009), and are mainly due to two broad selection effects:

(i) *Serendipitous discoveries in the SDSS quasar search*. The bulk of white dwarfs identified by SDSS were selected originally as blue quasar candidates, resulting in an excess of white dwarfs in the range $0.25 < (G_{\rm BP} - G_{\rm RP}) < 0.6$, corresponding (roughly) to a range of effective temperatures 7000 K$< T_{\rm eff} <$ 9000 K. This bias can be seen more clearly in Fig. 10, where the previously identified overdensity in the *Gaia*–SDSS sample, now in the range $-0.1 < (g - r) < 0.25$, overlaps with the sample of observed SDSS quasars. However, to reduce the total number of stars observed as part of the quasar search, the SDSS target selection adopted a number of exclusion boxes, which add further complexity to the biases affecting the SDSS sample (see section 3.5.1 in Richards et al. 2002 and section 5.2.1 in Gänsicke et al. 2009).

(ii) *Blue selection of white dwarfs*. Blue and hot ($T_{\rm eff} \gtrsim 12\,000$) were included as ancillary science targets for spectroscopy in SDSS III (Dawson et al. 2013) and, in smaller numbers as flux standards, in SDSS IV (Dawson et al. 2016), resulting in additional selection biases.

In summary, whereas SDSS provided a large number of spectroscopic observations of white dwarfs, it was subject to selection effects that are extremely difficult to quantify. As DESI follows up *Gaia* white dwarf candidates, which are only subject to a magnitude-limit, the forthcoming large sample of DESI white dwarfs will be very well suited for detailed statistical studies of their physical properties.

Downloaded from https://academic.oup.com/mnras/article/535/1/254/7774399 by guest on 09 December 2024

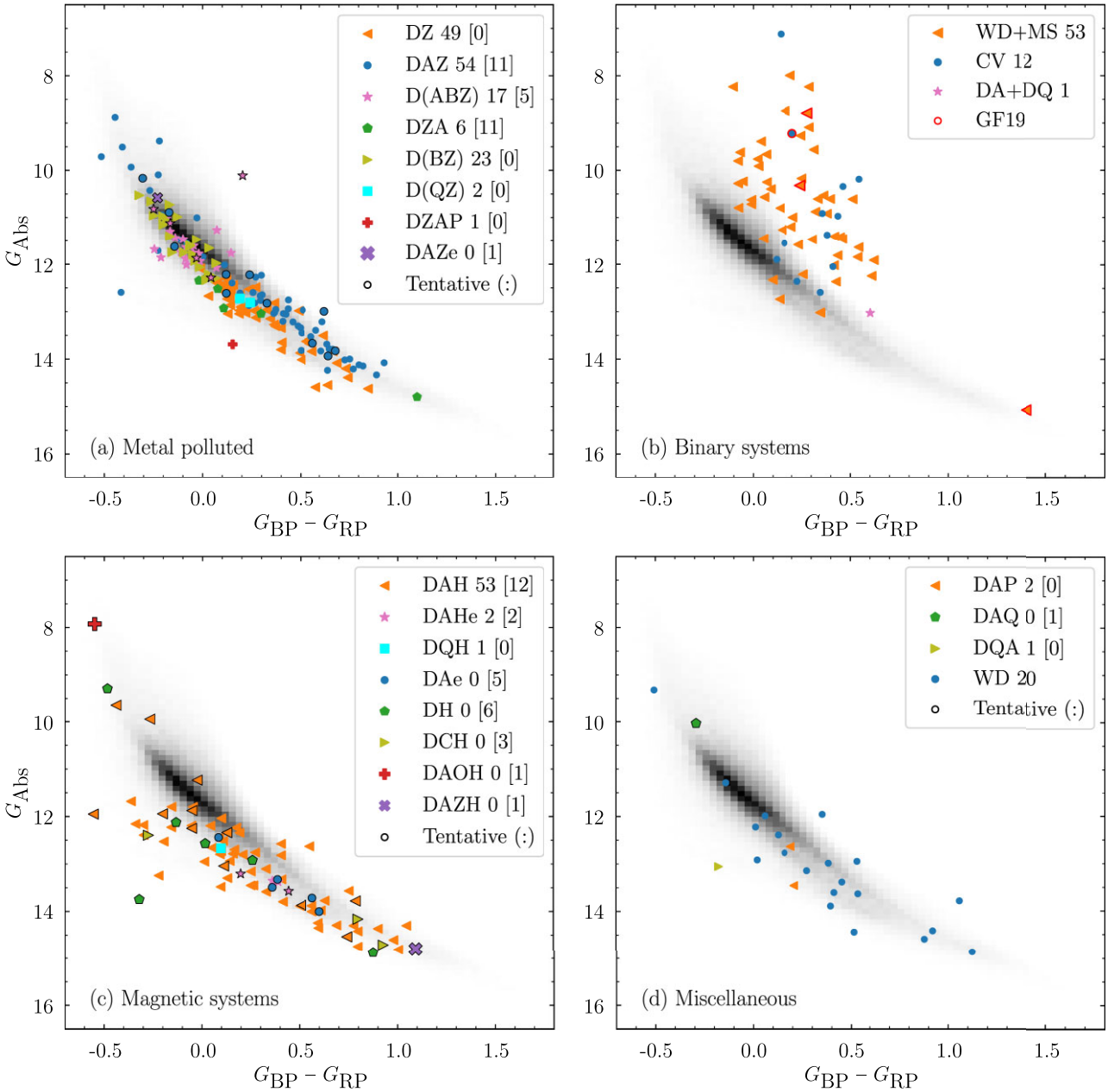

Figure 7. Same as Fig. 5 showing additional types of white dwarf systems identified by DESI with no cooling models presented. The number of confidently classified white dwarfs associated with each classification are given, with tentative (:) classifications given additionally in square brackets. (a) White dwarfs with metals present in the atmosphere commonly associated with the accretion of planetary material. (b) White dwarf binary systems. (c) White dwarfs showing evidence for hosting a magnetic field, including DAe white dwarfs, where the presence of emission is thought to be associated with magnetic fields (Elms et al. 2023). (d) Miscellaneous white dwarfs in addition to systems which were identified as a white dwarf but no further classification could be given.

5 WHITE DWARF SUBTYPE STUDIES

5.1 DA/DB/D(AB) model atmospheres and fitting procedure

The properties of the population can be determined if their stellar parameters ($T_{\rm eff}$ and $\log g$) are known. Nearly 80 per cent of the stars in the catalogue show spectral lines from only H or He (types DA, DAB, DB, and DBA), allowing reliable determination of their parameters by fitting white dwarf models to their data using established techniques. The methods we use and details of the spectral fitting process are described in depth in Appendix B. In summary, grids of synthetic spectra and photometry are generated using the atmosphere codes of Koester (2010), varying $T_{\rm eff}$, $\log g$, and (where appropriate) the H/He abundance, and applying reddening. Those variables are then fitted to the data in a Bayesian framework, treating distance as an additional free parameter constrained by the *Gaia* parallax and a prior tailored to a white dwarf population.

5.1.1 *The DA sample*

The distribution of $\log g$ as a function of $T_{\rm eff}$ drawn from the 1958 DAs within the DESI EDR spectra is presented in Fig. 11 (top panel).

This distribution should largely be smooth and closely follow the canonical value of $\log g = 8.0$ for DA white dwarfs. However, there

Downloaded from https://academic.oup.com/mnras/article/535/1/254/7774399 by guest on 09 December 2024

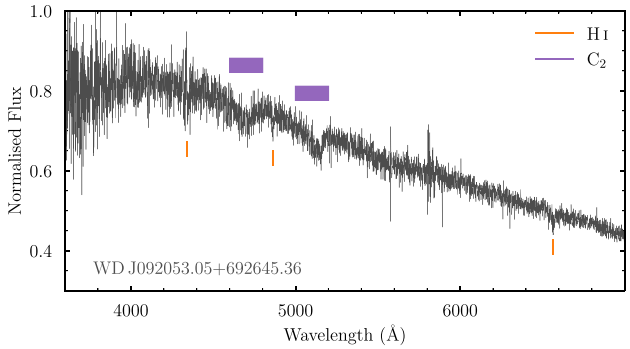

Figure 8. DESI EDR spectrum of the likely DA+DQ binary system WD J0920+6926. The system is located slightly above the white dwarf cooling sequence, suggestive of either being of low mass, or a binary, or both. DAQ/DQA white dwarfs are usually hotter and present atomic carbon features in their spectra. H Balmer lines and C_2 Swan bands are highlighted by vertical short tabs and horizontal bands, respectively.

are three clear deviations from this that we explain below: a scarcity of systems between 15 000 and 16 000 K, a small population of cool and massive systems, and a deviation from the canonical value of 8.0 for the cooler objects. These are artefacts related to the analysis with no physical meaning.

The clear decrease in the number of systems between 15 000 and 16 000 K is also present in other population studies (see e.g. Gianninas, Bergeron & Ruiz 2011; Genest-Beaulieu & Bergeron 2019) and coincides with the boundary between hot and cold solutions. In fact, we are using the maximum EW of Hβ line to choose between these two sets of solutions, but we have repeated this analysis for Hγ and Hδ. These two Balmer lines define new boundaries that move towards hotter temperatures, tentatively explaining the gap.

A group of unusually cool and (apparently) massive white dwarfs exists in a region around $T_{\rm eff} \simeq 6000$ K and $\log g \simeq 9.5$. Inspection of these spectra show unusually broad Balmer features, and these systems are likely helium-dominated atmosphere DAs. Detailed modelling of these stars is beyond the scope of this study, and they do not affect the overall conclusions we draw from the main population of DA white dwarfs.

In contrast, whereas the hotter white dwarfs are closely gathered around the canonical value of $\log g = 8.0$, their cooler counterparts ($T_{\rm eff} \lesssim 15\,000$ K) suffer from the so-called high-$\log g$ problem (Tremblay et al. 2010). This deviation is an artefact related to the spectroscopic fitting approach, since white dwarfs are expected to cool at constant radii and the abrupt change in $\log g$ is not seen in photometric studies. Tremblay et al. (2013) presented a grid of pure-H 3D model atmospheres with a correct treatment of the convection, and they demonstrated that the high-$\log g$ problem is related to the use of the 1D mixing-length (ML) approximation. Tremblay et al. (2013) derived analytical functions to convert spectroscopic 1D $T_{\rm eff}$ and $\log g$ to 3D atmospheric parameters, and while this correction was applied to the sample, a small deviation from the canonical $\log g = 8.0$ persists.

Below 10 000 K, the DA white dwarfs appear to deviate systematically below a value of $\log g = 8.0$, an issue which is currently unresolved with no clear discrepancies arising from comparisons with other methods and data sets (see Appendix B).

5.1.2 The DB and DBA samples

The spectroscopic parameters derived for the 141 DB white dwarfs within DESI EDR are displayed in Fig. 11 (bottom panel). The warmer stars ($T_{\rm eff} \geq 15\,000$ K) are closely clustered around $\log g \simeq 8$, the typical value for white dwarfs. This is not the case for the cooler objects where there is a known issue with the implementations of the broadening mechanisms for the neutral He, which results in fitted white dwarfs having unphysically high surface gravities (see e.g. Bergeron et al. 2011; Koester & Kepler 2015; Cukanovaite et al. 2021). Above $T_{\rm eff} \simeq 23\,000$ K, the $\log g$ values exhibit larger scatter: the spectroscopic parameters are difficult to estimate in the region where the EWs of the He I transitions reach their maximum (23 000 − 30 000 K) and this translates to less accurate parameters. Additionally, there are four objects with $T_{\rm eff} \simeq 27\,000$ K, which corresponds to the top boundary of the cool models, and likely have hotter temperatures.

5.2 DQ white dwarfs

The DESI EDR sample contains 55 DQ white dwarfs (Table C1), of which 43 are new discoveries (78 per cent). We fitted all DQ spectra following the methods of Koester & Kepler (2019), and using the models computed with the code of Koester (2010) with updates described in Koester, Kepler & Irwin (2020). We employed a cool DQ grid which spanned $T_{\rm eff} = 3000 - 12\,000$ K in steps of 250 K, $\log g = 7.25 - 9.75$ in steps of 0.25 dex and $\log$ C/He from −9.5 to −3.0 in steps of 0.5 dex. The warm and hot DQs were modelled with a grid spanning $T_{\rm eff} = 9000 - 30\,000$ K in steps of 250 K up to 20 000 K and steps of 1000 K above 20 000 K, $\log g = 7.0 - 9.5$ in steps of 0.25 dex, and $\log$ C/H from +4.0 to −4.0 in steps of 0.5 dex. The spectral appearance of DQ white dwarfs strongly depends on their effective temperature, with hotter white dwarfs showing atomic carbon lines and the cooler ones C_2 Swan bands (Fig. 12). Within the *Gaia* HRD, the hotter DQs are located on the Q-branch, and are correspondingly massive ($M_{\rm wd} > 1\,{\rm M}_\odot$, Table C1). In contrast, the cooler DQs largely lie on the standard cooling sequence, having average masses.

The C abundances show a strong anticorrelation with effective temperature (Fig. 13), following the trend found earlier by Coutu et al. (2019). It is noteworthy that the spectrum of the hottest DQ in the EDR sample, WD J085601.74+321354.51, is consistent with a C-dominated atmosphere.

We also identified two DQs that show traces of photospheric metals in addition to carbon: WD J101453.59 + 411416.94 and WD J142018.91 + 324921.12 (hereafter WD J1014 + 4114 and WD J1420+3249, respectively) which we classify as DZQ and DQZ, respectively (Fig. 14). The fraction of DQ white dwarfs that exhibit metals in their spectra is smaller than that among DA or DB white dwarfs. This is thought to be the result of an interplay between the accreted metals and the atmosphere structure, leading to the rapid transformation of DQ white dwarfs into DZ white dwarfs (Blouin 2022; Hollands et al. 2022).

Finally, we identified one DA+DQ double degenerate (WD J0920+6926, see Fig. 8 and Section 4.2) and detect Zeeman splitting in one of the warm DQs (WD J112513.32 + 094029.68, hereafter WD J1125+0940, see Fig. 17 and Section 5.4.1).

5.3 Metal line DxZ white dwarfs

Among the 152 DxZ (where 'x' is a placeholder for other spectral identifiers, e.g. A, B, and Q) white dwarfs that show metal lines in their DESI EDR spectra (Table D1) 121 are new discoveries (80 per cent) and 31 were previously known. This sample is very likely dominated by white dwarfs that are actively accreting, or have recently accreted planetary material (Zuckerman et al. 2003, 2007; Barstow et al. 2014; Koester et al. 2014; Wilson et al. 2019),

Downloaded from https://academic.oup.com/mnras/article/535/1/254/7774399 by guest on 09 December 2024

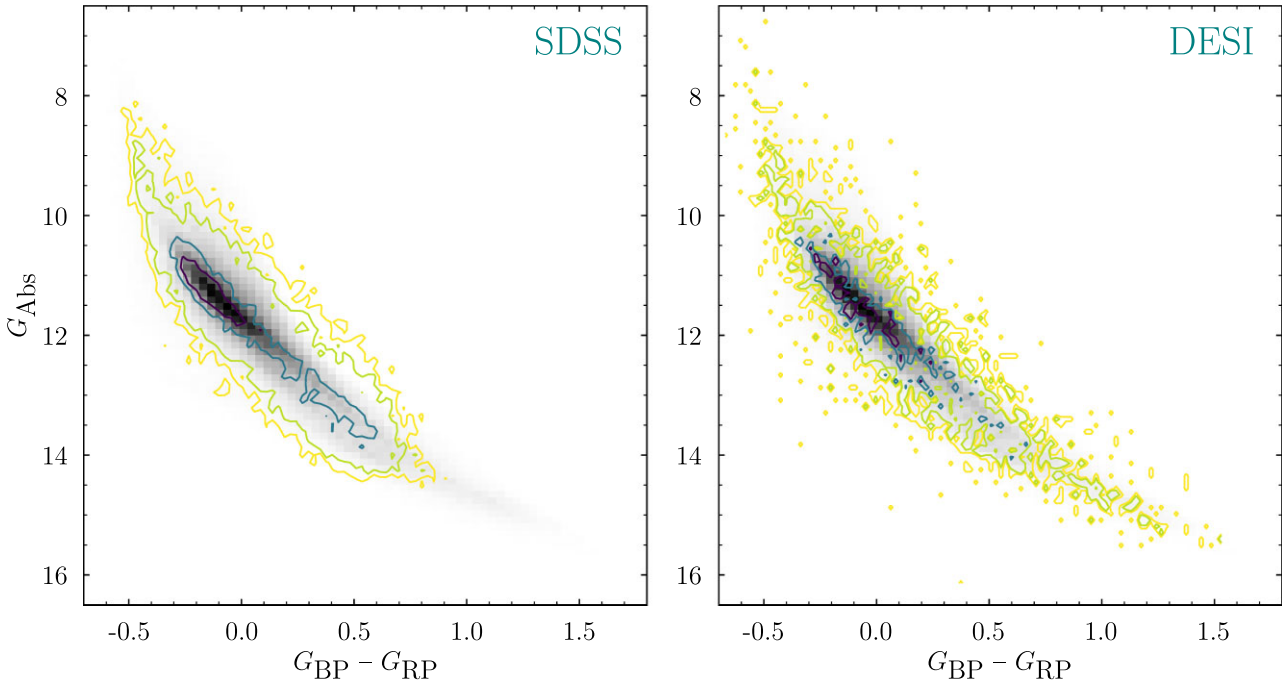

Figure 9. The distributions of the spectroscopically confirmed sample of *Gaia*–SDSS white dwarfs of GF21 (left) and the sample of DESI EDR white dwarfs (right) are shown as normalized contours in the *Gaia* HRD, where the yellow, lime, teal, and purple lines correspond to values of 0.05, 0.10, 0.35, and 0.55, respectively (from largest to smallest). Spectroscopically identified binaries have been excluded from both data sets. The magnitude-limited ($G < 20$) sample of high-confidence ($P_{\rm WD} > 0.95$) white dwarf candidates *Gaia* EDR3 from GF21 is underlied as a 2D grey-scale histogram. While the DESI EDR sample closely follows the magnitude-limited distribution of high-probability white dwarf candidates, the SDSS sample reveals significant selection effects (see the text). The higher granularity of the DESI EDR contours is due to the much smaller number of stars compared with the *Gaia*–SDSS sample.

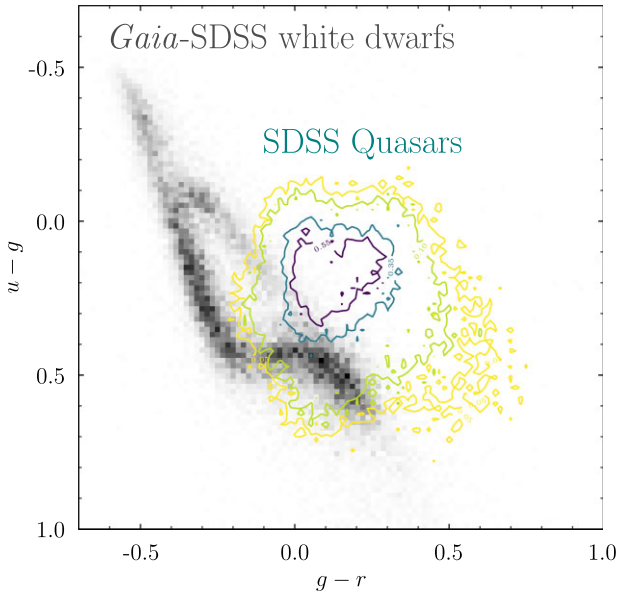

Figure 10. A histogram (black) of the *Gaia*–SDSS spectroscopically confirmed white dwarf sample of GF21, with a sample of SDSS-observed quasars plotted as contours (Schneider et al. 2007). The maximum of the quasar distribution is set to one, and the yellow, lime, teal, and purple contours correspond to values of 0.05, 0.10, 0.35, and 0.55, respectively (from largest to smallest). The overdensity of white dwarfs observed by SDSS on the *Gaia* HRD seen in Fig. 9 is likely due to serendipitous observations from SDSS quasar target selection (Richards et al. 2002).

in particular in nearby white dwarfs with strong metal absorption features. However, narrow absorption lines in hotter white dwarfs, in particular of Ca H/K and Na D, could also be present due to absorption in the interstellar medium (ISM) as these intrinsically bright stars can be observed at greater distances. To disentangle enrichment of the white dwarf photosphere and absorption in the ISM requires detailed modelling of the DESI spectra that takes into account the ionization and excitation within the white dwarf atmosphere, as well as the line-of-sight velocities of both the white dwarf and the ISM, and is beyond the scope of this work. We briefly discuss two noteworthy metal-enriched white dwarfs among the DESI EDR sample.

5.3.1 *WD J085035.17+320804.29*

WD J085035.17 + 320804.29 (hereafter WD J0850+3208, Fig. 15) is a DZAB[4] which shows extremely strong metal lines. O I absorption at 7775 and 8446 Å, along with the strong Hα line indicated significant amounts of H in what is likely an He-dominated atmosphere suggest that this white dwarf may have accreted a water-rich body (Klein et al. 2010; Farihi, Gänsicke & Koester 2013; Gentile Fusillo et al. 2017). Further bespoke modelling of WD J0850+3208 is required to determine the composition of the planetary body it accreted.

5.3.2 *WD J085912.92−005842.86*

WD J085912.92−005842.86 (hereafter WD J0859−0058, Fig. 15) is a known member of the 20-pc sample which has been previously

[4]WDJ0850+3208 is a known metal-enriched white dwarf, classified as a DABZ by Kong et al. (2019).

Downloaded from https://academic.oup.com/mnras/article/535/1/254/7774399 by guest on 09 December 2024

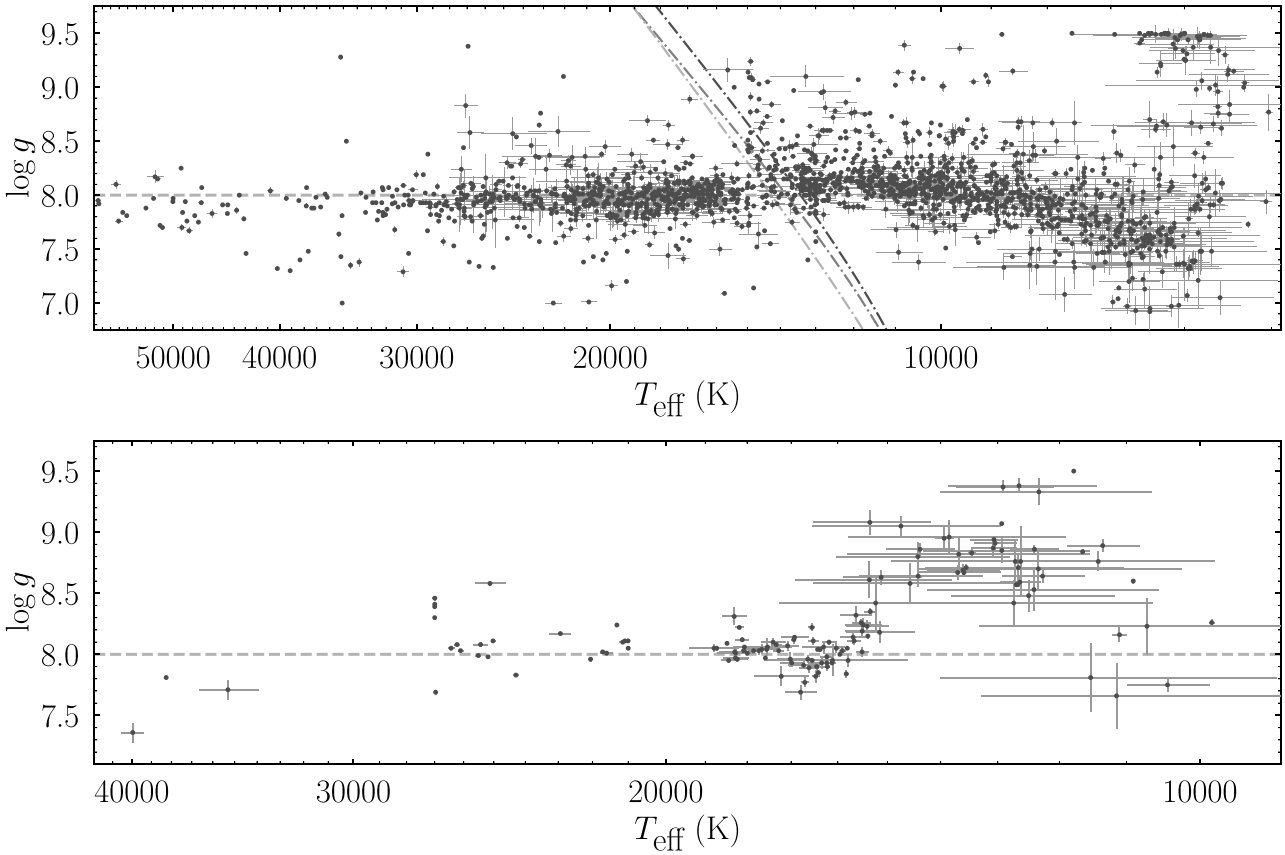

Figure 11. Effective temperatures against surface gravities of DA (top) and DB (bottom) white dwarfs measured from the DESI EDR spectra. The horizontal dashed lines indicate $\log g = 8$, the average surface gravity of white dwarfs. For the DA white dwarfs, we applied the 3D corrections of Tremblay et al. (2013). The parameters for the DB sample are presented here without 3D corrections, but 3D corrected values are given in the online catalogue (see Appendix B). The diagonal dotted–dashed lines show the maximum EWs of the Hβ, Hγ, and Hδ lines, going from dark grey (right) to light grey (left), in effective temperature as a function of surface gravity for the models we use in our fitting procedure.

reported as a featureless DC (Subasavage et al. 2008; Hollands et al. 2018b), however, the DESI spectrum clearly reveals Ca H/K lines. Inspection of spectrum of WD J0859−0058 obtained by Subasavage et al. (2008) and available in the MWDD shows no signs of metal absorption features, likely because of the much lower spectral resolution compared to the one obtained by DESI. This system is among the closest sources to the Sun observed by DESI, and this classification shows that new and interesting systems are still being identified in well-studied samples.

5.4 Magnetic white dwarfs

For the 56 systems presenting clear Zeeman-split spectral features we estimated their surface-averaged field strengths which are provided in Table E1. 39 (70 per cent) of the magnetic white dwarfs identified in the DESI EDR sample are new magnetic identifications from DESI. All but one, a DQH white dwarf, appear to show Zeeman splitting of the Balmer lines evident in the spectrum (Fig. 16). For these systems, we used the transition wavelengths of the Balmer series as a function of field strength B provided by Schimeczek & Wunner (2014a, b) and fit the Zeeman-split Hβ and Hα profiles, as these are usually the strongest features present. The fitting was performed by splitting the magnetic features into resolvable components and determining their location in wavelength-space, and then performing a least-squared fit with the theoretical wavelengths of the Balmer transitions to find a magnetic field strength. Two magnetic white dwarfs show Zeeman-split features in emission, classified as DAHe white dwarfs (Manser et al. 2023), and were fit by the authors using the same method.

While we assume in our fitting a single field strength, the field geometry of white dwarfs are known to be more complicated, having dipolar, quadrupole or even higher order poles and non-trivial combinations (Martin & Wickramasinghe 1984; Achilleos & Wickramasinghe 1989; Achilleos et al. 1992; Euchner et al. 2002, 2005, 2006). This is clearly evident in the spectra of high-field white dwarfs above ~ 200 MG, where only transitions that are close to $\mathrm{d}\lambda/\mathrm{d}B \simeq 0$ are identifiable, where λ is the wavelength of the transition, with others being smeared out across the spectrum (see fig. 2 of Schmidt et al. 2003).

Below we briefly discuss three systems of further interest:

5.4.1 WD J112513.32+094029.68

WD J1125+0940 is a DQH white dwarf that shows Zeeman splitting clearly identified in the $\simeq 7100$ and $\simeq 9100$ Å C lines. We fit these Zeeman-split features and obtain a field strength of 2.19 MG (Fig. 17).

5.4.2 WD J113357.66+515204.69

WD J113357.66 + 515204.69 (hereafter WD J1133+5152) shows five components in Hα. Individual exposures obtained by DESI for WD J1133+5152 only show three components, as expected for

Downloaded from https://academic.oup.com/mnras/article/535/1/254/7774399 by guest on 09 December 2024

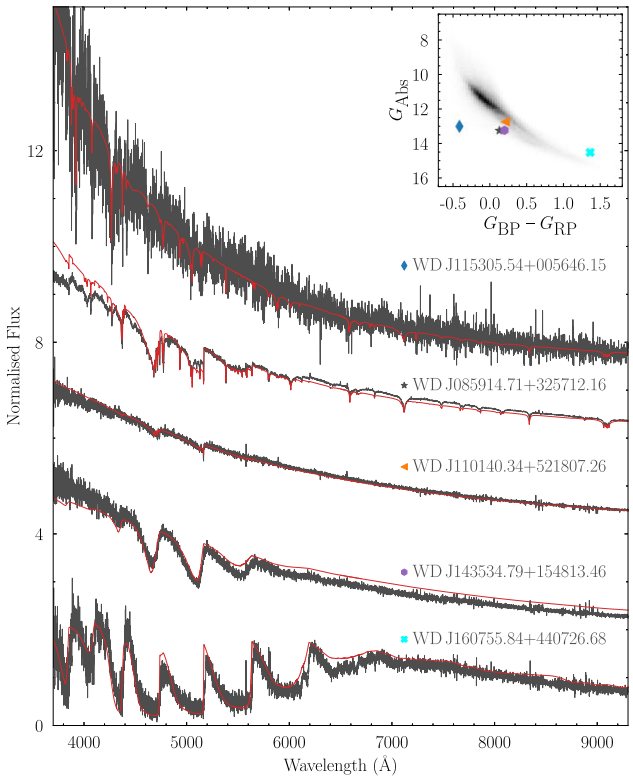

Figure 12. Examples of different types of DQs (grey) with model fits (red) overplotted. Spectra are vertically offset for clarity. The inset in the top right shows the location of these systems on the *Gaia* HRD as coloured markers.

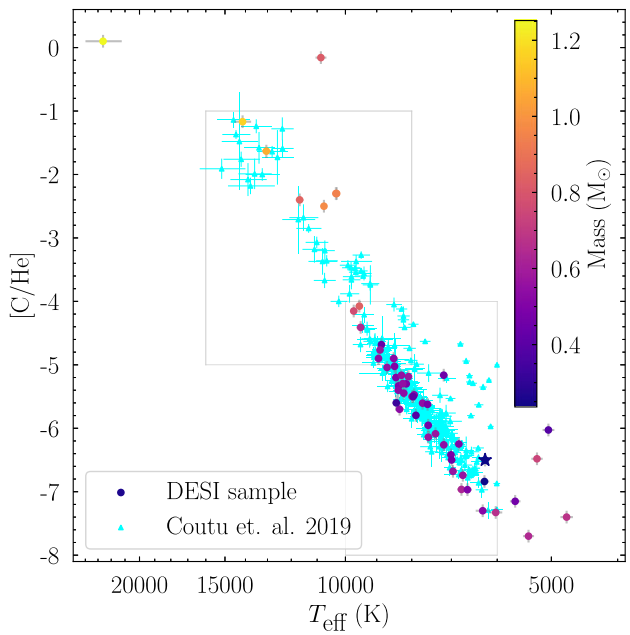

Figure 13. Fitted parameters of carbon-rich white dwarfs (DQs) in our sample (purple, orange, and yellow circles) compared to the sample of 317 DQs studied by Coutu et al. (2019, cyan triangles). Grey boxes denote the parameter space of the model grids used in Coutu et al. (2019), and are presented here to highlight the regions where comparisons between the samples should be made. The DA+DQ binary WD J0920+6926 is included (star), although the fit assumes the spectrum is of a single object.

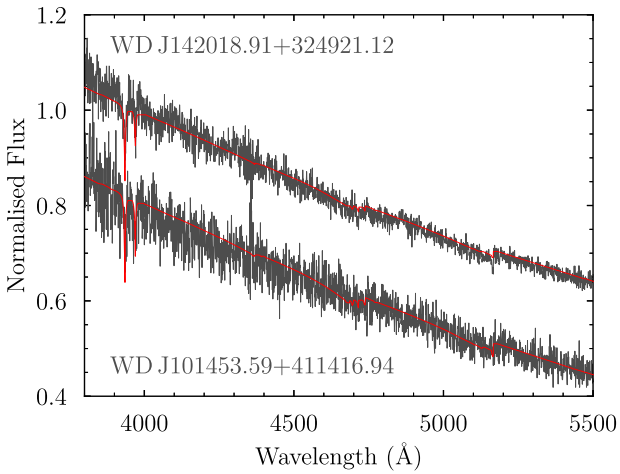

Figure 14. DESI spectra (grey) of the DZQ WD J1014+4114 and the DQZ WD J1420+3249 with model fits including metals overplotted (red).

Zeeman splitting, and the profiles shift from one field strength to another and back again over a time frame of $\simeq 20$ min. This sharp transition between field strengths in the observed spectrum is similar to that observed at G183−35 (Kilic et al. 2019), and it has been suggested that a combination of a complex magnetic field structure in addition to an inhomogeneous chemical distribution across the white dwarf surface can explain the profiles. We estimate the two identified field strengths observed for WD J1133+5152 from the five components assuming they are a superposition of two sets of Zeeman-split profiles as 3.04 ± 0.07 and 4.4 ± 0.1 MG, and these are both reported in Table E1.

WD J1133+5152 was previously identified as a DAH from SDSS spectroscopy (Schmidt et al. 2003; Külebi et al. 2009), however there is no documentation of five Zeeman components. It has been modelled to have a polar field strength of $\simeq 8$ MG, slightly varying depending on the complexity of the dipolar model used, and a viewing angle compared to the dipolar field configuration as looking along the equator. For a centred-dipolar field configuration, the field strength near the magnetic equator is a factor two lower than the field strength at the poles (Achilleos et al. 1992), and our measured field strengths for WD J1133+5152 are in rough agreement with a factor two drop compared with the previously reported polar field strength.

5.4.3 *WD J070253.76+553733.64*

WD J070253.76 + 553733.64 (hereafter WD J0702+5537) also shows five components in Hα, similar to WD J1133+5152. By fitting the five components assuming they come from two sets of Zeeman-split profiles, we obtain field strengths of 6.89 ± 0.07 and 15.5 ± 0.2 MG.

5.5 Cataclysmic variables

Table F1 lists the 12 CVs identified by DESI, five of which are new discoveries, and seven are previously known systems. DESI spectra along with ZTF light curves are shown in Fig. 18 for the five new systems, and we briefly discuss them below.

5.5.1 *J124413.48+593610.24*

The DESI spectrum reveals a blue continuum superimposed with moderately strong Hα emission, and weaker Hβ emission. The

Downloaded from https://academic.oup.com/mnras/article/535/1/254/7774399 by guest on 09 December 2024

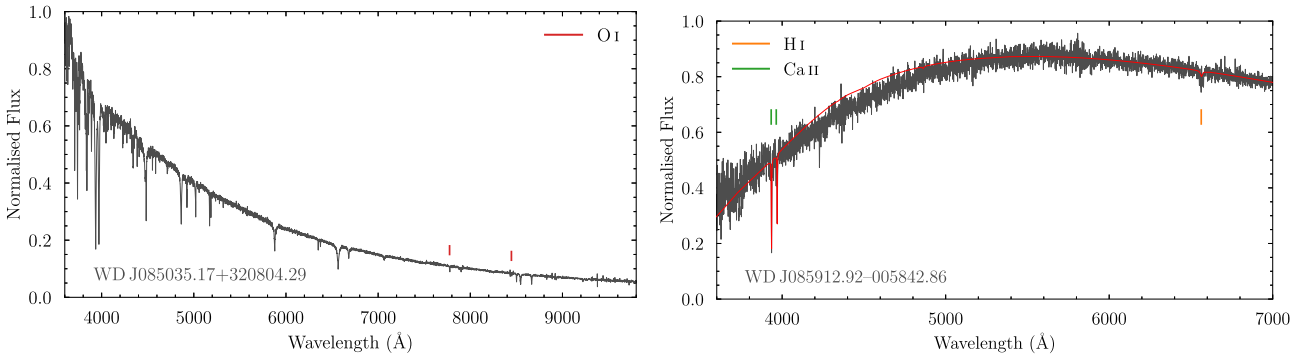

Figure 15. Two examples of white dwarfs within the DESI EDR sample that accrete planetary debris. Left: the spectrum of the extremely metal-enriched DZAB white dwarf WD J0850+3208 exhibits absorption lines of many elements, including oxygen (indicated by the red tick marks), which along with the detection of Balmer lines may be indicative of water accretion. Right: the DESI spectrum (grey) of the DZA WD J0859−0058 contains calcium and hydrogen absorption features indicated by vertical tick marks. The best-fitting model (red) implies $T_{\rm eff} = 4832 \pm 10$ K, $\log g = 7.87 \pm 0.10$, and $\log({\rm Ca/H}) = -10.25 \pm 0.10$. WD J0859−0058 is a known 20 pc member with a previous DC spectral classification based on lower quality spectroscopy (Subasavage et al. 2008).

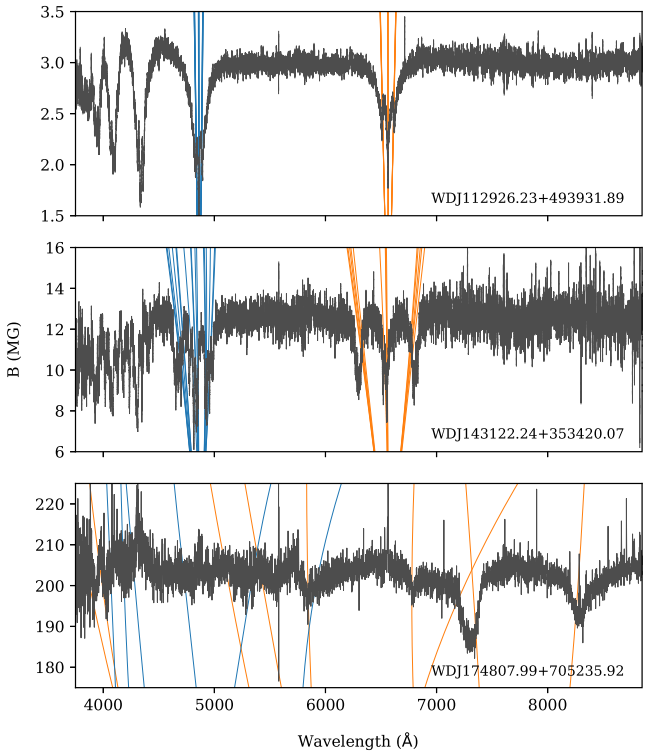

Figure 16. Continuum-normalized spectra of three DAH white dwarfs showcasing the range of magnetic fields observed. Each spectrum has been normalized to one, and then multiplied by the field strength, B, determined from the spectrum. Transition wavelengths for Hβ and Hα as a function of B are provided by Schimeczek & Wunner (2014a, b) and are presented as blue and orange lines. respectively. Top panel: the field strengths on a few MG level show three clear components consistent with the linear Zeeman-splitting regime. Middle panel: as B increases, the energy degeneracy due to orbital angular momentum, l, will lift and these three components will split further, resulting in 18 (15) transitions in Hβ (Hα). Bottom panel: when the field reaches a few hundred MG, the transitions spread across the optical spectral range.

deep central absorption feature within Hα is suggestive of a high inclination (Horne & Marsh 1986). The slope of the spectrum displays a break around 7000 Å, which may indicate the contribution of the donor star; however, the signal-to-noise ratio is too low to identify any of its spectral signatures. The ZTF light curves of this

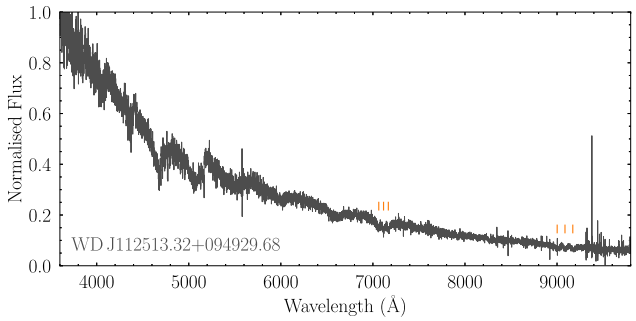

Figure 17. The DQH WD J1125+0949. Orange vertical tabs highlight clear Zeeman-split components, which we used to determine the surface averaged field strength of $B = 2.19$ MG.

system reveal multiple outbursts, several of which lasting $\simeq 10$ d, corroborating a classification as SU UMa dwarf nova (Brun & Petit 1952; Vogt 1980). The ZTF data also reveal deep eclipses, and we measure an orbital period of $P = 1.74953778(98)$ h.

5.5.2 J142833.44+003100.45

The DESI spectrum shows a blue slope with broad Balmer absorption lines from the white dwarf, which are partially filled in by double-peaked emission lines indicating the presence of an accretion disc. The spectrum reveals no signature from the donor star. The ZTF light curves do not exhibit any outbursts, and a period analysis fails to detect a coherent signal in the data. This CV is most likely a WZ Sge dwarf nova with a long outburst recurrence time (Bailey 1979).

5.5.3 J143435.39+334049.98

The DESI and ZTF data of this CV are overall similar to J142833.44+003100.45, though with weaker Balmer absorption lines from the white dwarf, and stronger Balmer emission lines, suggestive of a larger contribution of the accretion disc. It is also most likely a WZ Sge dwarf nova.

5.5.4 J161927.83+423039.61

The DESI spectrum shows a blue continuum with the Balmer jump in emission, and double-peaked emission lines from an accretion

Downloaded from https://academic.oup.com/mnras/article/535/1/254/7774399 by guest on 09 December 2024

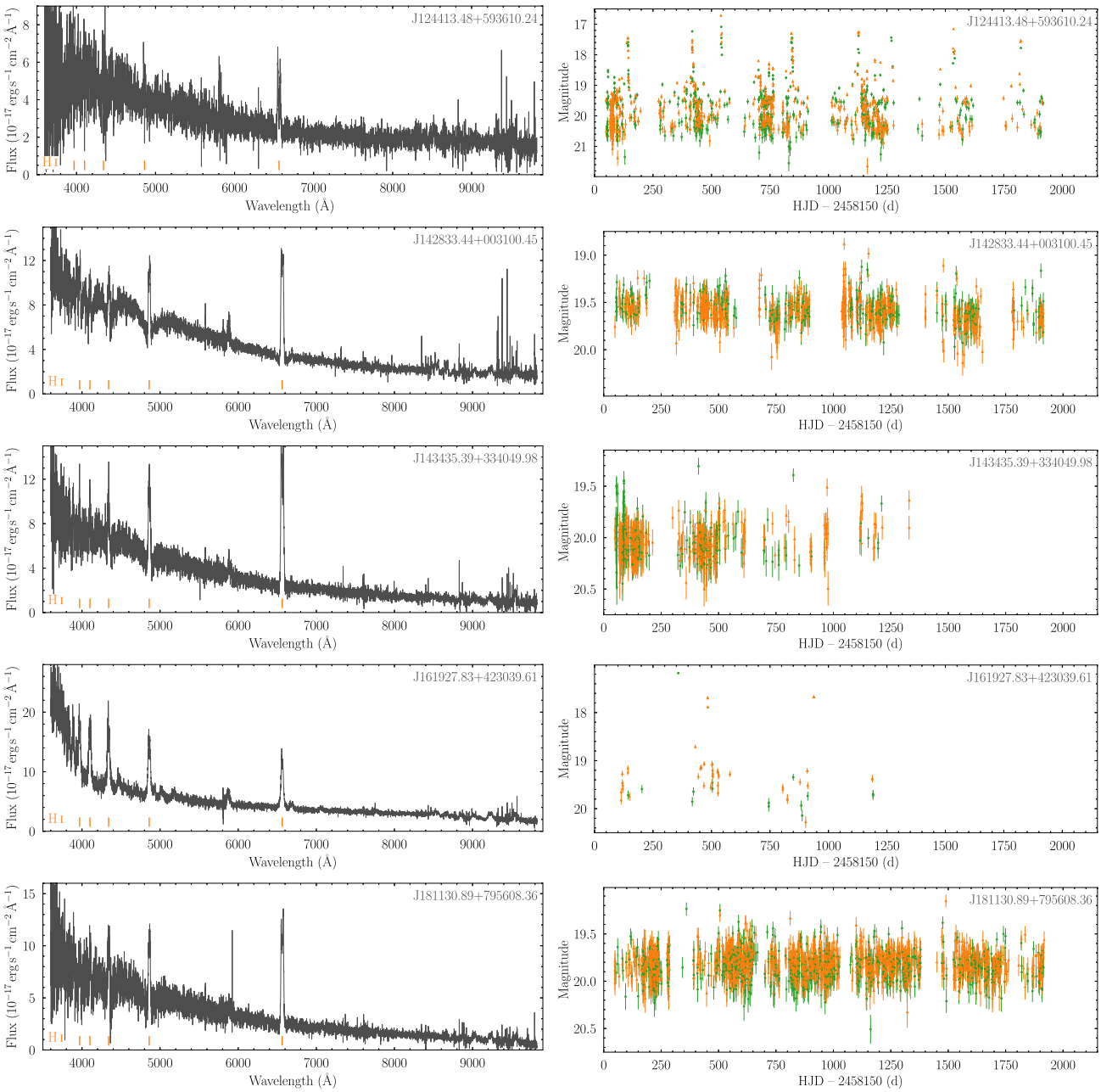

Figure 18. DESI spectra (left panels) and ZTF light curves (right panels) of five new CVs identified in the DESI EDR. The rest wavelength of the first five Balmer lines are denoted by vertical orange tabs for the spectra. *g*-band and *r*-band data points are denoted by green circles and orange triangles, respectively.

disc, with no signature of either the white dwarf or the donor star. The spectral appearance is typical of an SU UMa dwarf nova. The ZTF light curve is sparse, but captured one outburst, confirming the SU UMa classification.

5.5.5 *J181130.89+795608.36*

The DESI and ZTF data of this system closely resemble those of J142833.44+003100.45 and J143435.39+334049.98, and this CV is also most likely a WZ Sge dwarf nova.

These CVs have been serendipitously included in the selection cuts made by Gentile Fusillo et al. (2019) and later by Cooper et al. (2023) to target isolated white dwarfs. CVs in this area of the *Gaia* HRD are dominated by WZ Sge and SU UMa subtypes [compare our Fig. 7 (top left) and fig. 15 of Inight et al. 2023], consistent with our identifications.

6 CONCLUSIONS

We present here the DESI EDR sample of 2706 white dwarfs and 66 binaries including white dwarfs selected from cuts made on *Gaia* astrometry and photometry. The resulting *Gaia* selection function is relatively simple, making the DESI sample significantly more unbiased than previous surveys such as the SDSS and facilitating its use in statistical studies of white dwarf samples. Many of the white dwarfs in the DESI EDR have new spectroscopic classifications, including 43 DQs, 121 metal-line DxZ white dwarfs, 39 magnetic

Downloaded from https://academic.oup.com/mnras/article/535/1/254/7774399 by guest on 09 December 2024

white dwarfs, and five CVs. The forthcoming DESI DR1 sample contains over 47 000 white dwarf candidates, and will revolutionize statistical studies of white dwarf samples.

ACKNOWLEDGEMENTS

We thank the anonymous referee for their review of the manuscript which improved the quality of the manuscript. We thank Pier-Emmanuel Tremblay for useful discussions that improved the quality of the manuscript. The authors acknowledge financial support from Imperial College London through an Imperial College Research Fellowship grant awarded to CJM. This project has received funding from the European Research Council (ERC) under the European Union's Horizon 2020 research and innovation programme (grant agreement no. 101020057). PI was supported by a Leverhulme Trust Research Project Grant. SX was supported by NOIRLab, which is managed by the Association of Universities for Research in Astronomy (AURA) under a cooperative agreement with the National Science Foundation. SK acknowledges support from the Science & Technology Facilities Council (STFC) grant ST/Y001001/1. For the purpose of open access, the author has applied a Creative Commons Attribution (CC BY) licence to any Author Accepted Manuscript version arising from this submission. In identifying new white dwarfs and classifications, we have made use of the MWDD (Dufour et al. 2017) and the SIMBAD database, operated at CDS, Strasbourg, France (Wenger et al. 2000). This research is supported by the Director, Office of Science, Office of High Energy Physics of the U.S. Department of Energy under contract no. DE–AC02–05CH11231, and by the National Energy Research Scientific Computing Center, a DOE Office of Science User Facility under the same contract; additional support for DESI is provided by the U.S. National Science Foundation, Division of Astronomical Sciences under contract no. AST-0950945 to the NSF's National Optical-Infrared Astronomy Research Laboratory; the Science and Technologies Facilities Council of the United Kingdom; the Gordon and Betty Moore Foundation; the Heising-Simons Foundation; the French Alternative Energies and Atomic Energy Commission (CEA); the National Council of Science and Technology of Mexico (CONACYT); the Ministry of Science and Innovation of Spain (MICINN), and by the DESI Member Institutions: https://www.desi.lbl.gov/collaborating-institutions. The authors are honoured to be permitted to conduct scientific research on Iolkam Du'ag (Kitt Peak), a mountain with particular significance to the Tohono O'odham Nation. This work has made use of data from the European Space Agency (ESA) mission *Gaia* (https://www.cosmos.esa.int/gaia), processed by the *Gaia* Data Processing and Analysis Consortium (DPAC, https://www.cosmos.esa.int/web/gaia/dpac/consortium). Funding for the DPAC has been provided by national institutions, in particular the institutions participating in the *Gaia* Multilateral Agreement. Funding for the SDSS-IV has been provided by the Alfred P. Sloan Foundation, the U.S. Department of Energy Office of Science, and the Participating Institutions. SDSS-IV acknowledges support and resources from the Center for High Performance Computing at the University of Utah. The SDSS website is www.sdss4.org. SDSS-IV is managed by the Astrophysical Research Consortium for the Participating Institutions of the SDSS Collaboration including the Brazilian Participation Group, the Carnegie Institution for Science, Carnegie Mellon University, Center for Astrophysics| Harvard and Smithsonian, the Chilean Participation Group, the French Participation Group, Instituto de Astrofísica de Canarias, The Johns Hopkins University, Kavli Institute for the Physics and Mathematics of the Universe (IPMU)/University of Tokyo, the Korean Participation Group, Lawrence Berkeley National Laboratory, Leibniz Institut für Astrophysik Potsdam (AIP), Max-Planck-Institut für Astronomie (MPIA Heidelberg), Max-Planck-Institut für Astrophysik (MPA Garching), Max-Planck-Institut für Extraterrestrische Physik (MPE), National Astronomical Observatories of China, New Mexico State University, New York University, University of Notre Dame, Observatário Nacional/MCTI, The Ohio State University, Pennsylvania State University, Shanghai Astronomical Observatory, United Kingdom Participation Group, Universidad Nacional Autónoma de México, University of Arizona, University of Colorado Boulder, University of Oxford, University of Portsmouth, University of Utah, University of Virginia, University of Washington, University of Wisconsin, Vanderbilt University, and Yale University. Based on observations obtained with the Samuel Oschin Telescope 48-inch and the 60-inch Telescope at the Palomar Observatory as part of the Zwicky Transient Facility project. ZTF is supported by the National Science Foundation under grants nos AST-1440341 and AST-2034437 and a collaboration including current partners Caltech, IPAC, the Weizmann Institute for Science, the Oskar Klein Center at Stockholm University, the University of Maryland, Deutsches Elektronen-Synchrotron and Humboldt University, the TANGO Consortium of Taiwan, the University of Wisconsin at Milwaukee, Trinity College Dublin, Lawrence Livermore National Laboratories, IN2P3, University of Warwick, Ruhr University Bochum, Northwestern University, and former partners the University of Washington, Los Alamos National Laboratories, and Lawrence Berkeley National Laboratories. Operations are conducted by COO, IPAC, and UW. This research has used data, tools or materials developed as part of the EXPLORE project that has received funding from the European Union's Horizon 2020 research and innovation programme under grant agreement no. 101004214.

DATA AVAILABILITY

The data presented here are all available from the public archives of DESI, *Gaia*, ZTF, SDSS, and Pan-STARRS. Data and PYTHON scripts used to produce the figures presented in this paper, along with the FITS file containing the DESI EDR white dwarf catalogue, are available at https://zenodo.org/records/13684288.

REFERENCES

Abdurro'uf et al., 2022, ApJS, 259, 35
Achilleos N., Wickramasinghe D. T., 1989, ApJ, 346, 444
Achilleos N., Wickramasinghe D. T., Liebert J., Saffer R. A., Grauer A. D., 1992, ApJ, 396, 273
Allende Prieto C. et al., 2020, Res. Notes Am. Astron. Soc., 4, 188
Almeida A. et al., 2023, ApJS, 267, 44
Althaus L. G., Serenelli A. M., Panei J. A., Córsico A. H., García-Berro E., Scóccola C. G., 2005, A&A, 435, 631
Althaus L. G., Miller Bertolami M. M., Córsico A. H., 2013, A&A, 557, A19
Angel J. R. P., Hintzen P., Strittmatter P. A., Martin P. G., 1974a, ApJ, 190, L71
Angel J. R. P., Carswell R. F., Strittmatter P. A., Beaver E. A., Harms R., 1974b, ApJ, 194, L47
Bailer-Jones C. A. L., Rybizki J., Fouesneau M., Demleitner M., Andrae R., 2021, AJ, 161, 147
Bailey J., 1979, MNRAS, 189, 41P
Barstow M. A., Barstow J. K., Casewell S. L., Holberg J. B., Hubeny I., 2014, MNRAS, 440, 1607
Bauer E. B., Bildsten L., 2018, ApJ, 859, L19
Bédard A., Bergeron P., Brassard P., Fontaine G., 2020, ApJ, 901, 93
Bédard A., Bergeron P., Brassard P., 2022, ApJ, 930, 8
Bellm E. C. et al., 2019, PASP, 131, 018002

Downloaded from https://academic.oup.com/mnras/article/535/1/254/7774399 by guest on 09 December 2024

Berg C., Wegner G., Foltz C. B., Chaffee F. H. J., Hewett P. C., 1992, ApJS, 78, 409
Bergeron P., 2001, ApJ, 558, 369
Bergeron P., Wesemael F., Fontaine G., Liebert J., 1990, ApJ, 351, L21
Bergeron P., Ruiz M. T., Leggett S. K., 1997, ApJS, 108, 339
Bergeron P., Leggett S. K., Ruiz M., 2001, ApJS, 133, 413
Bergeron P. et al., 2011, ApJ, 737, 28
Bergeron P., Kilic M., Blouin S., Bédard A., Leggett S. K., Brown W. R., 2022, ApJ, 934, 36
Blouin S., 2022, A&A, 666, L7
Blouin S., Kowalski P. M., Dufour P., 2017, ApJ, 848, 36
Blouin S., Dufour P., Allard N. F., 2018, ApJ, 863, 184
Blouin S., Bédard A., Tremblay P.-E., 2023a, MNRAS, 523, 3363
Blouin S., Kilic M., Bédard A., Tremblay P.-E., 2023b, MNRAS, 525, L112
Borysow A., Jorgensen U. G., Fu Y., 2001, J. Quant. Spec. Radiat. Transf., 68, 235
Brun A., Petit M., 1952, Bull. Assoc. Fr. Obs. Etoiles Variables, 12, 1
Camisassa M., Torres S., Hollands M., Koester D., Raddi R., Althaus L. G., Rebassa-Mansergas A., 2023, A&A, 674, A213
Caron A., Bergeron P., Blouin S., Leggett S. K., 2023, MNRAS, 519, 4529
Cauley P. W., Farihi J., Redfield S., Bachman S., Parsons S. G., Gänsicke B. T., 2018, ApJ, 852, L22
Chambers K. C. et al., 2019, preprint (arXiv:1612.05560)
Cheng S., Cummings J. D., Ménard B., 2019, ApJ, 886, 100
Christlieb N., Wisotzki L., Reimers D., Homeier D., Koester D., Heber U., 2001, A&A, 366, 898
Cooper A. P. et al., 2023, ApJ, 947, 37
Coutu S., Dufour P., Bergeron P., Blouin S., Loranger E., Allard N. F., Dunlap B. H., 2019, ApJ, 885, 74
Croom S. M., Smith R. J., Boyle B. J., Shanks T., Miller L., Outram P. J., Loaring N. S., 2004, MNRAS, 349, 1397
Cukanovaite E., Tremblay P. E., Freytag B., Ludwig H. G., Bergeron P., 2018, MNRAS, 481, 1522
Cukanovaite E., Tremblay P.-E., Bergeron P., Freytag B., Ludwig H.-G., Steffen M., 2021, MNRAS, 501, 5274
Cunningham T., Tremblay P.-E., Freytag B., Ludwig H.-G., Koester D., 2019, MNRAS, 488, 2503
Cunningham T., Tremblay P.-E., Gentile Fusillo N. P., Hollands M., Cukanovaite E., 2020, MNRAS, 492, 3540
Cunningham T., Wheatley P. J., Tremblay P.-E., Gänsicke B. T., King G. W., Toloza O., Veras D., 2022, Nature, 602, 219
Dalton G. et al., 2012, in McLean I. S., Ramsay S. K., Takami H., eds, Proc. SPIE Conf. Ser. Vol. 8446, Ground-Based and Airborne Instrumentation for Astronomy IV. SPIE, Bellingham, p. 84460P
Dalton G. et al., 2016, in Evans C. J., Simard L., Takami H., eds, Proc. SPIE Conf. Ser. Vol. 7015, Ground-Based and Airborne Instrumentation for Astronomy VI. SPIE, Bellingham, p. 99081G
Dawson K. S. et al., 2013, AJ, 145, 10
Dawson K. S. et al., 2016, AJ, 151, 44
de Jong R. S. et al., 2016, in Evans C. J., Simard L., Takami H., eds, Proc. SPIE Conf. Ser. Vol. 9908, Ground-based and Airborne Instrumentation for Astronomy VI. SPIE, Bellingham, p. 99081O
Debes J. H., Sigurdsson S., 2002, ApJ, 572, 556
DESI Collaboration, 2016a, preprint (arXiv:1611.00036)
DESI Collaboration, 2016b, preprint (arXiv:1611.00037)
DESI Collaboration, 2022, AJ, 164, 207
DESI Collaboration, 2024a, AJ, 167, 62
DESI Collaboration, 2024b, AJ, 168, 58
Dobbie P. D. et al., 2006, MNRAS, 369, 383
Dufour P., Liebert J., Fontaine G., Behara N., 2007a, Nat, 450, 522
Dufour P. et al., 2007b, ApJ, 663, 1291
Dufour P., Blouin S., Coutu S., Fortin-Archambault M., Thibeault C., Bergeron P., Fontaine G., 2017, in Tremblay P. E., Gaensicke B., Marsh T., eds, ASP Conf. Ser. Vol. 509, 20th European White Dwarf Workshop. Astron. Soc. Pac., San Francisco, p. 3
Dunlap B. H., Clemens J. C., 2015, in Dufour P., Bergeron P., Fontaine G., eds, ASP Conf. Ser. Vol. 493, 19th European Workshop on White Dwarfs. Astron. Soc. Pac., San Francisco, p. 547
Eisenstein D. J. et al., 2006, ApJS, 167, 40
Elms A. K. et al., 2023, MNRAS, 524, 4996
Euchner F., Jordan S., Beuermann K., Gänsicke B. T., Hessman F. V., 2002, A&A, 390, 633
Euchner F., Reinsch K., Jordan S., Beuermann K., Gänsicke B. T., 2005, A&A, 442, 651
Euchner F., Jordan S., Beuermann K., Reinsch K., Gänsicke B. T., 2006, A&A, 451, 671
Farihi J., Gänsicke B. T., Koester D., 2013, MNRAS, 432, 1955
Fitzpatrick E. L., 1999, PASP, 111, 63
Fleming T. A., Liebert J., Green R. F., 1986, ApJ, 308, 176
Fontaine G., Wesemael F., 1987, in Philip A. G. D., Hayes D. S., Liebert J. W., eds, IAU Colloq. 95: Second Conference on Faint Blue Stars, L. Davis Press, Inc., Schenectady, NY, p. 319
Fontaine G., Brassard P., Bergeron P., 2001, PASP, 113, 409
Foreman-Mackey D., Hogg D. W., Lang D., Goodman J., 2013, PASP, 125, 306
Gaia Collaboration, 2018, A&A, 616, A10
Gaia Collaboration, 2021, A&A, 649, A1
Gänsicke B. T. et al., 2009, MNRAS, 397, 2170
Gänsicke B. T., Koester D., Farihi J., Girven J., Parsons S. G., Breedt E., 2012, MNRAS, 424, 333
García-Berro E. et al., 2012, ApJ, 749, 25
Genest-Beaulieu C., Bergeron P., 2014, ApJ, 796, 128
Genest-Beaulieu C., Bergeron P., 2019, ApJ, 871, 169
Gentile Fusillo N. P., Gänsicke B. T., Greiss S., 2015, MNRAS, 448, 2260
Gentile Fusillo N. P., Gänsicke B. T., Farihi J., Koester D., Schreiber M. R., Pala A. F., 2017, MNRAS, 468, 971
Gentile Fusillo N. P. et al., 2019, MNRAS, 482, 4570
Gentile Fusillo N. P. et al., 2021, MNRAS, 508, 3877
Gianninas A., Bergeron P., Ruiz M. T., 2011, ApJ, 743, 138
Giclas H. L., Burnham R., Thomas N. G., 1965, Lowell Obs. Bull., 125, 155
Graham J. R., Matthews K., Neugebauer G., Soifer B. T., 1990, ApJ, 357, 216
Green R. F., Schmidt M., Liebert J., 1986, ApJS, 61, 305
Gunn J. E. et al., 2006, AJ, 131, 2332
Guo J., Zhao J., Tziamtzis A., Liu J., Li L., Zhang Y., Hou Y., Wang Y., 2015, MNRAS, 454, 2787
Guy J. et al., 2023, AJ, 165, 144
Hahn C. et al., 2023, AJ, 165, 253
Hardy F., Dufour P., Jordan S., 2023a, MNRAS, 520, 6111
Hardy F., Dufour P., Jordan S., 2023b, MNRAS, 520, 6135
Harris H. C. et al., 2003, AJ, 126, 1023
Herwig F., Blöcker T., Langer N., Driebe T., 1999, A&A, 349, L5
Hodgkin S. T. et al., 2021, A&A, 652, A76
Hollands M. A., Koester D., Alekseev V., Herbert E. L., Gänsicke B. T., 2017, MNRAS, 467, 4970
Hollands M. A., Gänsicke B. T., Koester D., 2018a, MNRAS, 477, 93
Hollands M. A., Tremblay P. E., Gänsicke B. T., Gentile-Fusillo N. P., Toonen S., 2018b, MNRAS, 480, 3942
Hollands M. A. et al., 2020, Nat. Astron., 4, 663
Hollands M. A., Tremblay P.-E., Gänsicke B. T., Koester D., Gentile-Fusillo N. P., 2021, Nat. Astron., 5, 451
Hollands M. A., Tremblay P. E., Gänsicke B. T., Koester D., 2022, MNRAS, 511, 71
Homeier D., Koester D., Hagen H. J., Jordan S., Heber U., Engels D., Reimers D., Dreizler S., 1998, A&A, 338, 563
Horne K., Marsh T. R., 1986, MNRAS, 218, 761
Iben I. J., Ritossa C., Garcia-Berro E., 1997, ApJ, 489, 772
Inight K. et al., 2023, MNRAS, 525, 3597
Izquierdo P., Toloza O., Gänsicke B. T., Rodríguez-Gil P., Farihi J., Koester D., Guo J., Redfield S., 2021, MNRAS, 501, 4276
Izquierdo P., Gänsicke B. T., Rodríguez-Gil P., Koester D., Toloza O., Gentile Fusillo N. P., Pala A. F., Tremblay P.-E., 2023, MNRAS, 520, 2843
Jura M., 2003, ApJ, 584, L91
Kaiser B. C., Clemens J. C., Blouin S., Dufour P., Hegedus R. J., Reding J. S., Bédard A., 2021, Science, 371, 168
Kawka A., Ferrario L., Vennes S., 2023, MNRAS, 520, 6299

Downloaded from https://academic.oup.com/mnras/article/535/1/254/7774399 by guest on 09 December 2024

Keller P. M., Breedt E., Hodgkin S., Belokurov V., Wild J., García-Soriano I., Wise J. L., 2022, MNRAS, 509, 4171
Kemp J. C., Swedlund J. B., Landstreet J. D., Angel J. R. P., 1970, ApJ, 161, L77
Kenyon S. J., Shipman H. L., Sion E. M., Aannestad P. A., 1988, ApJ, 328, L65
Kepler S. O. et al., 2013, MNRAS, 429, 2934
Kepler S. O. et al., 2015, MNRAS, 446, 4078
Kepler S. O. et al., 2016, MNRAS, 455, 3413
Kepler S. O., Koester D., Pelisoli I., Romero A. D., Ourique G., 2021, MNRAS, 507, 4646
Kilic M., Kowalski P. M., Reach W. T., von Hippel T., 2009, ApJ, 696, 2094
Kilic M., Rolland B., Bergeron P., Vanderbosch Z., Benni P., Garlitz J., 2019, MNRAS, 489, 3648
Kilic M., Bergeron P., Kosakowski A., Brown W. R., Agüeros M. A., Blouin S., 2020, ApJ, 898, 84
Kilic M., Bergeron P., Blouin S., Jewett G., Brown W. R., Moss A., 2024, ApJ, 965, 11
Klein B., Jura M., Koester D., Zuckerman B., Melis C., 2010, ApJ, 709, 950
Klein B. L., Doyle A. E., Zuckerman B., Dufour P., Blouin S., Melis C., Weinberger A. J., Young E. D., 2021, ApJ, 914, 61
Kleinman S. J. et al., 2004, ApJ, 607, 426
Kleinman S. J. et al., 2013, ApJS, 204, 5
Koester D., 1976, A&A, 52, 415
Koester D., 2010, Mem. Soc. Astron. Ital., 81, 921
Koester D., Kepler S. O., 2015, A&A, 583, A86
Koester D., Kepler S. O., 2019, A&A, 628, A102
Koester D., Knist S., 2006, A&A, 454, 951
Koester D., Girven J., Gänsicke B. T., Dufour P., 2011, A&A, 530, A114
Koester D., Gänsicke B. T., Farihi J., 2014, A&A, 566, A34
Koester D., Kepler S. O., Irwin A. W., 2020, A&A, 635, A103
Kollmeier J. A. et al., 2017, preprint (arXiv:1711.03234)
Kong X., Luo A. L., Li X.-R., 2019, Res. Astron. Astrophys., 19, 088
Kowalski P. M., Saumon D., 2006, ApJ, 651, L137
Kraft R. P., 1962, ApJ, 135, 408
Külebi B., Jordan S., Euchner F., Gänsicke B. T., Hirsch H., 2009, A&A, 506, 1341
Lallement R., Vergely J. L., Babusiaux C., Cox N. L., 2022, A&A, 661, A147
Liebert J., 1977, PASP, 89, 78
Liebert J., 1986, in Hunger K., Schoenberner D., Kameswara Rao N., eds, IAU Colloq. 87: Hydrogen Deficient Stars and Related Objects. Steward Observatory, University of Arizona, Tucson, AZ, p. 367
Liebert J., Bergeron P., Holberg J. B., 2003, AJ, 125, 348
Lindegren L. et al., 2021, A&A, 649, A2
Manser C. J. et al., 2016, MNRAS, 455, 4467
Manser C. J. et al., 2021, MNRAS, 508, 5657
Manser C. J. et al., 2023, MNRAS, 521, 4976
Marsh T. R., Horne K., 1988, MNRAS, 235, 269
Martin B., Wickramasinghe D. T., 1984, MNRAS, 206, 407
Masci F. J. et al., 2019, PASP, 131, 018003
Myers A. D. et al., 2023, AJ, 165, 50
Nelson B., Ford E. B., Payne M. J., 2013, ApJS, 210, 11
Nordhaus J., Wellons S., Spiegel D. S., Metzger B. D., Blackman E. G., 2011, Proc. Natl. Acad. Sci., 108, 3135
O'Brien M. W. et al., 2023, MNRAS, 518, 3055
O'Brien M. W. et al., 2024, MNRAS, 527, 8687
Okuya A., Ida S., Hyodo R., Okuzumi S., 2023, MNRAS, 519, 1657
Pelletier C., Fontaine G., Wesemael F., Michaud G., Wegner G., 1986, ApJ, 307, 242
Ramírez-Pérez C. et al., 2024, MNRAS, 528, 6666
Rebassa-Mansergas A., Gänsicke B. T., Rodríguez-Gil P., Schreiber M. R., Koester D., 2007, MNRAS, 382, 1377
Rebassa-Mansergas A., Solano E., Xu S., Rodrigo C., Jiménez-Esteban F. M., Torres S., 2019, MNRAS, 489, 3990
Reding J. S., Hermes J. J., Clemens J. C., Hegedus R. J., Kaiser B. C., 2023, MNRAS, 522, 693
Regős E., Tout C. A., 1995, MNRAS, 273, 146
Reid I. N., Liebert J., Schmidt G. D., 2001, ApJ, 550, L61
Richards G. T. et al., 2002, AJ, 123, 2945
Riello M. et al., 2021, A&A, 649, A3
Rogers L. K. et al., 2024, MNRAS, 527, 6038
Rolland B., Bergeron P., Fontaine G., 2018, ApJ, 857, 56
Rolland B., Bergeron P., Fontaine G., 2020, ApJ, 889, 87
Ruiz-Macias O. et al., 2020, Res. Notes Am. Astron. Soc., 4, 187
Rybizki J. et al., 2020, PASP, 132, 074501
Rybizki J., Rix H.-W., Demleitner M., Bailer-Jones C. A. L., Cooper W. J., 2021, MNRAS, 500, 397
Schimeczek C., Wunner G., 2014a, Comput. Phys. Commun., 185, 614
Schimeczek C., Wunner G., 2014b, ApJS, 212, 26
Schlafly E. F. et al., 2023, AJ, 166,23
Schmidt G. D. et al., 2003, ApJ, 595, 1101
Schmidt G. D. et al., 2005, ApJ, 630, 1037
Schneider D. P. et al., 2007, AJ, 134, 102
Schreiber M. R., Gänsicke B. T., Toloza O., Hernandez M.-S., Lagos F., 2019, ApJ, 887, L4
Shen K. J., Blouin S., Breivik K., 2023, AJ Letters, 955, 10
Sion E. M., Greenstein J. L., Landstreet J. D., Liebert J., Shipman H. L., Wegner G. A., 1983, ApJ, 269, 253
Sion E. M., Aannestad P. A., Kenyon S. J., 1988, ApJ, 330, L55
Steele A., Debes J., Xu S., Yeh S., Dufour P., 2021, ApJ, 911, 25
Subasavage J. P., Henry T. J., Bergeron P., Dufour P., Hambly N. C., 2008, AJ, 136, 899
Swan A., Farihi J., Koester D., Holland s M., Parsons S., Cauley P. W., Redfield S., Gänsicke B. T., 2019, MNRAS, 490, 202
Swan A., Farihi J., Su K. Y. L., Desch S. J., 2024, MNRAS, 529, L41
Szkody P. et al., 2004, AJ, 128, 1882
Szkody P. et al., 2005, AJ, 129, 2386
Szkody P. et al., 2006, AJ, 131, 973
Tapia S., 1977, ApJ Lett., 212, L125
ter Braak C. J., Vrugt J. A., 2008, Stat. Comput., 18, 435
Tout C. A., Wickramasinghe D. T., Liebert J., Ferrario L., Pringle J. E., 2008, MNRAS, 387, 897
Tremblay P., Bergeron P., Kalirai J. S., Gianninas A., 2010, ApJ, 712, 1345
Tremblay P.-E., Ludwig H.-G., Steffen M., Bergeron P., Freytag B., 2011, A&A, 531, L19
Tremblay P. E., Ludwig H. G., Steffen M., Freytag B., 2013, A&A, 559, A104
Tremblay P. E., Cukanovaite E., Gentile Fusillo N. P., Cunningham T., Hollands M. A., 2019a, MNRAS, 482, 5222
Tremblay P.-E. et al., 2019b, Nature, 565, 202
Trierweiler I. L., Doyle A. E., Young E. D., 2023, Planet. Sci. J., 4, 13
Vanderburg A. et al., 2015, Nature, 526, 546
Vanlandingham K. M. et al., 2005, AJ, 130, 734
Vennes S., Kawka A., 2012, ApJ, 745, L12
Vennes S., Smith R. J., Boyle B. J., Croom S. M., Kawka A., Shanks T., Miller L., Loaring N., 2002, MNRAS, 335, 673
Vennes S., Kawka A., O'Toole S. J., Thorstensen J. R., 2012, ApJ, 756, L5
Vergely J. L., Lallement R., Cox N. L., 2022, A&A, 664, A174
Vincent O., Bergeron P., Dufour P., 2023, MNRAS, 521, 760
Vogel J., Byckling K., Schwope A., Osborne J. P., Schwarz R., Watson M. G., 2008, A&A, 485, 787
Vogt N., 1980, A&A, 88, 66
Watson M. G., Marsh T. R., Fender R. P., Barstow M. A., Still M., Page M., Dhillon V. S., Beardmore A. P., 1996, MNRAS, 281, 1016
Wenger M. et al., 2000, A&AS, 143, 9
Werner K., Herwig F., 2006, PASP, 118, 183
Wesemael F., Fontaine G., 1985, ApJ, 288, 764
Wickramasinghe D. T., Tout C. A., Ferrario L., 2014, MNRAS, 437, 675
Wilson T. G., Farihi J., Gänsicke B. T., Swan A., 2019, MNRAS, 487, 133
Zuckerman B., 2015, in Dufour P., Bergeron P., Fontaine G., eds, ASP Conf. Ser. Vol. 493, 19th European Workshop on White Dwarfs. Astron. Soc. Pac., San Francisco, p. 291
Zuckerman B., Becklin E. E., 1987, Nature, 330, 138
Zuckerman B., Reid I. N., 1998, ApJ, 505, L143
Zuckerman B., Koester D., Reid I. N., Hünsch M., 2003, ApJ, 596, 477
Zuckerman B., Koester D., Melis C., Hansen B. M., Jura M., 2007, ApJ, 671, 872

Downloaded from https://academic.oup.com/mnras/article/535/1/254/7774399 by guest on 09 December 2024

APPENDIX A: DESCRIPTION OF THE DESI EDR WHITE DWARF CATALOGUE

Table A1. Catalogue FITS extension one: the DESI EDR white dwarf catalogue. Parameters with a prefix of 'dr2' and 'edr3' are reproduced from the *Gaia* white dwarf catalogues of Gentile Fusillo et al. (2019, 2021), respectively.

Column	Heading	Description
1	wdj_name	WD J + RA (hh mm ss.ss) + Dec. (dd mm ss.s), equinox and epoch 2000
2	desi_sp_class	Spectral class determined from DESI EDR spectra
3	desi_id	DESI target ID (unique within DESI targeting)
4	desi_nexp	Number of exposures included in the DESI EDR
5	desi_stn_aiq	Signal-to-noise ratios of the DESI EDR blue-arm individual exposures added in quadrature
6	dr2_source_id	*Gaia* DR2 unique source identifier (unique within a particular data release)
7	dr2_ra	*Gaia* DR2 right ascension (J2015.5) [deg]
8	dr2_ra_error	*Gaia* DR2 standard error of right ascension ($\times \cos(\delta)$) [mas]
9	dr2_dec	*Gaia* DR2 declination (J2015.5) [deg]
10	dr2_dec_error	*Gaia* DR2 standard error of declination [mas]
11	dr2_parallax	*Gaia* DR2 absolute stellar parallax of the source at J2015.5 [mas]
12	dr2_parallax_error	*Gaia* DR2 standard error of parallax [mas]
13	dr2_pmra	*Gaia* DR2 proper motion in right ascension ($\times \cos(\delta)$) [mas yr^{-1}]
14	dr2_pmra_error	*Gaia* DR2 standard error of proper motion in right ascension [mas yr^{-1}]
15	dr2_pmdec	*Gaia* DR2 proper motion in declination [mas yr^{-1}]
16	dr2_pmdec_error	*Gaia* DR2 standard error of proper motion in declination [mas yr^{-1}]
17	dr2_astrometric_excess_noise	*Gaia* DR2 measure of the residuals in the astrometric solution for the source [mas]
18	dr2_astrometric_sigma5d_max	*Gaia* DR2 five-dimensional equivalent to the semi-major axis of the *Gaia* position error ellipse [mas]
19	dr2_phot_g_mean_flux	*Gaia* DR2 G-band mean flux [e^-/s]
20	dr2_phot_g_mean_flux_error	*Gaia* DR2 error on G-band mean flux [e^-/s]
21	dr2_phot_g_mean_mag	*Gaia* DR2 *Gaia* G-band mean magnitude (Vega scale) [mag]
22	dr2_phot_bp_mean_flux	*Gaia* DR2 integrated $G_{\rm BP}$ mean flux [e^-/s]
23	dr2_phot_bp_mean_flux_error	*Gaia* DR2 error on integrated $G_{\rm BP}$ mean flux [e^-/s]
24	dr2_phot_bp_mean_mag	*Gaia* DR2 integrated $G_{\rm BP}$ mean magnitude (Vega scale) [mag]
25	dr2_phot_rp_mean_flux	*Gaia* DR2 integrated $G_{\rm RP}$ mean flux [e^-/s]
26	dr2_phot_rp_mean_flux_error	*Gaia* DR2 error on integrated $G_{\rm RP}$ mean flux [e^-/s]
27	dr2_phot_rp_mean_mag	*Gaia* DR2 integrated $G_{\rm RP}$ mean magnitude (Vega scale) [mag]
28	dr2_phot_bp_rp_excess_factor	*Gaia* DR2 $G_{\rm BP}$ /$G_{\rm RP}$ excess factor estimated from the comparison of the sum of integrated
29	dr2_distance	*Gaia* DR2 distance determined using parallax by GF19
30	dr2_pwd	*Gaia* DR2 probability of being a white dwarf calculated by Gentile Fusillo et al. (2019)
31	dr2_pwd_flag	If 1 it indicates the *Gaia* DR2 $P_{\rm WD}$ value could be unreliable
32	dr2_Teff_H	*Gaia* DR2 effective temperature [K] determined by Gentile Fusillo et al. (2019) for pure-H model atmospheres
33	dr2_eTeff_H	*Gaia* DR2 uncertainty on effective temperature [K]
34	dr2_log_g_H	*Gaia* DR2 surface gravities [cm s^{-2}] determined by Gentile Fusillo et al. (2019) for pure-H model atmospheres
35	dr2_elog_g_H	*Gaia* DR2 uncertainty on surface gravities [cm s^{-2}]
36	dr2_mass_H	*Gaia* DR2 stellar mass [M$_\odot$] determined by Gentile Fusillo et al. (2019)
37	dr2_emass_H	*Gaia* DR2 uncertainty on the mass [M$_\odot$]
38	dr2_chi2_H	*Gaia* DR2 χ^2 value of the fit (pure-H)
39	dr2_Teff_He	*Gaia* DR2 effective temperature [K] determined by Gentile Fusillo et al. (2019) for pure-He model atmospheres
40	dr2_eTeff_He	*Gaia* DR2 uncertainty on effective temperature [K]
41	dr2_log_g_He	*Gaia* DR2 surface gravities [cm s^{-2}] determined by Gentile Fusillo et al. (2019) for pure-He model atmospheres
42	dr2_elog_g_He	*Gaia* DR2 uncertainty on surface gravities [cm s^{-2}]
43	dr2_mass_He	*Gaia* DR2 stellar mass [M$_\odot$] determined by Gentile Fusillo et al. (2019)
44	dr2_emass_He	*Gaia* DR2 uncertainty on the mass [M$_\odot$]
45	dr2_chisq_He	*Gaia* DR2 χ^2 value of the fit (pure-He)
46	edr3_source_id	*Gaia* EDR3 unique source identifier (unique within a particular data release)
47	edr3_ra	*Gaia* EDR3 right ascension (J2015.5) [deg]
48	edr3_ra_error	*Gaia* EDR3 standard error of right ascension ($\times \cos(\delta)$) [mas]
49	edr3_dec	*Gaia* EDR3 declination (J2015.5) [deg]
50	edr3_dec_error	*Gaia* EDR3 standard error of declination [mas]
51	edr3_parallax	*Gaia* EDR3 absolute stellar parallax of the source at J2015.5 [mas]
52	edr3_parallax_error	*Gaia* EDR3 standard error of parallax [mas]

Downloaded from https://academic.oup.com/mnras/article/535/1/254/7774399 by guest on 09 December 2024

Table A1 – *continued*

Column	Heading	Description
53	edr3_ZP_correction	*Gaia* EDR3 zero-point offset correction (Lindegren et al. 2021)
54	edr3_Pwd	*Gaia* EDR3 probability of being a white dwarf calculated by Gentile Fusillo et al. (2021)
55	edr3_density	The number of *Gaia* sources per square degree around this object
56	edr3_ref_epoch	*Gaia* EDR3 reference epoch (J2016.0)
57	edr3_pmra	*Gaia* EDR3 proper motion in right ascension ($\times \cos(\delta)$) [mas yr^{-1}]
58	edr3_pmra_error	*Gaia* EDR3 Standard error of proper motion in right ascension [mas yr^{-1}]
59	edr3_pmdec	*Gaia* EDR3 proper motion in declination [mas yr^{-1}]
60	edr3_pmdec_error	*Gaia* EDR3 standard error of proper motion in declination [mas yr^{-1}]
61	edr3_astrometric_excess_noise	*Gaia* EDR3 measure of the residuals in the astrometric solution for the source [mas]
62	edr3_astrometric_excess_noise_sig	*Gaia* EDR3 significance of the measure of the residuals in the astrometric solution
63	edr3_astrometric_params_solved	*Gaia* EDR3 number of parameters solved for the astrometric solution
64	edr3_astrometric_sigma5d_max	*Gaia* EDR3 five-dimensional equivalent to the semi-major axis of the *Gaia* position error ellipse [mas]
65	edr3_ruwe	*Gaia* EDR3 renormalized unit weight error
66	edr3_phot_g_n_obs	*Gaia* EDR3 number of observations contributing to G photometry
67	edr3_phot_g_mean_flux	*Gaia* EDR3 G-band mean flux [e^-/s]
68	edr3_phot_g_mean_flux_error	*Gaia* EDR3 error on G-band mean flux [e^-/s]
69	edr3_phot_g_mean_mag	*Gaia* EDR3 G-band mean magnitude (Vega scale) [mag]
70	edr3_phot_g_mean_mag_error	*Gaia* EDR3 error on G-band mean magnitude (Vega scale) [mag]
71	edr3_phot_g_mean_flux_corrected	*Gaia* EDR3 corrected G-band mean flux (Gaia Collaboration 2021)
72	edr3_phot_g_mean_mag_corrected	*Gaia* EDR3 corrected G-band mean magnitude (Vega scale) [mag] (Gaia Collaboration 2021)
73	edr3_phot_g_mean_mag_error_corrected	*Gaia* EDR3 corrected error on G-band mean magnitude (Vega scale) [mag] (Gaia Collaboration 2021)
74	edr3_phot_bp_n_obs	*Gaia* EDR3 number of observations contributing to $G_{\rm BP}$ photometry
75	edr3_phot_bp_mean_flux	*Gaia* EDR3 integrated $G_{\rm BP}$ mean flux [e^-/s]
76	edr3_phot_bp_mean_flux_error	*Gaia* EDR3 error on integrated $G_{\rm BP}$ mean flux [e^-/s]
77	edr3_phot_bp_mean_mag	*Gaia* EDR3 integrated $G_{\rm BP}$ mean magnitude (Vega scale) [mag]
78	edr3_phot_bp_mean_mag_error	*Gaia* EDR3 Error on integrated $G_{\rm BP}$ mean magnitude (Vega scale) [mag]
79	edr3_phot_rp_n_obs	*Gaia* EDR3 number of observations contributing to $G_{\rm RP}$ photometry
80	edr3_phot_rp_mean_flux	*Gaia* EDR3 integrated $G_{\rm BP}$ mean flux [e^-/s]
81	edr3_phot_rp_mean_flux_error	*Gaia* EDR3 error on integrated $G_{\rm BP}$ mean flux [e^-/s]
82	edr3_phot_rp_mean_mag	*Gaia* EDR3 integrated $G_{\rm BP}$ mean magnitude (Vega scale) [mag]
83	edr3_phot_rp_mean_mag_error	*Gaia* EDR3 error on integrated $G_{\rm RP}$ mean magnitude (Vega scale) [mag]
84	edr3_phot_bp_rp_excess_factor	*Gaia* EDR3 $G_{\rm BP}$ /$G_{\rm RP}$ excess factor estimated from the comparison of the sum of integrated
85	edr3_phot_bp_rp_excess_factor_corrected	*Gaia* EDR3 $G_{\rm BP}$ /$G_{\rm RP}$ excess factor corrected for colour dependence (Riello et al. 2021)
86	edr3_l	Galactic longitude [deg]
87	edr3_b	Galactic latitude [deg]
88	edr3_excess_flux_error	*Gaia* EDR3 metric for source photometric variability
89	edr3_meanAV	*Gaia* EDR3 mean extinction value (mag) derived from 3D reddening maps
90	edr3_minAV	*Gaia* EDR3 extinction value (mag) derived from 3D reddening maps using -1σ EDR3 distance
91	edr3_maxAV	*Gaia* EDR3 extinction value (mag) derived from 3D reddening maps using $+1\sigma$ EDR3 distance
92	edr3_flag_ext	*Gaia* EDR3 extinction flag (see Gentile Fusillo et al. 2021)
93	edr3_teff_H	*Gaia* EDR3 effective temperature [K] determined by Gentile Fusillo et al. (2021) for pure-H model atmospheres
94	edr3_eteff_H	*Gaia* EDR3 uncertainty on effective temperature [K]
95	edr3_logg_H	*Gaia* EDR3 surface gravities [cm s^{-2}] determined by Gentile Fusillo et al. (2021) for pure-H model atmospheres
96	edr3_elogg_H	*Gaia* EDR3 uncertainty on surface gravities [cm s^{-2}]
97	edr3_mass_H	*Gaia* EDR3 stellar mass [M$_\odot$] determined by Gentile Fusillo et al. (2021)
98	edr3_emass_H	*Gaia* EDR3 uncertainty on the mass [M$_\odot$]
99	edr3_chisq_H	*Gaia* EDR3 χ^2 value of the fit (pure-H)
100	edr3_teff_He	*Gaia* EDR3 effective temperature [K] determined by Gentile Fusillo et al. (2021) for pure-He model atmospheres
101	edr3_eteff_He	*Gaia* EDR3 uncertainty on effective temperature [K]
102	edr3_logg_He	*Gaia* EDR3 surface gravities [cm s^{-2}] determined by Gentile Fusillo et al. (2021) for pure-He model atmospheres
103	edr3_elogg_He	*Gaia* EDR3 uncertainty on surface gravities [cm s^{-2}]
104	edr3_mass_He	*Gaia* EDR3 stellar mass [M$_\odot$] determined by Gentile Fusillo et al. (2021)
105	edr3_emass_He	*Gaia* EDR3 uncertainty on the mass [M$_\odot$]
106	edr3_chisq_He	*Gaia* EDR3 χ^2 value of the fit (pure-He)
107	edr3_teff_mixed	*Gaia* EDR3 effective temperature [K] determined by Gentile Fusillo et al. (2021) for mixed H-He model atmospheres
108	edr3_eteff_mixed	*Gaia* EDR3 uncertainty on effective temperature [K]
109	edr3_logg_mixed	*Gaia* EDR3 surface gravities [cm s^{-2}] determined by Gentile Fusillo et al. (2021) for mixed H-He model atmospheres

Downloaded from https://academic.oup.com/mnras/article/535/1/254/7774399 by guest on 09 December 2024

Table A1 – *continued*

Column	Heading	Description
110	edr3_elogg_mixed	*Gaia* EDR3 uncertainty on surface gravities [cm s^{-2}]
111	edr3_mass_mixed	*Gaia* EDR3 stellar mass [M$_\odot$] determined by Gentile Fusillo et al. (2021)
112	edr3_emass_mixed	*Gaia* EDR3 uncertainty on the mass [M$_\odot$]
113	edr3_chisq_mixed	*Gaia* EDR3 χ^2 value of the fit (mixed H-He)
114	edr3_r_med_geo	Median of the geometric distance posterior (pc) (Bailer-Jones et al. 2021)
115	edr3_r_lo_geo	16th percentile of the geometric distance posterior (pc) (Bailer-Jones et al. 2021)
116	edr3_r_hi_geo	84th percentile of the geometric distance posterior (pc) (Bailer-Jones et al. 2021)
117	edr3_r_med_photogeo	Median of the photogeometric distance posterior (pc) (Bailer-Jones et al. 2021)
118	edr3_r_lo_photogeo	16th percentile of the photomgeometric distance posterior (pc) (Bailer-Jones et al. 2021)
119	edr3_r_hi_photogeo	84th percentile of the photomgeometric distance posterior (pc) (Bailer-Jones et al. 2021)
120	edr3_fidelity_v1	'Astrometric fidelity' metric from Rybizki et al. (2021)
121	umag_sdss	SDSS *u*-band magnitude [mag]
122	e_umag_sdss	SDSS *u*-band magnitude uncertainty [mag]
123	gmag_sdss	SDSS *g*-band magnitude [mag]
124	e_gmag_sdss	SDSS *g*-band magnitude uncertainty [mag]
125	rmag_sdss	SDSS *r*-band magnitude [mag]
126	e_rmag_sdss	SDSS *r*-band magnitude uncertainty [mag]
127	imag_sdss	SDSS *i*-band magnitude [mag]
128	e_imag_sdss	SDSS *i*-band magnitude uncertainty [mag]
129	zmag_sdss	SDSS *z*-band magnitude [mag]
130	e_zmag_sdss	SDSS *z*-band magnitude uncertainty [mag]
131	gmag_ps1	Pan-STARRS DR1 *g*-band magnitude [mag]
132	e_gmag_ps1	Pan-STARRS DR1 *g*-band magnitude uncertainty [mag]
133	gFlags_ps1	Flags on Pan-STARRS DR1 *g*-band magnitude
134	rmag_ps1	Pan-STARRS DR1 *r*-band magnitude [mag]
135	e_rmag_ps1	Pan-STARRS DR1 *r*-band magnitude uncertainty [mag]
136	rFlags_ps1	Flags on Pan-STARRS DR1 *r*-band magnitude
137	imag_ps1	Pan-STARRS DR1 *i*-band magnitude [mag]
138	e_imag_ps1	Pan-STARRS DR1 *i*-band magnitude uncertainty [mag]
139	iFlags_ps1	Flags on Pan-STARRS DR1 *i*-band magnitude
140	zmag_ps1	Pan-STARRS DR1 *z*-band magnitude [mag]
141	e_zmag_ps1	Pan-STARRS DR1 *z*-band magnitude uncertainty [mag]
142	zFlags_ps1	Flags on Pan-STARRS DR1 *z*-band magnitude
143	ymag_ps1	Pan-STARRS DR1 *y*-band magnitude [mag]
144	e_ymag_ps1	Pan-STARRS DR1 *y*-band magnitude uncertainty [mag]
145	yFlags_ps1	Flags on Pan-STARRS DR1 *y*-band magnitude
146	fuvmag_galex	*GALEX* FUV magnitude [mag]
147	e_fuvmag_galex	*GALEX* FUV magnitude uncertainty [mag]
148	nuvmag_galex	*GALEX* NUV magnitude [mag]
149	e_nuvmag_galex	*GALEX* NUV magnitude uncertainty [mag]
150	ext_tomog	Visual (5500 Å) extinction [mag] from TOMO-G (https://explore-platform.eu/sda/g-tomo)
151	ext_err_tomog	Visual (5500 Å) extinction uncertainity [mag] from TOMO-G (https://explore-platform.eu/sda/g-tomo)
152	simbad_main_id	Main identifier for given crossmatched source in the SIMBAD database (Wenger et al. 2000)
153	simbad_main_type	Main astronomical source type for given cross-matched source in the SIMBAD database (Wenger et al. 2000)
154	simbad_other_types	Other astronomical source types for given cross-matched source in the SIMBAD database (Wenger et al. 2000)
155	simbad_sp_type	Spectral type for the given cross-matched source by the SIMBAD database (Wenger et al. 2000)
156	simbad_angDist	Distance between DESI source and given cross-matched source in the SIMBAD database (Wenger et al. 2000)
157	simbad_nbref	Number of references associated with given source in the SIMBAD database (Wenger et al. 2000)
158	mwdd_name	Identifier given by the Montreal White Dwarf Database (Dufour et al. 2017)
159	mwdd_ra	Right ascension given by the Montreal White Dwarf Database (Dufour et al. 2017)
160	mwdd_dec	Declination given by the Montreal White Dwarf Database (Dufour et al. 2017)
161	mwdd_sp_class	Spectral type given by the Montreal White Dwarf Database (Dufour et al. 2017)
162	mwdd_teff	Effective temperature [K] given by the Montreal White Dwarf Database (Dufour et al. 2017)
163	mwdd_logg	Surface gravity [cm s^{-2}] given by the Montreal White Dwarf Database (Dufour et al. 2017)
164	mwdd_desi_separation	Separation between DESI source and cross-matched source in the Montreal White Dwarf Database (Dufour et al. 2017)

Downloaded from https://academic.oup.com/mnras/article/535/1/254/7774399 by guest on 09 December 2024

Table A2. Catalogue FITS extension two: cross-matched SDSS spectra.

Column	Heading	Description
1	wdj_name	WD J + RA (hh mm ss.ss) + Dec. (dd mm ss.s), equinox and epoch 2000
2	plate	Plate identifier for a unique SDSS spectrum
3	mjd	MJD identifier for a unique SDSS spectrum
4	fibreid	Fibre identifier for a unique SDSS spectrum
5	desi_sdss_separation	Separation between DESI source and cross-matched source in the SDSS sample
6	n_sdss_spec	Number of unique SDSS spectra cross-matched to a given white dwarf in the DESI EDR sample

Table A3. Catalogue FITS extension three: photometric fits to DESI EDR DA white dwarfs.

Column	Heading	Description
1	wdj_name	WD J + RA (hh mm ss.ss) + Dec. (dd mm ss.s), equinox and epoch 2000
2	teff	Effective temperature [K] obtained from fit
3	teff_err	Error on effective temperature [K] obtained from fit
4	logg	Surface gravity [cm s^{-2}] obtained from fit
5	logg_err	Error on surface gravity [cm s^{-2}] obtained from fit
6	d_fitted	Distance [pc] obtained from the fit
7	d_fitted_err	Error on the distance [pc] obtained from the fit

Table A4. Catalogue FITS extension four: spectroscopic fits to DESI EDR DA white dwarfs.

Column	Heading	Description
1	wdj_name	WD J + RA (hh mm ss.ss) + Dec. (dd mm ss.s), equinox and epoch 2000
2	teff	Effective temperature [K] obtained from fit
3	teff_err	Error on effective temperature [K] obtained from fit
4	logg	Surface gravity [cm s^{-2}] obtained from fit
5	logg_err	Error on surface gravity [cm s^{-2}] obtained from fit
6	teff_3D_0.8	Effective temperature [K] obtained from fit after applying 3D corrections of Tremblay et al. (2011)
7	logg_3D_0.8	Surface gravity [cm s^{-2}] obtained from fit after applying 3D corrections of Tremblay et al. (2011)

Table A5. Catalogue FITS extension five: spectroscopic fits to SDSS DA white dwarfs.

Column	Heading	Description
1	wdj_name	WD J + RA (hh mm ss.ss) + Dec. (dd mm ss.s), equinox and epoch 2000
2	mjd	MJD identifier for a unique SDSS spectrum
3	plate	Plate identifier for a unique SDSS spectrum
4	fibreid	Fibre identifier for a unique SDSS spectrum
5	teff	Effective temperature [K] obtained from fit
6	teff_err	Error on effective temperature [K] obtained from fit
7	logg	Surface gravity [cm s^{-2}] obtained from fit
8	logg_err	Error on surface gravity [cm s^{-2}] obtained from fit
9	teff_3D_0.8	Effective temperature [K] obtained from fit after applying 3D corrections of Tremblay et al. (2011)
10	logg_3D_0.8	Surface gravity [cm s^{-2}] obtained from fit after applying 3D corrections of Tremblay et al. (2011)

Table A6. Catalogue FITS extension six: photometric fits to DESI EDR DB white dwarfs.

Column	Heading	Description
1	wdj_name	WD J + RA (hh mm ss.ss) + Dec. (dd mm ss.s), equinox and epoch 2000
2	teff	Effective temperature [K] obtained from fit
3	teff_err	Error on effective temperature [K] obtained from fit
4	logg	Surface gravity [cm s^{-2}] obtained from fit
5	logg_err	Error on surface gravity [cm s^{-2}] obtained from fit
6	d_fitted	Distance [pc] obtained from the fit
7	d_fitted_err	Error on the distance [pc] obtained from the fit

Downloaded from https://academic.oup.com/mnras/article/535/1/254/7774399 by guest on 09 December 2024

Table A7. Catalogue FITS extension seven: spectroscopic fits to DESI EDR DB white dwarfs.

Column	Heading	Description
1	wdj_name	WD J + RA (hh mm ss.ss) + Dec. (dd mm ss.s), equinox and epoch 2000
2	teff	Effective temperature [K] obtained from fit
3	teff_err	Error on effective temperature [K] obtained from fit
4	logg	Surface gravity [cm s^{-2}] obtained from fit
5	logg_err	Error on surface gravity [cm s^{-2}] obtained from fit
6	teff_3D_0.8	Effective temperature [K] obtained from fit after applying 3D corrections of Cukanovaite et al. (2021)
7	logg_3D_0.8	Surface gravity [cm s^{-2}] obtained from fit after applying 3D corrections of Cukanovaite et al. (2021)

Table A8. Catalogue FITS extension eight: spectroscopic fits to SDSS DB white dwarfs.

Column	Heading	Description
1	wdj_name	WD J + RA (hh mm ss.ss) + Dec. (dd mm ss.s), equinox and epoch 2000
2	mjd	MJD identifier for a unique SDSS spectrum
3	plate	Plate identifier for a unique SDSS spectrum
4	fibre	Fibre identifier for a unique SDSS spectrum
5	teff	Effective temperature [K] obtained from fit
6	teff_err	Error on effective temperature [K] obtained from fit
7	logg	Surface gravity [cm s^{-2}] obtained from fit
8	logg_err	Error on surface gravity [cm s^{-2}] obtained from fit
9	teff_3D_0.8	Effective temperature [K] obtained from fit after applying 3D corrections of Cukanovaite et al. (2021)
10	logg_3D_0.8	Surface gravity [cm s^{-2}] obtained from fit after applying 3D corrections of Cukanovaite et al. (2021)

Table A9. Catalogue FITS extension nine: photometric fits to DESI EDR DBA/DAB white dwarfs.

Column	Heading	Description
1	wdj_name	WD J + RA (hh mm ss.ss) + Dec. (dd mm ss.s), equinox and epoch 2000
2	teff	Effective temperature [K] obtained from fit
3	teff_err	Error on effective temperature [K] obtained from fit
4	logg	Surface gravity [cm s^{-2}] obtained from fit
5	logg_err	Error on surface gravity [cm s^{-2}] obtained from fit
6	d_fitted	Distance [pc] obtained from the fit
7	d_fitted_err	Error on the distance [pc] obtained from the fit

Table A10. Catalogue FITS extension 10: spectroscopic fits to DESI EDR DBA/DAB white dwarfs.

Column	Heading	Description
1	wdj_name	WD J + RA (hh mm ss.ss) + Dec. (dd mm ss.s), equinox and epoch 2000
2	teff	Effective temperature [K] obtained from fit
3	teff_err	Error on effective temperature [K] obtained from fit
4	logg	Surface gravity [cm s^{-2}] obtained from fit
5	logg_err	Error on surface gravity [cm s^{-2}] obtained from fit
6	h_he	log (H/He) obtained from fit
7	h_he_err	Error on log (H/He) obtained from fit
8	teff_3D_0.8	Effective temperature [K] obtained from fit after applying 3D corrections of Cukanovaite et al. (2021)
9	logg_3D_0.8	Surface gravity [cm s^{-2}] obtained from fit after applying 3D corrections of Cukanovaite et al. (2021)

Table A11. Catalogue FITS extension 11: spectroscopic fits to DESI EDR DQx white dwarfs.

Column	Heading	Description
1	wdj_name	WD J + RA (hh mm ss.ss) + Dec. (dd mm ss.s), equinox and epoch 2000
2	teff	Effective temperature [K] obtained from fit
3	teff_err	Error on effective temperature [K] obtained from fit
4	logg	Surface gravity [cm s^{-2}] obtained from fit
5	logg_err	Error on surface gravity [cm s^{-2}] obtained from fit
6	mass	Mass ($M_{\odot}$) obtained from fit
7	c_he	log (C/He) abundance obtained from fit
8	c_he_err	Error on the log (C/He) abundance obtained from fit

Downloaded from https://academic.oup.com/mnras/article/535/1/254/7774399 by guest on 09 December 2024

APPENDIX B: DETAILS AND VALIDATION OF THE DA, DB, AND DBA FITTING ROUTINES

The synthetic spectra used in the fitting procedure are generated by the latest version of the Koester (2010) code. The convection zones are modelled employing the 1D ML approximation, with the ML2 parametrization and a fixed convective efficiency α set to 0.8 and 1.25 for the DAs and DBs/D(AB)s, respectively (the canonical values in the treatment of H- and He-dominated photospheres, Tremblay et al. 2010; Bergeron et al. 2011).

The ranges and steps in $T_{\rm eff}$ that cover each of the employed grids of synthetic spectra vary with chemical composition. Pure H models are used to fit the DA spectra, spanning $5000 \leq T_{\rm eff} \leq 80\,000$ K in steps of 250, 1000, 2000, and 5000 K up to 20 000, 30 000, 40 000, and 80 000 K, respectively. We employed pure He models for DBs, which covered $9000 \leq T_{\rm eff} \leq 40\,000$ K in steps of 250, 1000, and 2000 K up to 20 000, 30 000, and 40 000 K, since the He I transitions disappear from the spectrum below 9000 K and above 40 000 K He II transitions are visible. The D(AB)s were fit with an H + He grid, equivalent to the pure He one in terms of $T_{\rm eff}$ since the same reasoning applies. The three grids spanned surface gravities $7.0 \leq \log g \leq 9.5$ in steps of 0.25 dex. To obtain estimates on the H content, the H + He grid covered $-7.0 \leq \log({\rm H/He}) \leq -3.0$ in steps of 0.25 dex.

For both the spectroscopic and photometric analyses, we used the Markov Chain Monte Carlo EMCEE package within PYTHON (Foreman-Mackey et al. 2013), following procedures established in previous work (Izquierdo et al. 2023) with some modifications that are explained in the following subsections. In all cases, chains were initialized with 30 walkers distributed randomly across the parameter space. Autocorrelation times were calculated and used to test for convergence (following the guidelines in the EMCEE documentation), to identify and discard a burn-in section, and to select 10 000 independent samples from the ends of the chains.

B1 Spectroscopic fitting

We performed spectroscopic analyses to the DESI co-added spectra and, when available, the SDSS archival spectroscopy, using up to three free parameters, namely $T_{\rm eff}$, $\log g$, and log(H/He). The fitting technique is analogous to that presented in Izquierdo et al. (2023) except for the normalization procedure. In this work, we do not normalize the spectra by the continuum. Instead, the useful spectral regions (Balmer and/or He I transitions) were split in smaller windows. Each of these windows sample, at least, an absorption line and its surroundings. The total flux of each window is integrated and each data point contained in the window is divided by this value. The same normalization is applied to both observed and synthetic spectra. The windows span 220 and 200 Å for the DAs and DB/D(AB)s, respectively. These optimal widths were identified through various internal tests with independent studies.

A purely spectroscopic fit usually has two degenerate solutions that can differ significantly in $T_{\rm eff}$, and are called the hot and cold solutions. This is due to the EWs of the Balmer absorption lines reaching a maximum around 13 000 K (Rebassa-Mansergas et al. 2007); and because the EW of the He I transitions reach a plateau between 22 000 to 33 000 K (dependent on the $\log g$, Bergeron et al. 2001). In order to overcome this degeneracy, we performed two fits to each white dwarf: one using only cool synthetic spectra, and a second fit employing hot synthetic spectra, with some overlap between the two subsets. For the DAs, these translated into cool models up to 15 000 K and hot ones down to 13 000 K. For the DBs and D(AB)s, the cool models reached to 27 000 K and the hot ones went down to 22 000 K.

Due to this degeneracy, the default EMCEE setup is unsuitable as it is tuned to problems with unimodal parameters. To ensure proper exploration of the posteriors, we used differential evolution proposals, so that walkers are able to move freely between widely separated modes (ter Braak & Vrugt 2008; Nelson, Ford & Payne 2013). Specifically, we used `DEMove` with stretch factor $\gamma = 1.17$ for 81 per cent of the moves, `DESnookerMove` ($\gamma = 2.38/\sqrt{2}$) for 9 per cent, `DEMove` ($\gamma = 1$) for 9 per cent, and `DESnookerMove` ($\gamma = 1$) for 1 per cent.

To decide between the cold and hot solution for each H-dominated white dwarf, we followed the procedures presented in Rebassa-Mansergas et al. (2007) to evaluate the true value (the photometric result, since it is not subject to the EW degeneracy) against the theoretical value. We measured the EW of the Balmer lines in our models, and fit a polynomial in $T_{\rm eff} - \log g$ space to the peak values. That way, if the independently fit photometric solution falls on the hot side of that polynomial, we select the hot spectroscopic fit, similarly for the cold side/fit.

For the DB/D(AB)s, there is no such study performed, so we chose between the hot and cold solutions by proximity to the photometric result of each star.

We applied the 3D corrections to convert 1D spectroscopic values to 3D atmospheric parameters, following the prescriptions of Tremblay et al. (2011) and Cukanovaite et al. (2021). These results are available in the online catalogue and used throughout the paper when specified.

B2 Photometric fitting

We modelled photometric archival data from SDSS, Pan-STARRS, *Gaia* DR2, and EDR3 to test our spectroscopic results. These photometric analyses fitted for the $T_{\rm eff}$, $\log g$, and distance, D, as free parameters and followed the same prescription as in Izquierdo et al. (2023) with a few variations. The model fluxes were scaled by the solid angle of the star $\pi(R_{\rm WD}/D)$, with $R_{\rm WD}$ the radius of the white dwarf derived from evolutionary models from Althaus, Miller Bertolami & Córsico (2013). The photometric data were supplemented by *Gaia* parallaxes, but some of the white dwarfs have imprecise measurements. We therefore used a distance prior constructed following the popular prescription of Bailer-Jones et al. (2021) but generated only from sources with $\log g > 7$ from the mock *Gaia* EDR3 catalogue (Rybizki et al. 2020). The synthetic spectra were reddened by querying the G-Tomo 3D dust map (Fitzpatrick 1999; Lallement et al. 2022; Vergely, Lallement & Cox 2022) at the inverse-parallax distance, adopting a total-to-selective extinction ratio of $R_V = 3.1$, and then integrating over the SDSS bandpasses.

B3 Validation of DA fitting method

In order to test the accuracy of our spectroscopic $T_{\rm eff}$ and $\log g$ drawn from the DESI EDR spectra we compared them to different sets of data in Figs B1 and B2. We use the same notation as in Figs B1 and B2, where A and B refer to the two samples that are being compared in a respective panel.

Downloaded from https://academic.oup.com/mnras/article/535/1/254/7774399 by guest on 09 December 2024

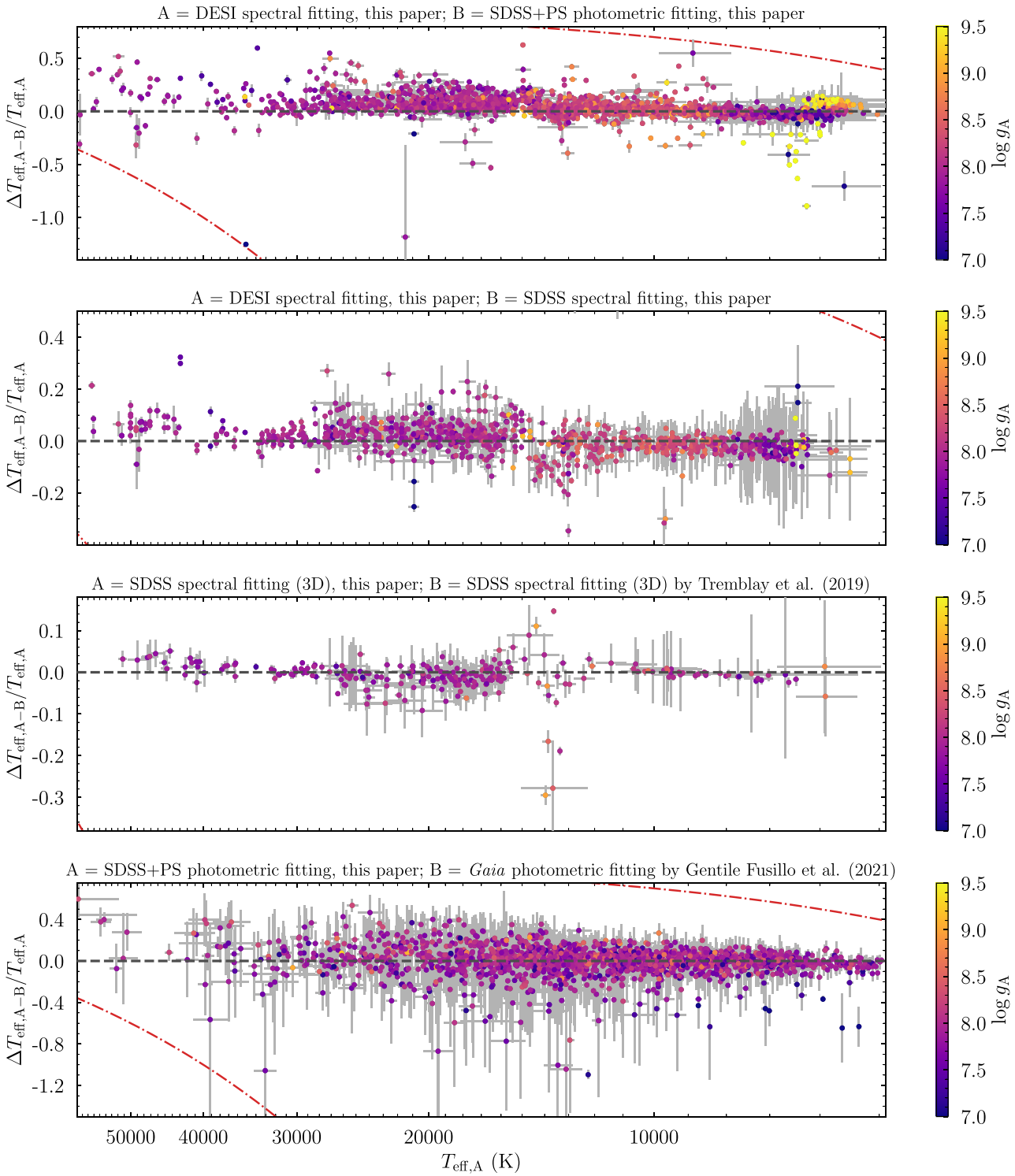

Figure B1. Comparisons of our measured spectroscopic and photometric effective temperatures for DA white dwarfs observed by DESI with several other samples. Data sets are labelled 'A' and 'B', with definitions given in the heading of each panel. Data points colour-coded by their determined surface gravities. Red dotted–dashed lines show the curves $y = (T_{\rm eff,A} - 3000)/T_{\rm eff,A}$, and $y = (T_{\rm eff,A} - 80000)/T_{\rm eff,A}$, indicating the bounds of our model grid. From top to bottom, we compare: (1) our spectroscopic fitting of DESI spectra with our photometric fitting using SDSS and Pan-STARRS photometry; (2) our spectroscopic fitting of DESI spectra with our spectroscopic fitting of SDSS spectra where a given DA has been observed by both DESI and SDSS; (3) our spectroscopic fitting of SDSS spectra with spectroscopic 3D fitting by Tremblay et al. (2019a) with DAs observed by DESI within the sample of stars modelled by Tremblay et al. (2019a); and (4) our photometric fitting using SDSS and Pan-STARRS photometry with *Gaia* photometric fits of GF21 for DA white dwarfs observed by DESI.

Downloaded from https://academic.oup.com/mnras/article/535/1/254/7774399 by guest on 09 December 2024

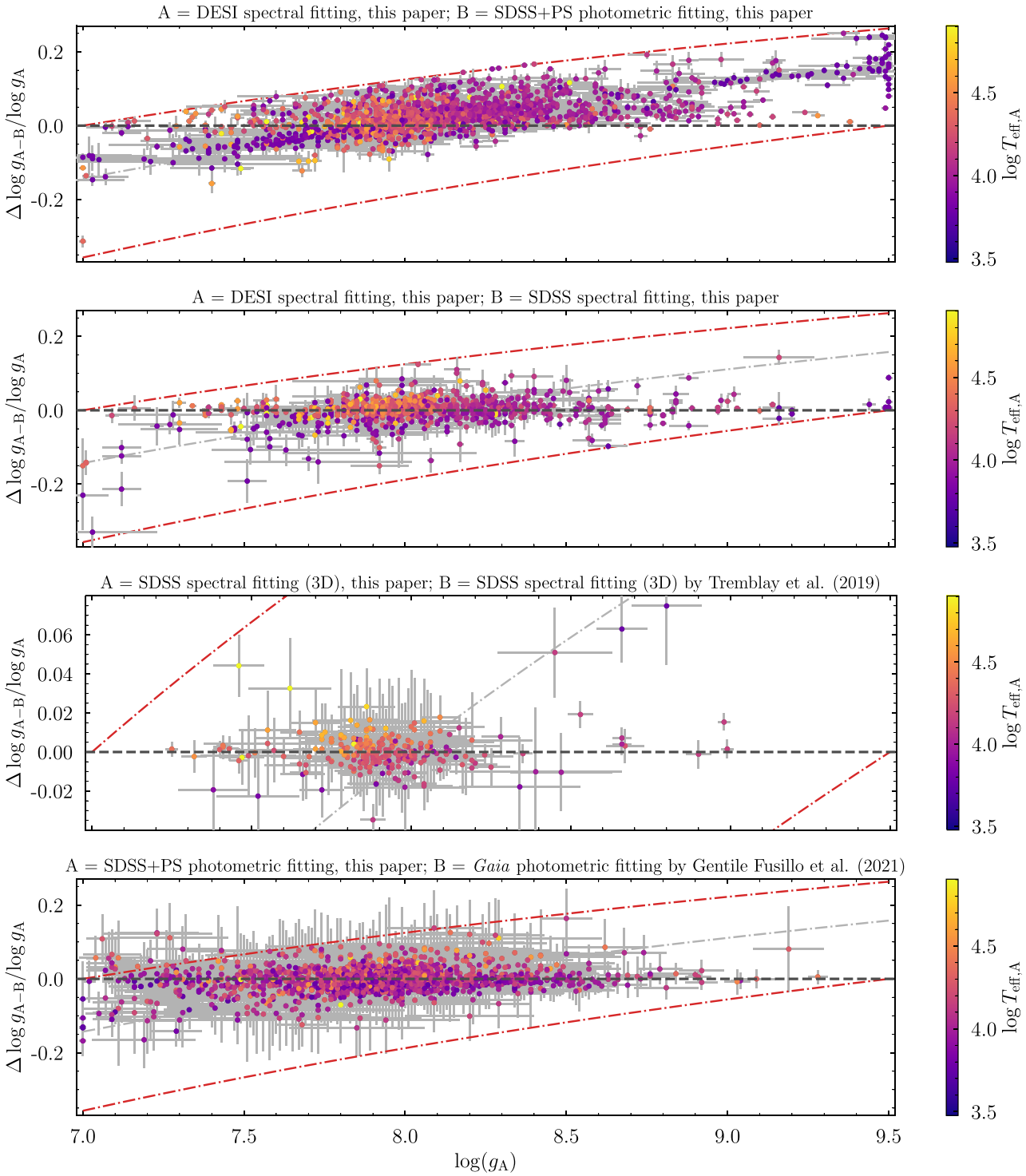

Figure B2. As in Fig. B1, but comparisons are shown for surface gravities with points colour-coded by their determined effective temperatures. Red dotted–dashed lines show the curves $y = (\log g_{\rm A} - 7.0)/\log g_{\rm A}$, and $y = (\log g_{\rm A} - 9.5)/\log g_{\rm A}$, indicating the bounds of our model grid. The grey dotted–dashed line marks the canonical $y = (\log g_{\rm A} - 8.0)/\log g_{\rm A}$.

For the comparison of our spectroscopic DESI results (A) with an internal photometric test we chose the SDSS and Pan-STARRS catalogues (B). In general, there is good agreement between the spectroscopic and photometric results, with a weighted mean $\langle \Delta T_{\rm eff,A-B}/T_{\rm eff,A} \rangle = 0.15 \pm 0.22$ and $\langle \Delta \log g_{\rm A-B}/\log g_{\rm A} \rangle = 0.04 \pm 0.05$. In particular, we are obtaining higher $T_{\rm eff}$ from the DESI spectroscopic analysis than that derived from photometry, which is most significant above $T_{\rm eff} \geq 15\,000$ K, which is also observed in other DA population studies that compare spectroscopic and photometric solutions (Genest-Beaulieu & Bergeron 2019; Tremblay et al. 2019a; O'Brien et al. 2023). This is also illustrated in the individual mean and standard deviations for the hotter objects ($\langle \Delta T_{\rm eff,A-B}/T_{\rm eff,A} \rangle = 0.34 \pm 0.24$), compared to the objects

Downloaded from https://academic.oup.com/mnras/article/535/1/254/7774399 by guest on 09 December 2024

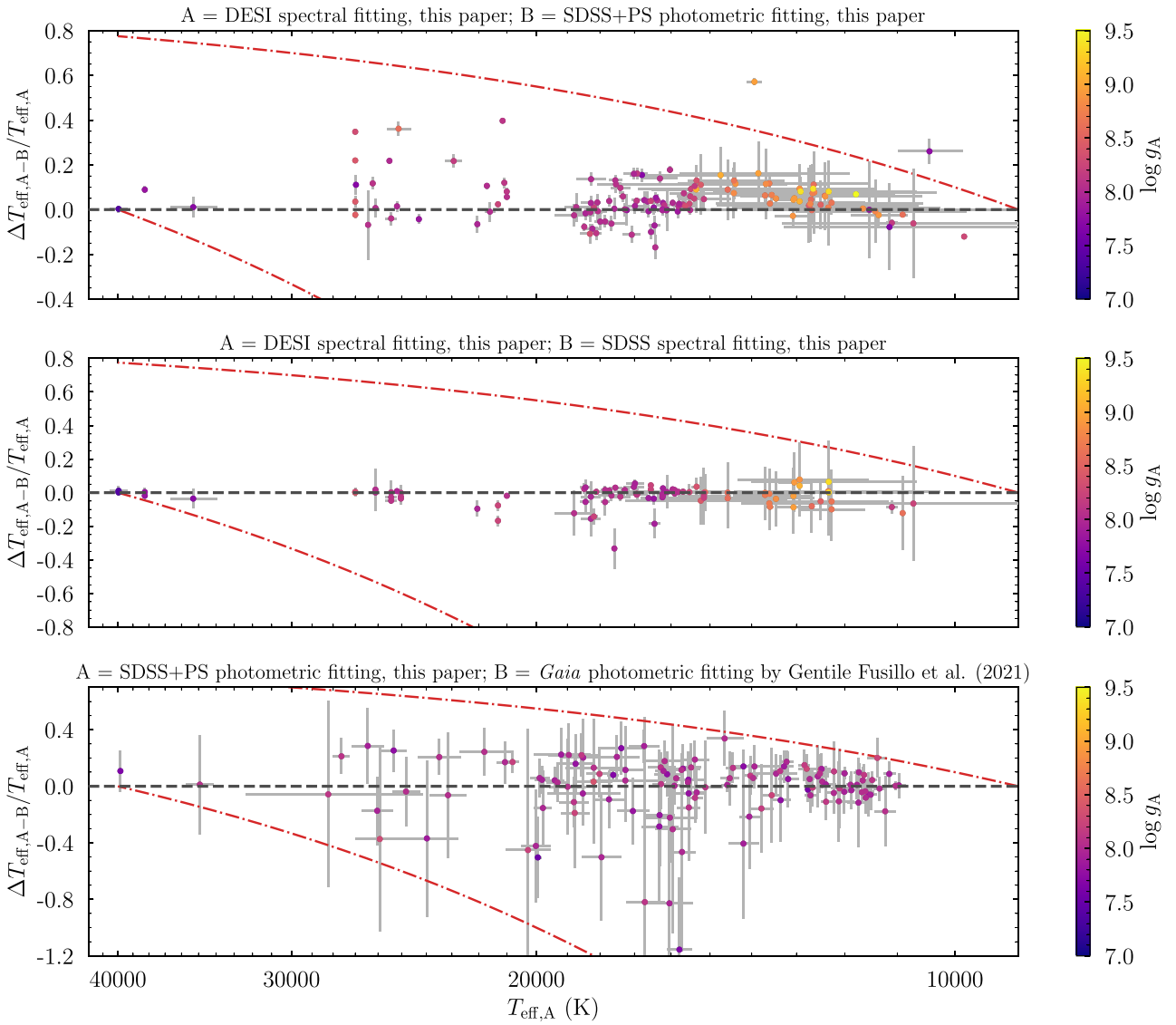

Figure B3. Comparisons of our measured spectroscopic and photometric effective temperatures for DB white dwarfs observed by DESI with several other samples. Data sets are labelled 'A' and 'B', with definitions given in the heading of each panel. Data points colour-coded by their determined surface gravities. Red dotted–dashed lines show the curves $y = (T_{\rm eff,A} - 40\,000)/T_{\rm eff,A}$, and $y = (T_{\rm eff,A} - 9000)/T_{\rm eff,A}$, indicating the bounds of our model grid. From top to bottom, we compare: (1) our spectroscopic fitting of DESI spectra with our photometric fitting using SDSS and Pan-STARRS photometry; (2) our spectroscopic fitting of DESI spectra with our spectroscopic fitting of SDSS spectra where a given DB has been observed by both DESI and SDSS; and (3) our photometric fitting using SDSS and Pan-STARRS photometry with *Gaia* photometric fits of GF21 for DB white dwarfs observed by DESI.

with $T_{\rm eff} \leq 15\,000$ K of 0.056 ± 0.13. The large discrepancies obtained for white dwarfs with $T_{\rm eff} \geq 30\,000$ K are likely related to the loss of sensitivity to $T_{\rm eff}$ that affects optical photometry as $T_{\rm eff}$ increases, becoming unreliable as the observed spectral energy distribution reaches the Rayleigh–Jeans regime.

We fit the archival SDSS spectra of the 963 DA white dwarfs (B) in the same way as the DESI EDR spectra (A) to validate our results. If we remove from the sample two low signal-to-noise ratio SDSS spectra (those corresponding to WDJ140151.43+032946.46 and WDJ140547.76−013454.94), which lead to meaningless values both compared to our DESI spectroscopic results and the literature values obtained from photometry, we find $\langle \Delta T_{\rm eff,A-B}/T_{\rm eff,A} \rangle = 0.02 \pm 0.05$ and $\langle \Delta \log g_{\rm A-B}/\log g_{\rm A} \rangle = 0.01 \pm 0.02$. This is an excellent agreement given the low signal-to-noise ratio of several of the SDSS spectra compared to DESI. In fact, these figures are in line with the ones seen in literature for independent analyses performed on different spectroscopic data sets (Genest-Beaulieu & Bergeron 2014).

Some of the SDSS stars that also feature in the DESI EDR sample were fit by Tremblay et al. (2019a) and the comparison between their analysis (B) and ours (A), both with 3D corrections applied, yields $\langle \Delta T_{\rm eff,A-B}/T_{\rm eff,A} \rangle = -0.002 \pm 0.031$ and $\langle \Delta \log g_{\rm A-B}/\log g_{\rm A} \rangle = -0.0003 \pm 0.0072$. The biggest discrepancies are found in the region where the hot and cold solutions are split and hence, systematic uncertainties due to the different approaches may arise.

The spectroscopic and photometric comparison performed in this work relies on the validity of both types of analyses. We have compared our DESI EDR spectroscopic results with two independent samples and thus we need to contrast too the goodness of our photometric fit. This

Downloaded from https://academic.oup.com/mnras/article/535/1/254/7774399 by guest on 09 December 2024

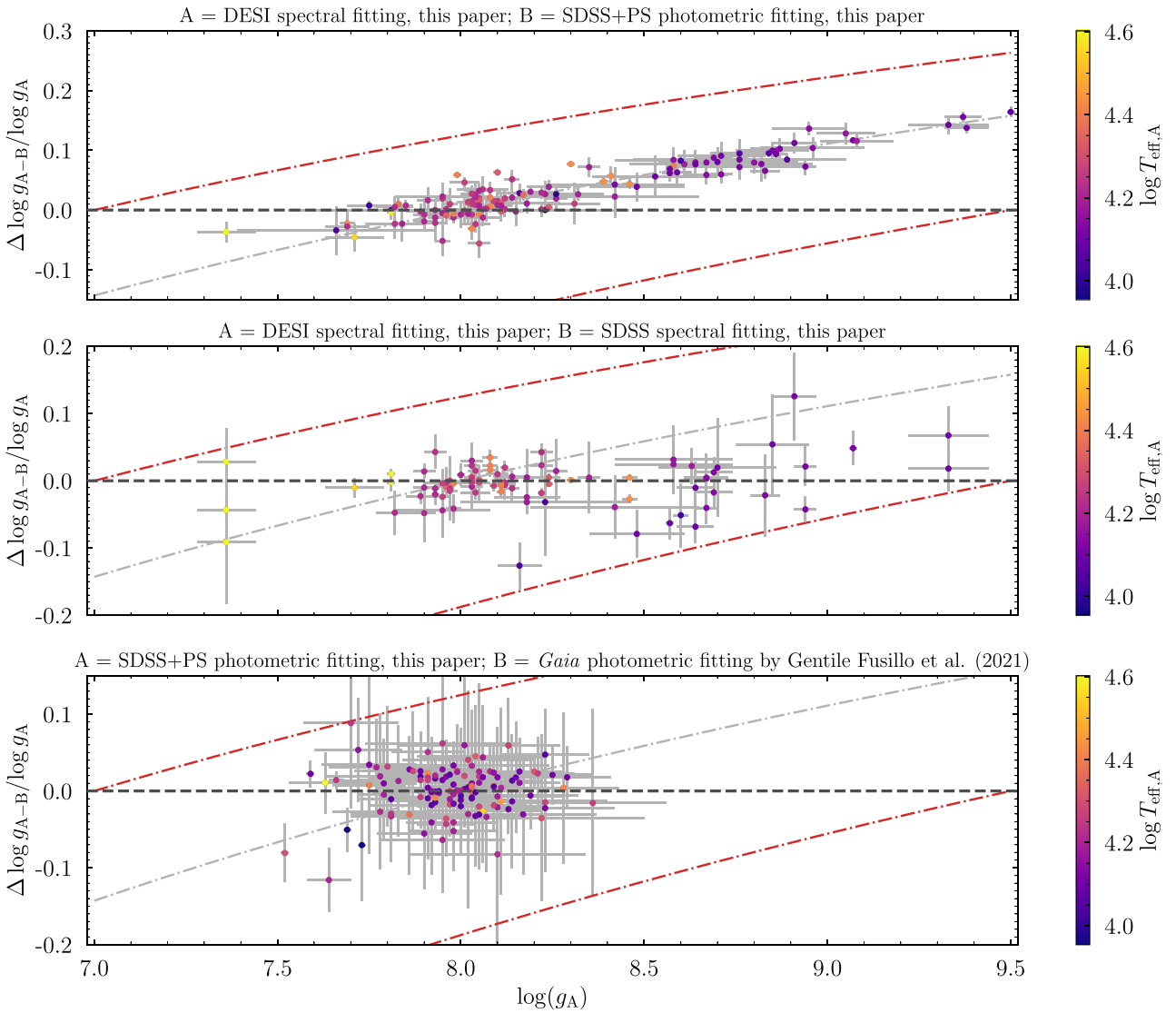

Figure B4. As in Fig. B3, but comparisons are shown for surface gravities with points colour-coded by their determined effective temperatures. Red dotted–dashed lines show the curves $y = (\log g_{\rm A} - 7.0)/\log g_{\rm A}$, and $y = (\log g_{\rm A} - 9.5)/\log g_{\rm A}$, indicating the bounds of our model grid. The grey dotted–dashed line marks the canonical $y = (\log g_{\rm A} - 8.0)/\log g_{\rm A}$.

comparison between our photometric fitting (A), and the photometric catalogue of Gentile Fusillo et al. (2021) (B), is displayed in the bottom panels of Figs B1 and B2. We obtained $\langle \Delta T_{\rm eff,A-B}/T_{\rm eff,A} \rangle = 0.007 \pm 0.087$ and $\langle \Delta \log g_{\rm A-B}/\log g_{\rm A} \rangle = -0.002 \pm 0.016$, which are both on the order of the uncertainties obtained when fitting independent photometric catalogues (see figs 7–10 of GF19).

B4 Validation of DB fitting method

Our spectroscopic results drawn from the DESI EDR spectra for the DB white dwarfs are contrasted to independent analyses in Figs B3 and B4. As for the DA white dwarfs, we use the notation of Figs B3 and B4 when describing the comparison between two given samples.

The comparison between the spectroscopic (A) and photometric (B) techniques we developed (top panels in Figs B3 and B4) highlights the non-physical increase in spectroscopic $\log g$ below $T_{\rm eff} \simeq 15\,000$ K. Within the same regime, we have identified two objects whose photometrically derived $T_{\rm eff}$ fall outside our spectroscopic grid boundaries, as indicated by the red dotted–dashed lines. This is because the He I transitions are only visible above $T_{\rm eff} \simeq 9000$ K but the photometric solutions can cover cooler temperatures as well, including DC spectral types. Inspection of these two systems in more details revealed that the observed photometry did not appear consistent, and that the spectroscopic solutions are preferred. The $T_{\rm eff}$ differences between 20 000 and 30 000 K originate from the difficulty to obtain accurate photometric parameters in the instability strip of DBs (where they pulsate) and its coincidence with the maximum of the EW for He I lines, where the hot and cold technique is necessary but forces sharp boundaries in $T_{\rm eff}$. In general, we find a weighted mean of $\langle \Delta T_{\rm eff,A-B}/T_{\rm eff,A} \rangle = 0.15 \pm 0.19$ and $\langle \Delta \log g_{\rm A-B}/\log g_{\rm A} \rangle = 0.05 \pm 0.04$, similar to the values seen in the literature (Tremblay et al. 2019a). If we calculate those values for the objects with photometric $T_{\rm eff}$ smaller than 15 000 K, we get $\langle \Delta T_{\rm eff,A-B}/T_{\rm eff,A} \rangle = 0.11 \pm 0.23$ and $\langle \Delta \log g_{\rm A-B}/\log g_{\rm A} \rangle = 0.09 \pm 0.04$; and

Downloaded from https://academic.oup.com/mnras/article/535/1/254/7774399 by guest on 09 December 2024

for the hotter ones: $\langle \Delta T_{\rm eff,A-B}/T_{\rm eff,A} \rangle = 0.17 \pm 0.17$ and $\langle \Delta \log g_{\rm A-B}/\log g_{\rm A} \rangle = 0.04 \pm 0.03$, which illustrates the bigger discrepancy in $T_{\rm eff}$ for hotter objects and the significant difference in $\log g$ for the cooler ones.

The refitted archival SDSS spectroscopy (B) of crossmatched DESI EDR (A) DB white dwarfs shows a good agreement, both in $T_{\rm eff}$ and $\log g$, with $\langle \Delta T_{\rm eff,A-B}/T_{\rm eff,A} \rangle = 0.000 \pm 0.018$ and $\langle \Delta \log g_{\rm A-B}/\log g_{\rm A} \rangle = -0.003 \pm 0.014$. The comparison between our SDSS + Pan-STARRS photometric (A) parameters and the *Gaia*-obtained values published by GF21 (B) results in $\langle \Delta T_{\rm eff,A-B}/T_{\rm eff,A} \rangle = 0.05 \pm 0.09$ and $\langle \Delta \log g_{\rm A-B}/\log g_{\rm A} \rangle = 0.003 \pm 0.018$. Given the small number of D(AB) white dwarfs no population study was performed, but the derived spectroscopic and photometric parameters are available in the online catalogue.

APPENDIX C: TABLES OF DQ CLASSIFICATIONS

Table C1. Carbon-rich atmosphere white dwarfs. Statistical errors from our fitting routines are given in brackets, which in some cases are underestimates. Realistic errors are 100 K in $T_{\rm eff}$ and 0.1 dex in $\log g$.

Name	Class	$T_{\rm eff}$ (K)	$\log g$	Mass ($M_\odot$)	log (C/He)	References/Notes
Newly confirmed carbon-rich systems						
WDJ072922.34+451425.96	DQ	7182 (62)	7.943 (0.155)	0.541	−6.261 (0.004)	
WDJ074019.13+314234.94	DQ	7385 (30)	7.988 (0.078)	0.568	−6.087 (0.006)	
WDJ084131.55 + 332915.47	DQ	6736 (23)	7.978 (0.087)	0.561	−6.741 (0.002)	
WDJ085049.40+315656.41	DQ	8859 (70)	7.724 (0.222)	0.427	−4.682 (0.007)	
WDJ085601.74+321354.51	DQ	22611 (1379)	9.286 (0.102)	1.252	∼0.100 (0.100)	
WDJ091350.42+833906.33	DQ	8334 (119)	7.926 (0.094)	0.533	−5.700 (0.015)	
WDJ092053.05+692645.36	DQ + DA	6250 (100)	7.333 (0.100)	0.262	−6.500 (0.100)	
WDJ092702.32+660414.45	DQ	8427 (112)	7.482 (0.154)	0.324	−5.600 (0.127)	
WDJ093332.74+690523.34	DQ	9501 (135)	8.119 (0.133)	0.647	−4.410 (0.006)	
WDJ101453.59+411416.94	DZQ	8438 (41)	7.858 (0.058)	0.498	−5.200 (0.150)	log (Ca/He) = −11.20 (0.15)
WDJ104933.02+831754.88	DQ	9543 (117)	8.414 (0.072)	0.835	−4.075 (0.005)	
WDJ112513.32+094929.68	DQH	10861 (200)	8.383 (0.100)	0.818	−0.158 (0.100)	
WDJ113918.83+560127.03	DQ	6030 (131)	8.152 (0.256)	0.664	−7.327 (0.012)	
WDJ115550.78+004602.30	DQ	6263 (100)	7.250 (0.100)	0.236	−6.839 (0.100)	
WDJ120827.22 − 001019.67	DQ	8149 (44)	7.837 (0.112)	0.484	−5.300 (0.010)	
WDJ121501.67+010057.72	DQ	5400 (100)	8.115 (0.100)	0.639	−7.700 (0.100)	
WDJ123426.71+534526.83	DQ	7011 (47)	7.847 (0.078)	0.487	−6.418 (0.006)	
WDJ124716.94+571031.84	DQ	7991 (99)	8.082 (0.099)	0.613	−5.500 (0.024)	
WDJ125047.16+265145.69[a]	DQ	5248 (100)	8.275 (0.100)	0.740	−6.481 (0.100)	
WDJ125207.43+745756.93	DQ	4750 (100)	8.171 (0.100)	0.673	−7.400 (0.100)	
WDJ130431.69+252847.56	DQ	6767 (43)	8.099 (0.072)	0.627	−6.964 (0.007)	
WDJ130830.91+062921.60	DQA	14137 (400)	8.993 (0.200)	1.158	−1.168 (0.100)	
WDJ133614.62+312322.83	DQ	7183 (100)	7.780 (0.100)	0.452	−5.163 (0.100)	
WDJ135004.41+701129.23	DQ	8088 (65)	7.989 (0.120)	0.569	−5.186 (0.008)	
WDJ141205.22 − 013214.32	DQ	6827 (41)	7.885 (0.066)	0.507	−6.248 (0.007)	
WDJ141844.14+512729.49	DQ	7934 (50)	7.913 (0.115)	0.525	−5.473 (0.003)	
WDJ142018.91+324921.12	DQZ	8370 (36)	7.892 (0.051)	0.551	−5.400 (0.150)	log (Ca/He) = −11.50 (0.15)
WDJ143047.56+023259.07	DQ	7565 (59)	8.012 (0.052)	0.566	−6.140 (0.006)	
WDJ143534.79+154813.46	DQ	6632 (45)	7.870 (0.108)	0.499	−6.968 (0.006)	
WDJ145256.54+762027.63	DQ	6995 (44)	7.796 (0.038)	0.460	−6.500 (0.009)	
WDJ151203.98+695231.94	DQ	6300 (150)	7.904 (0.100)	0.517	−7.300 (0.100)	
WDJ153904.40+335231.80	DQ	7962 (86)	7.671 (0.160)	0.402	−5.500 (0.016)	
WDJ160053.14+424017.74	DQ	7585 (71)	7.825 (0.135)	0.477	−5.623 (0.005)	
WDJ160244.40+435558.42	DQ	9725 (121)	8.306 (0.055)	0.765	−4.152 (0.005)	
WDJ160347.86+430810.38	DQ	13050 (200)	8.786 (0.100)	1.070	−1.632 (0.100)	
WDJ160411.92+434359.04	DQ	8947 (37)	7.925 (0.034)	0.534	−4.900 (0.005)	
WDJ160424.17+423816.28	DQ	5648 (100)	7.802 (0.100)	0.459	−7.151 (0.100)	
WDJ160755.84+440726.68	DQ	5050 (100)	7.657 (0.100)	0.385	−6.027 (0.100)	
WDJ161348.88+195024.46	DQ	7568 (51)	7.811 (0.145)	0.469	−5.953 (0.005)	
WDJ161659.09+534228.01	DQ	8217 (63)	7.935 (0.066)	0.538	−5.446 (0.002)	
WDJ164417.61+234720.41	DQ	7889 (71)	7.639 (0.133)	0.387	−5.796 (0.007)	
WDJ171604.64+555548.08	DQ	8901 (74)	8.004 (0.076)	0.569	−4.766 (0.005)	
Known carbon-rich systems						
WDJ084151.18+324821.49	DQ	8362 (81)	7.860 (0.143)	0.496	−5.332 (0.007)	Koester & Knist (2006)
WDJ085914.71+325712.16	DQ	10300 (100)	8.589 (0.100)	0.951	−2.300 (0.100)	Liebert (1977)
WDJ110140.34+521807.26	DQ	8476 (52)	7.866 (0.075)	0.500	−5.024 (0.003)	Kepler et al. (2016); Coutu et al. (2019)
WDJ114048.36+554251.29	DQ	7713 (45)	7.946 (0.076)	0.544	−5.604 (0.009)	Vincent, Bergeron & Dufour (2023)
WDJ114851.69−012612.69	DQ	10327 (100)	8.573 (0.100)	0.941	−2.300 (0.100)	Berg et al. (1992)

Downloaded from https://academic.oup.com/mnras/article/535/1/254/7774399 by guest on 09 December 2024

Table C1 – *continued*

Name	Class	$T_{\rm eff}$ (K)	log g	Mass ($M_\odot$)	log (C/He)	References/Notes
WDJ115305.54+005646.15	DQ	19211 (400)	9.312 (0.100)	1.256	> 0.000	Liebert, Bergeron & Holberg (2003)
WDJ120936.52+535525.76	DQ	11666 (150)	8.426 (0.100)	0.846	−2.400 (0.100)	Eisenstein et al. (2006)
WDJ135810.43+055238.08	DQ	8282 (40)	7.956 (0.068)	0.550	−5.164 (0.005)	Kepler et al. (2015)
WDJ142032.64+531624.19	DQ	8487 (45)	7.920 (0.052)	0.530	−5.367 (0.005)	Koester & Kepler (2019)
WDJ154248.66+432902.53	DQ	10750 (100)	8.618 (0.100)	0.970	−2.500 (0.100)	Kleinman et al. (2013)
WDJ163837.83+360620.16	DQ	6963 (28)	8.004 (0.030)	0.565	−6.678 (0.006)	Kleinman et al. (2013)

[a]A poor fit was obtained.

APPENDIX D: TABLES OF METAL-LINE CLASSIFICATIONS

Table D1. White dwarfs exhibiting metal lines in the DESI sample.

Name	Class	Reference for DxZ candidacy
Newly confirmed metal-line systems		
WD J013105.68+314755.63	DAZ	
WD J014145.83+311049.96	DAZ	
WD J014211.57+314603.62	DBZ	
WD J020559.33−042230.18	DZB	
WD J054545.32−190245.54	DAZ	
WD J071959.42+402122.13	DBZ	Sion, Aannestad & Kenyon (1988)
WD J072234.27+425655.60	DZ	
WD J073321.79+321614.15	DAZ	
WD J074351.32+385615.78	DBZ	
WD J081556.53+345224.37	DAZ	
WD J081634.98+342638.54	DAZ	
WD J081918.86+334837.64	DAZ	
WD J082845.45+334600.34	DAZ	
WD J083213.85+010907.60	DBZ	
WD J083254.36+313904.84	DAZ	
WD J083834.87−064942.24	DBAZ	
WD J085748.04+332708.66	DBZ	
WD J085912.92−005842.86	DZA	
WD J090016.86+331819.03	DAZ	
WD J091725.71+325837.90	DBZ	
WD J092251.70+315028.36	DZ	
WD J092301.12+315828.32	DZAB	
WD J093106.58+684430.96	DBZA	
WD J093640.77+314335.15	DBZA	
WD J094111.57+705827.74	DZ	
WD J095936.19+034949.30	DAZ	
WD J101453.59+411416.94	DZQ	
WD J102012.80+315447.24	DAZ	Kepler et al. (2016)
WD J102447.72+332816.61	DAZ	
WD J103637.16+070948.00	DAZ	
WD J103812.22+825135.62	DAZ	
WD J104534.75−272726.47	DAZ	
WD J104709.52+712557.15	DZ	
WD J105627.17+485610.66	DAZ	
WD J105751.09+320839.62	DZ	
WD J105805.77+711242.56	DZ	
WD J105846.34+325113.01	DAZ	
WD J110145.42+313555.64	DAZ	
WD J110511.98+320003.98	DAZ	
WD J110835.57+522526.91	DZB	
WD J110858.03+513410.39	DBZ	
WD J111322.63+700635.27	DZ	
WD J112009.89+085641.99	DBZ	
WD J112638.23+720116.67	DZ	
WD J112807.93+530625.77	DZ	
WD J113233.24+723746.29	DAZ	
WD J113305.51+790621.07	DAZ	
WD J113320.85+505909.85	DAZ	

Downloaded from https://academic.oup.com/mnras/article/535/1/254/7774399 by guest on 09 December 2024

Table D1 – *continued*

Name	Class	Reference for DxZ candidacy
WD J113706.95+494337.11	DZB	
WD J113835.19+553922.24	DZ	
WD J114041.55+511835.62[a]	DAZ	Kepler et al. (2016)
Newly confirmed metal-line systems		
WD J114201.76+562949.00	DAZ	
WD J115040.63+552956.66	DZ	
WD J115802.16+010537.12	DZ	
WD J115803.66−011257.60	DZA	
WD J115908.60+525653.55	DZ	
WD J120538.84+524626.80	DAZ	
WD J120924.36+740639.27	DZ	
WD J121104.25+544857.06	DZ	
WD J121219.03−011535.95	DBZA	
WD J121354.40+531140.78	DABZ	
WD J121653.30+745525.29 [a]	DAZ	Rebassa-Mansergas et al. (2019)
WD J121710.48+321358.74	DAZ	
WD J122102.43+554835.08	DZ	
WD J122147.27+330426.63	DAZ	
WD J122239.60+305149.93	DAZ	
WD J122704.88+794236.33	DAZ	
WD J123026.82+800506.82	DZ	
WD J123352.65+544610.28	DAZ	
WD J123519.07+575949.54	DAZ	
WD J123544.36+623414.43	DBZ	
WD J123711.25+545128.03	DZ	
WD J123949.74+740823.33	DZ	
WD J124325.87+605227.97	DZ	
WD J124440.84+582304.08	DBZ	
WD J125250.17+735216.84	DZA	
WD J125427.39+735248.83	DAZ	
WD J125955.25+240542.09	DBZ	Vincent et al. (2023)
WD J130130.51+262150.50	DZ	
WD J130153.16+233106.57	DBZ	
WD J130931.30+162204.03	DAZ	
WD J133136.60+323835.96	DZ	
WD J141517.07+512345.35	DAZ	
WD J142018.91+324921.12	DQZ	
WD J142258.14−004853.17	DZ	
WD J143013.43+040018.09	DAZ	
WD J143304.74+330703.81	DZ	
WD J143555.99+135928.34	DZ	
WD J143651.40−004709.85	DAZ	
WD J143700.89+330917.72	DZ	
WD J143802.77+144137.61	DBZ	
WD J145242.22+753939.06	DBZ	
WD J150003.73+331948.23	DZ	
WD J150241.98+732528.73	DBZ	
WD J150831.23+330239.24	DAZ	
WD J151259.89+745158.02	DAZ	
WD J151521.50+155213.09	DAZ	
WD J153954.92+335444.49	DBZ	
WD J154155.46+745259.62	DZ	
WD J154252.76+445829.02	DZ	
WD J154310.62+314355.41	DZ	
WD J155050.49+744001.33	DBZA	
Newly confirmed metal-line systems		
WD J155300.64+692620.03	DZA	
WD J161316.63+552125.97	DAZ	
WD J161502.83+544603.38	DBZ	
WD J162344.53+744313.12	DAZ	
WD J163054.20+434009.43	DBZA	

Downloaded from https://academic.oup.com/mnras/article/535/1/254/7774399 by guest on 09 December 2024

Table D1 – *continued*

Name	Class	Reference for DxZ candidacy
WD J163405.62+314336.23	DAZ	
WD J164344.36+343305.46	DBAZ	
WD J165236.79+353437.58	DAZ	
WD J171723.85+574608.00	DAZ	
WD J172623.05+793759.60	DZ	
WD J175121.52+802758.90	DZ	
WD J175314.93+653107.61	DZ	
WD J175358.38+605738.86	DAZ	
WD J175445.49+610836.20	DBZA	
WD J175805.73+645520.41	DAZ	
WD J180322.69+664744.38	DAZ	
WD J180555.51+621534.72	DBZA	
WD J180804.35+645950.43	DAZ	
WD J181236.47+802423.37	DAZ	
Known metal-line systems		
WD J014125.42+225734.98	DZA	Kilic et al. (2020)
WD J080234.18+405015.21	DBAZ	Kepler et al. (2015)
WD J082611.70+325000.40	DAZ	Kilic et al. (2020)
WD J082720.59+330438.09	DZ	Eisenstein et al. (2006)
WD J083935.89+215844.56	DZ	Kleinman et al. (2013)
WD J085035.17+320804.29	DZAB	Kong, Luo & Li (2019)
WD J094024.06+642202.02	DZ	Kleinman et al. (2013)
WD J095406.45+334716.86	DZ	Kleinman et al. (2013)
WD J100237.36+031325.60	DZ	Eisenstein et al. (2006)
WD J110513.63+500652.49	DZAP	Hollands et al. (2017)
WD J112035.20+525754.44	DZB	Gentile Fusillo, Gänsicke & Greiss (2015); Guo et al. (2015)
WD J112617.18+524155.12	DZ	Eisenstein et al. (2006)
WD J114054.89+532827.33	DZA	Dufour et al. (2007a)
WD J114830.09+570840.98	DZ	Kepler et al. (2016)
WD J115926.98+290105.85	DZ	Vincent et al. (2023)
WD J121129.27+572417.24	DAZ	Zuckerman & Reid (1998)
WD J121218.70+540938.68	DZ	Eisenstein et al. (2006)
WD J121837.12+002303.87	DZ	Kleinman et al. (2004); Eisenstein et al. (2006)
WD J125922.03+311215.59	DZ	Hollands et al. (2017)
WD J125946.66+273404.14	DAZ	Zuckerman et al. (2003)
WD J133305.34+325400.11	DBZ	Kleinman et al. (2013); Coutu et al. (2019)
WD J135632.60+241606.27	DZ	Koester et al. (2011)
WD J141426.55−011354.63	DZ	Harris et al. (2003)
WD J141518.65+315551.05	DZAB	Gentile Fusillo et al. (2019)
WD J142516.43−005048.83	DZ	Harris et al. (2003)
WD J142736.17+534828.00	DBAZ	Kenyon et al. (1988)
WD J143235.82+035423.22	DZAB	Eisenstein et al. (2006)
WD J154907.13+442258.06	DZ	Kepler et al. (2015)
WD J155847.91+150735.08	DZ	Kleinman et al. (2013)
WD J160731.21+444248.06	DBZ	Kepler et al. (2015)
WD J162646.91+313628.00	DZBA	Kepler et al. (2015)

[a]Identified as a candidate for hosting a dusty disc.

APPENDIX E: TABLES OF MAGNETIC CLASSIFICATIONS

Downloaded from https://academic.oup.com/mnras/article/535/1/254/7774399 by guest on 09 December 2024

Table E1. Magnetic field strengths, B, determined for magnetic white dwarfs in our sample. Statistical errors from our fitting routines are given in brackets which do not take into account systematics or more complex field structures, and a more reasonable lower bound is $\simeq 5$ per cent of the derived B.

Name	Class	B (MG)	References
Newly identified magnetic systems			
WD J022723.13−055305.72	DAH	20.5 (0.4)	
WD J042613.14−034701.99[a]	DAH	250–1000	
WD J070253.76+553733.64[b]	DAH	6.89 (0.07)/15.5 (0.2)	
WD J082302.41+334534.27	DAH	1.344 (0.008)	
WD J084546.99+194542.45	DAH	7.01 (0.05)	
WD J085045.22+110553.50	DAH	542 (1)	
WD J085753.69+331453.52	DAH	22.9 (0.2)	
WD J092625.68+710020.09	DAH	39.3 (0.8)	
WD J100055.37+690330.42	DAH	290 (9)	
WD J102146.26+310551.99	DAH	12.2 (0.2)	
WD J110146.25+323101.96	DAH	1.89 (0.06)	
WD J110344.93+510048.61	DAH	1.822 (0.008)	
WD J110759.25+812213.63	DAH	18.3 (0.2)	
WD J111940.70+722847.58	DAH	10.90 (0.02)	
WD J112513.32+094929.68	DQH	2.19 (0.01)	
WD J121945.85+543402.99	DAH	3.57 (0.07)	
WD J125820.50+281357.33	DAH	2.57 (0.02)	
WD J125954.37+252756.09	DAH	2.09 (0.02)	
WD J130522.83+244537.01	DAH	13.5 (0.3)	
WD J131051.11+171049.60	DAH	0.81 (0.01)	
WD J133158.03+312721.23	DAH	3.05 (0.06)	
WD J135820.93+045021.46	DAH	2.30 (0.01)	
WD J140009.88+042015.44	DAH	2.90 (0.03)	
WD J140100.50+043720.71	DAH	2.4 (0.1)	
WD J140916.34−000011.32[c]	DAHe	23.5	Manser et al. (2023)
WD J142645.38+020101.87	DAH	1.83 (0.02)	
WD J143122.24+353420.07	DAH	12.60 (0.02)	
WD J143550.43+140519.59	DAH	4.30 (0.03)	
WD J143755.33+141345.64	DAH	660 (50)	
WD J143804.42−005220.49	DAH	15.0 (0.1)	
WD J160604.06+550924.93	DAH	2.214 (0.007)	
WD J161053.06+535518.49	DAH	0.585 (0.004)	
WD J161634.36+541011.51[c]	DAHe	6.5 (0.1)	Manser et al. (2023)
WD J162713.92+313559.18	DAH	1.394 (0.007)	
WD J165631.22+760850.65	DAH	73.8 (0.5)	
WD J175419.17+660224.85	DAH	12.9 (0.2)	
WD J180147.11 + 652136.43	DAH	2.71 (0.02)	
WD J180813.60+652321.24	DAH	24.1 (0.4)	
WD J181222.70+624810.54	DAH	14.0 (0.2)	
Previously known magnetic systems			
WD J023420.63+264801.74	DAH	27.2 (0.3)	Külebi et al. (2009)
WD J073615.92+403335.18	DAH	2.12 (0.02)	Kepler et al. (2015); Vincent et al. (2023)
WD J111812.68+095241.52	DAH	2.71 (0.03)	Vanlandingham et al. (2005)
WD J112328.50+095619.35	DAH	0.966 (0.007)	Külebi et al. (2009)
WD J112926.23+493931.89	DAH	3.00 (0.02)	Vanlandingham et al. (2005)
WD J113357.66+515204.69[b]	DAH	3.04 (0.07)/4.4 (0.1)	Schmidt et al. (2003)
WD J115418.15+011711.55	DAH	18.4 (0.2)	Schmidt et al. (2003)
WD J121209.31+013627.77[d]	DAH	7.21 (0.02)	Schmidt et al. (2003, 2005)
WD J121548.73−005637.56	DAH	1.653 (0.005)	Kilic et al. (2020)
WD J131426.39+173228.40	DAH	0.982 (0.008)	Kepler et al. (2013)
WD J141813.22+312340.03	DAH	1.23 (0.02)	Kepler et al. (2013)
WD J160357.94+140929.77	DAH	25.4 (0.3)	Kepler et al. (2013)
WD J164703.24+370910.23	DAH	2.7 (0.9)	Vanlandingham et al. (2005)
WD J165029.91+341125.53	DAH	2.29 (0.02)	Vanlandingham et al. (2005)
WD J165203.68+352815.81	DAH	6.29 (0.05)	Schmidt et al. (2003)
WD J165249.09+333444.98	DAH	3.00 (0.02)	Külebi et al. (2009)
WD J174807.99+705235.92	DAH	203 (3)	Angel et al. (1974a)

[a]We give a range of field strengths as only a single stationary component at $\simeq 8600$ Å is observed.
[b]Evidence of an offset-dipole field structure with five Zeeman components visible and we give field strengths for both poles separated by '/'.
[c]Field strength reproduced from Manser et al. (2023).
[d]This white dwarf is part of the binary system, V∗ V379 Vir, with the secondary likely being a brown dwarf.

Downloaded from https://academic.oup.com/mnras/article/535/1/254/7774399 by guest on 09 December 2024

APPENDIX F: TABLES OF CVS CLASSIFICATIONS

Table F1. Table of 12 CVs identified in the DESI EDR which includes three new systems, two confirmed candidates, and seven previously known systems. All systems except J161927.83+423039.61 are present in the Gentile Fusillo et al. (2021) *Gaia* EDR3 white dwarf catalogue.

Name	Alternative name	Simbad type	References
Newly confirmed CVs			
J124413.48+593610.24	Gaia 16adi	CV candidate	Hodgkin et al. (2021)
J142833.44+003100.45		CV candidate	Croom et al. (2004)
J143435.39+334049.98		WD candidate	
J161927.83+423039.61		Star	
J181130.89+795608.36		WD candidate	
Known CVs			
J022319.73–052002.02	2XLSSd J022319.8−052002	CV	Kepler et al. (2016); Gentile Fusillo et al. (2019)
J090350.73+330036.11	CRTS J090350.7+330036	CV	Szkody et al. (2005)
J125510.56+264226.59	V∗ MT Com	CV	Watson et al. (1996)
J131223.48+173659.21	2XMMp J131223.4+173659	CV	Vogel et al. (2008)
J150241.00+333424.00	V∗ NZ Boo	CV	Szkody et al. (2006)
J151333.10+703721.98	Gaia 17bcx	CV	Hodgkin et al. (2021); Keller et al. (2022)
J162608.15+332827.83		CV	Szkody et al. (2004)

APPENDIX G: DESI EDR WHITE DWARF SYSTEMS NOT IN THE *GAIA* EDR3 WHITE DWARF CATALOGUE

Downloaded from https://academic.oup.com/mnras/article/535/1/254/7774399 by guest on 09 December 2024

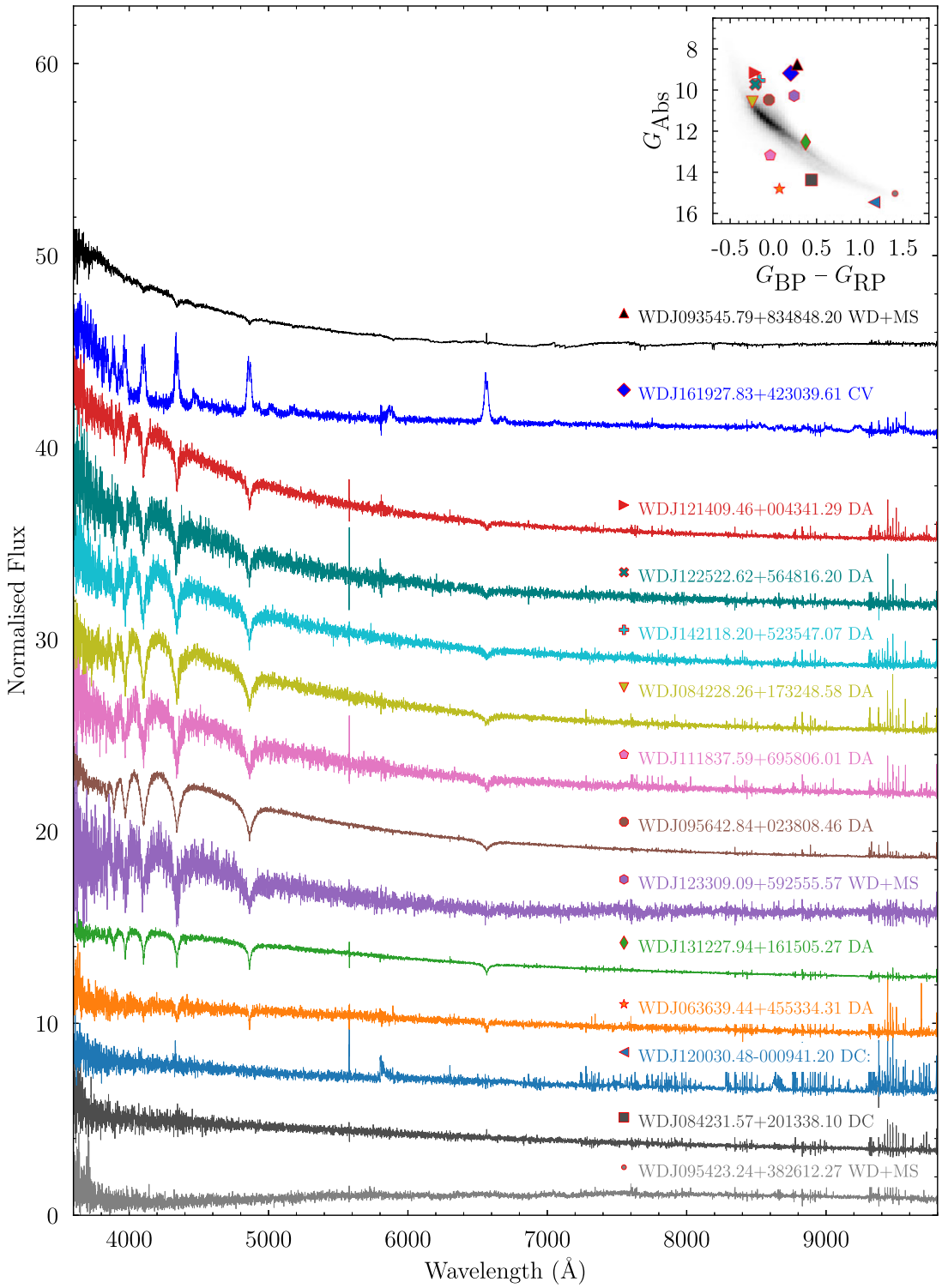

Figure G1. Normalized DESI spectra of white dwarf systems in the DESI EDR sample that do not have an entry in the *Gaia* EDR3 white dwarf catalogue of GF21. The spectra are offset by arbitrary amounts for clarity. A few systems have emission features that appear due to imperfect flux calibration and/or sky subtraction, which are particularly strong in the spectrum of WD J120030.48−000941.20. The inset shows the *Gaia* HRD, where each system is displayed with a corresponding coloured symbol outlined in red. For reference, the high-confidence ($P_{\rm WD} > 0.95$) *Gaia* white dwarfs brighter than $G = 20$ identified by GF21 are shown as a 2D grey-scale histogram.

Downloaded from https://academic.oup.com/mnras/article/535/1/254/7774399 by guest on 09 December 2024

[1]*Astrophysics Group, Department of Physics, Imperial College London, Prince Consort Road, London SW7 2AZ, UK*
[2]*Department of Physics, University of Warwick, Coventry CV4 7AL, UK*
[3]*Institut für Theoretische Physik und Astrophysik, University of Kiel, Kiel D-24098, Germany*
[4]*Department of Physics and Astronomy, University College London, London WC1E 6BT, UK*
[5]*Gemini Observatory/NSF's NOIRLab, 670 N. A'ohoku Place, Hilo, HI 96720, USA*
[6]*Department of Physics, Universita' degli Studi di Trieste, Via A. Valerio 2, Trieste I-34127 , Italy*
[7]*Institute for Astronomy, University of Edinburgh, Royal Observatory, Blackford Hill, Edinburgh EH9 3HJ, UK*
[8]*Institute of Astronomy, University of Cambridge, Madingley Road, Cambridge CB3 0HA, UK*
[9]*Kavli Institute for Cosmology, University of Cambridge, Madingley Road, Cambridge CB3 0HA, UK*
[10]*NSF's NOIRLab, 950 N. Cherry Avenue, Tucson, AZ 85719, USA*
[11]*Instituto de Astrofísica de Canarias, Vía Láctea, La Laguna E-38205, Spain*
[12]*Departamento de Astrofísica, Universidad de La Laguna, La Laguna E-38206, Spain*
[13]*Lawrence Berkeley National Laboratory, 1 Cyclotron Road, Berkeley, CA 94720, USA*
[14]*Physics Department, Boston University, 590 Commonwealth Avenue, Boston, MA 02215, USA*
[15]*Institute of Astronomy and Department of Physics, National Tsing Hua University, 101 Kuang-Fu Road, Section 2, Hsinchu 30013, Taiwan*
[16]*Department of Physics and Astronomy, The University of Utah, 115 South 1400 East, Salt Lake City, UT 84112, USA*
[17]*Instituto de Física, Universidad Nacional Autónoma de México, Cd. de México CP 04510, México*
[18]*Departamento de Física, Universidad de los Andes, Cra. 1 No. 18A-10, Edificio Ip, Bogotá CP 111711, Colombia*
[19]*Observatorio Astronómico, Universidad de los Andes, Cra. 1 No. 18A-10, Edificio H, Bogotá CP 111711, Colombia*
[20]*Institut d'Estudis Espacials de Catalunya (IEEC), Barcelona E-08034, Spain*
[21]*Institute of Cosmology and Gravitation, University of Portsmouth, Dennis Sciama Building, Portsmouth PO1 3FX, UK*
[22]*Institute of Space Sciences (ICE-CSIC), Campus UAB, Carrer de Can Magrans s/n, Bellaterra E-08913, Spain*
[23]*Center for Cosmology and AstroParticle Physics, The Ohio State University, 191 West Woodruff Avenue, Columbus, OH 43210, USA*
[24]*Department of Physics, The Ohio State University, 191 West Woodruff Avenue, Columbus, OH 43210, USA*
[25]*Laboratoire de Physique Nucléaire et de Hautes Energies (LPNHE), Sorbonne Université, CNRS/IN2P3, Paris FR-75005, France*
[26]*Department of Astronomy and Astrophysics, University of Toronto, Toronto, ON M5S 3H4, Canada*
[27]*Institució Catalana de Recerca i Estudis Avançats, Passeig de Lluís Companys, 23, E-08010 Barcelona, Spain*
[28]*Institut de Física d'Altes Energies (IFAE), The Barcelona Institute of Science and Technology, Campus UAB, Bellaterra E-08193, Spain*
[29]*Department of Physics and Astronomy, Siena College, 515 Loudon Road, Loudonville, NY 12211, USA*
[30]*National Astronomical Observatories, Chinese Academy of Sciences, A20 Datun Road, Chaoyang District, Beijing 100012, P. R. China*
[31]*IRFU, CEA, Université Paris-Saclay, Gif-sur-Yvette FR-91191, France*
[32]*Department of Physics and Astronomy, University of Waterloo, 200 University Avenue West, Waterloo, ON N2L 3G1, Canada*
[33]*Perimeter Institute for Theoretical Physics, 31 Caroline Steet North, Waterloo, ON N2L 2Y5, Canada*
[34]*Waterloo Centre for Astrophysics, University of Waterloo, 200 University Avenue West, Waterloo, ON N2L 3G1, Canada*
[35]*Space Sciences Laboratory, University of California, 7 Gauss Way, Berkeley, CA 94720, USA*
[36]*Department of Physics, University of California, 110 Sproul Hall #5800, Berkeley, CA 94720, USA*
[37]*Instituto de Astrofísica de Andalucía (CSIC), Glorieta de la Astronomía, s/n, GranadaE-18008, Spain*
[38]*Department of Physics, Kansas State University, 116 Cardwell Hall, Manhattan, KS 66506, USA*
[39]*Department of Physics and Astronomy, Sejong University, Seoul 143-747, South Korea*
[40]*CIEMAT, Avenida Complutense 40, MadridE-28040, Spain*
[41]*Space Telescope Science Institute, 3700 San Martin Drive, Baltimore, MD 21218, USA*
[42]*Department of Physics, University of Michigan, Ann Arbor, MI 48109, USA*
[43]*Department of Physics and Astronomy, Ohio University, Athens, OH 45701, USA*

This paper has been typeset from a TEX/LATEX file prepared by the author.

Downloaded from https://academic.oup.com/mnras/article/535/1/254/7774399 by guest on 09 December 2024

© 2024 The Author(s).
Published by Oxford University Press on behalf of Royal Astronomical Society. This is an Open Access article distributed under the terms of the Creative Commons Attribution License (https://creativecommons.org/licenses/by/4.0/), which permits unrestricted reuse, distribution, and reproduction in any medium, provided the original work is properly cited.